Physical, Chemical, & Nano Sciences Center

Research Briefs

2009

Sandia National Laboratories
Albuquerque, New Mexico

A Multiprogram Laboratory

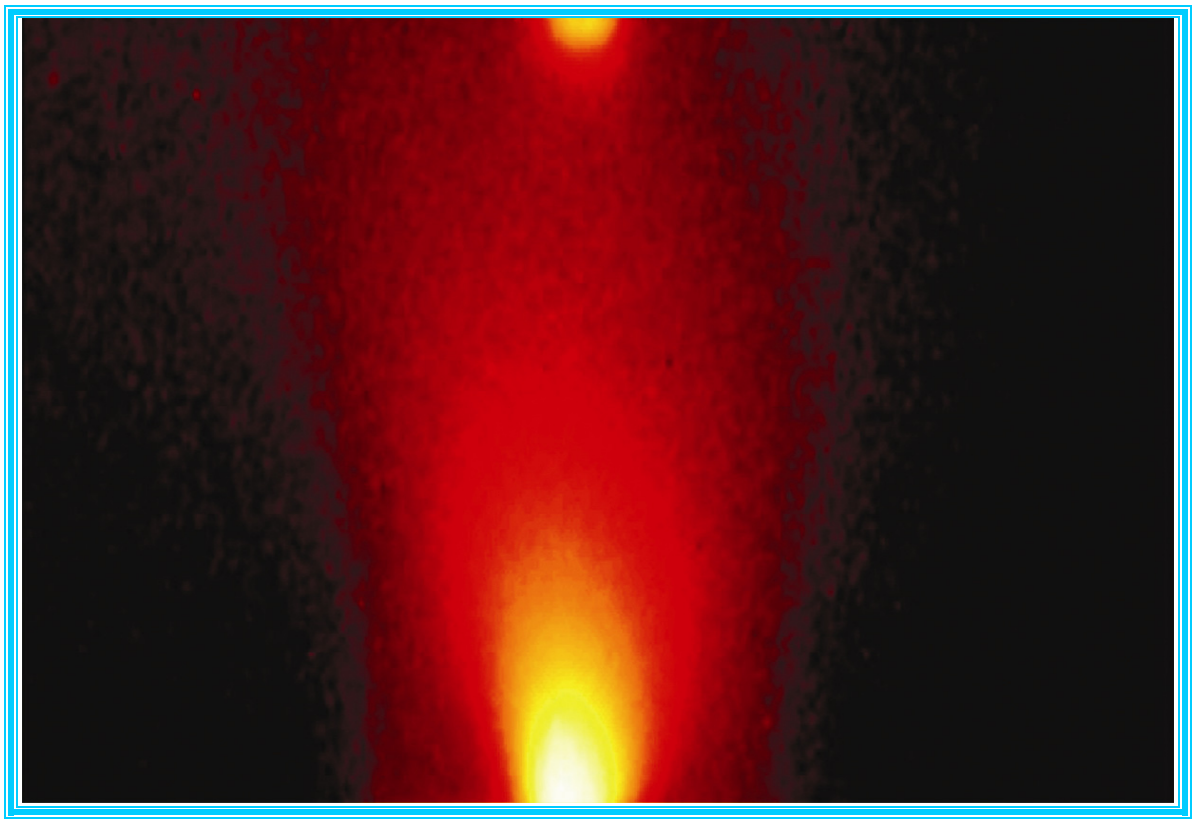

Research Briefs for the Physical, Chemical, & Nano Sciences Center is published by Sandia National Laboratories, a multiprogram laboratory operated by Sandia Corporation, a Lockheed Martin Company, for the United States National Nuclear Security Administration and the Department of Energy under Contract DE-AC04-94AL85000.

Additional complimentary copies are available by contacting:

Julia M. Phillips
Physical, Chemical, & Nano Sciences Center, 1100
Sandia National Laboratories
Albuquerque, NM 87185-1427

Phone: (505) 844-1071
Fax: (505) 844-6098
Email: jmphill@sanida.gov
url: http://www.sandia.gov/pcnsc

Research Briefs

Editors
Julia M. Phillips
David R. Sandison
Jerry A. Simmons

Production
Katelynn G. Florentino
Clare A. Stanopiewicz

Cover Page: The figure depicts a 50 ns snapshot of light emitted from a metal plasma generated by a co-linear, triggered vacuum arc. The image is presented in a log scale, spanning three orders of magnitude and corresponds to a the time just prior to the development of a fully ionized plasma channel bridging the 10 mm gap. Sophisticated diagnostic techniques like this or laser-collision induced fluorescence (E. V. Barnat on p. 52) are used to provide critical data needed to validate predictive simulations being developed at Sandia. See the brief by E.V. Barnat on p. 52.

Message from the Director

The **Physical, Chemical, and Nano Sciences Center** supports Sandia's energy and broad national security mission by combining the scientific excellence and mission understanding of its staff to provide new high impact knowledge and solutions in the areas of radiation effects, compound semiconductors, remote sensing, materials interfaces, and nanostructured materials. We are Sandia's leading performer of focused long-term scientific research in anticipation of future mission needs in these areas. This volume highlights representative research in our areas of emphasis, including nitride semiconductor science and technology for solid-state lighting; science and technology for quantum information processing; nuclear weapons science and technology; science and technology for national missions; and a sampling of some of our most fundamental scientific studies.

The activities of the Physical, Chemical, and Nano Sciences Center are supported by a diverse set of funding sources reflecting the broad impact of our work, both scientifically and programmatically. The research described in this volume illustrates the importance of a strong science base in the physical, chemical, and nano sciences for the success of the Department of Energy's missions and Sandia's broader mission in national security. In this work, we have benefited immeasurably from our partnerships with colleagues across the labs, in universities, and in industry. We gratefully acknowledge their collaboration.

We appreciate your interest in our work and welcome your comments and inquiries.

Julia M. Phillips
Director

Table of Contents

Solid-State Lighting: Nitride Semiconductor Science and Technology

Energy Frontier Research Center for Solid-State Lighting Science (J.A. Simmons, M.E. Coltrin and J.Y. Tsao) 6

Solid-State Lighting: An Integrated Human Factors, Technology and Economic Perspective (J.Y. Tsao, M.E. Coltrin, M.H. Crawford, and J.A. Simmons) 8

Energy Transfer from an Electron-Hole Plasma Layer to a Quantum Well (S.K. Lyo) 10

Growth Mechanisms that Control InGaN Step Morphology (D.D. Koleske, S.R. Lee, M.H. Crawford, M.E. Coltrin, J.M. Kempisty, and K.C. Cross) 12

Impact of Gas-Phase and Surface Chemistry During InGaN MOCVD (J.R. Creighton, M.E. Coltrin, D.D. Koleske, and J.J. Figiel) 14

Growth and Characterization of Mg-doped AlGaN/AlN Superlattices (A.A. Allerman, M.H. Crawford, M.A. Miller, and S.R. Lee) 16

Dislocation Density Reduction in GaN Using Self-Assembled Masking Layers of Silica Microspheres (G.T. Wang and Q. Li) 18

Science and Technology for Quantum Information Processing

Low Noise Exchange Gates in Double Quantum Dots (E. Nielsen and R. Muller) 22

Observation of a Percolation-Induced 2D Metal-Insulator Transition in a Si MOSFET (L.A. Tracy, E.H. Hwang, K. Eng, G.A. Ten Eyck, E.P. Nordberg, K. Childs, M.S. Carroll, M.P. Lilly, and S. Das Sarma) 24

Charge Sensing in Silicon Metal-Oxide-Semiconductor Quantum Dots (E.P. Nordberg, H.L. Stalford, R. Young, G.A. Ten Eyck, K. Eng, L.A. Tracy, K.D. Childs, J.R. Wendt, R.K. Grubbs, J. Stevens, M.P. Lilly, M.A. Eriksson, and M.S. Carroll .) 26

Observation of a Possible New Non-Abelian Quantum Hall State (W. Pan) 28

Advancements in Single Ion Geiger Mode Avalance Photodiodes (SIGMA) Detectors for the QIST Grand Challenge (E. Bielejec and M.S. Carroll) 30

Highlights in Condensed Matter Science

Superplastic Salt Nanowires (N.W. Moore, J.E. Houston, and J.Y. Huang) 34

The Role of Carbon Surface Diffusion on the Growth of Epitaxial Graphene on SiC (T. Ohta, N.C. Bartelt, S. Nie, K. Thuermer, and G.L. Kellogg) 36

Isothermal Magnetic Advection: Functional Flows for Heat and Mass Transfer (J.E. Martin and K. Solis) 38

Adatom and Addimer-Mediated Exchange Diffusion in the Ge/Si(001)Surface Alloy (E. Bussmann and B.S. Swartzentruber) 40

Determining the GaSb/GaAs-(2x8) Reconstruction and Its Impact on Stress Relaxation (J.E. Bickell, N.A. Modine, and J.M. Millunchick) 42

Table of Contents Cont'd

In-Situ Structure and Property Correlation of Nanostructured Materials by Using a TEM-SPM Platform (J. Huang) 44

In-Situ Structures for Nanoscale Electrochemistry (J.P. Sullivan, M.J. Shaw, A. Subramanian, and J. Huang) 46

Nuclear Weapons Science and Technology

Evolution of Mechanical Properties during Aging of ErT_2 Target Films (J.A. Knapp, J.F. Browning, and G.M. Bond) 50

Two-Dimensional Mapping of Electron Densities in an Ionized Plasma Using Laser-Collision Induced Fluorescence (E.V. Barnat) 52

Resolving Neutron Induced Defects in the Silicon Bipolar Transistor (R.M. Fleming) 54

Semiconductor Q-switch Demonstrated in Solid-State Microlaser (J.G. Cederberg, D.A. Bender, M.V. Pack, and R.L. Schmitt) 56

A New Capability for Using Orbital-Dependent Functionals in Density-Functional-Theory Calculations (A.F. Wright, N.A. Modine, D.M. Day, L. Romero, and M.P. Desjarlais) 58

Evolution of Oxide Stability During Localized Corrosion of Model Al-Cu Alloys (N.A. Missert, R.G. Copeland, P.G. Kotula, J.J. Hren, and J.M. Rivera) 60

Science and Technology for National Missions

Monolithically Integrated Solid-State Terahertz Transceivers (M.C. Wanke, E.W. Young, C.D. Nordquist, M.J. Cich, A.D. Grine, C.T. Fuller, J.L. Reno, and M. Lee) 64

Longwave Infrared Optical Cross Sections for Biological Warfare Agents and Simulants (R.L. Schmitt, S.M. Sickafoose, M.S. Johnson, M.V. Pack, J.W. Porter, C.F. Briner, and D. Castillo) 66

Nanoporous-Carbon Coated SAWs for ppb Detection of Trihalomethanes in Water (M.P. Siegal, C.D. Mowry, K.B. Pfeifer, and A.L. Robinson) 68

Trapping of Deuterium at Displacement Damage in Tungsten and the Implications for Tritium Retention in ITER (W.R. Wampler) 70

Recent Awards & Prizes 74

Government & National Advisory Boards & Professional Societies 80

Resource & Capabilities 88

Physical, Chemical, and Nano Sciences Center FY09 Budget 97

Solid-State Lighting: Nitride Semiconductor Science and Technology

Energy Frontier Research Center for Solid-State Lighting Science

by J. A. Simmons, M. E. Coltrin, and J. Y. Tsao

Motivation—Sandia National Laboratories will be home to one of 46 multi-million-dollar Energy Frontier Research Centers (EFRCs). The EFRCs, which will pursue advanced research on energy topics, are funded by the U.S. Department of Energy Office of Science. Our Solid-State Lighting (SSL) Science EFRC will receive $18 million in funding over the course of five years under this award.

Accomplishment—The overarching theme of our EFRC is the *exploration of energy conversion in tailored photonic structures*, a theme that is at the heart of SSL and other energy technologies and a theme of major scientific interest as discovery-class research. The EFRC will have three scientific Thrusts.

The first scientific Thrust is "Beyond 2D: Luminescent Nanowires, Nanodots and Hybrid Structures." In this Thrust, we are studying energy conversion routes in 1D and 0D nanostructures that go beyond the conventional 2D planar heterostructures typical of SSL technology. These nanostructures are scientifically interesting as vehicles for the science of the very small and for studying how energy quantization and conversion are influenced by dimensionality and proximity to surfaces and interfaces. Also, because of fundamental differences in how lower dimensional structures are synthesized and how they accommodate lattice mismatch and strain, these structures will allow study of defect-mediated energy conversion routes different from those occurring in traditional 2D heterostructures.

The second Thrust is "Beyond Perturbations: Light and Matter in Subwavelength Photonic Structures." We are investigating energy conversion routes in subwavelength photonic structures in which electromagnetic fields are stronger or more localized, and photonic densities of states more exquisitely controlled, than in structures typical of current SSL. Such extreme conditions are scientifically interesting as vehicles for the science of coherent, many-body phenomena. As new energy conversion routes are explored, entirely new SSL materials structures may arise from their understanding.

The third Thrust is "Wide-Bandgap Materials and Properties: Foundational Understanding and Beyond." We seek to understand radiative efficiency, which is due to the competition between radiative pathways and undesirable non-radiative pathways that produce heat instead of light. We will develop deeper insights into the synthesis of wide-bandgap materials, and the interplay between their defect and luminescent properties – both as applied to current SSL as well as to the first two Thrusts.

This EFRC includes collaborations with scientists at Rensselaer Polytechnic Institute, the Univ. of New Mexico, Caltech, LANL, Yale, Northwestern Univ., the Univ. of Massachusetts-Lowell, and Philips Lumileds Lighting.

Significance—Our fundamental scientific research has the goal of improving the energy-efficiency in the way we light our homes and offices. Currently, over 20% of the country's electrical energy is consumed by lighting. Solid-state lighting has the potential to cut that energy consumption in half or even more. Our science breakthroughs in photonic energy conversion may also impact solar photovoltaic technologies.

Sponsor for various phases of this work include: DOE Office of Basic Energy Sciences

Contact: Jerry A. Simmons, Semiconductor and Optical Sciences
Phone: (505) 844-8402, Fax: (505) 844-4045, E-mail: jsimmon@sandia.gov

Figure 1. Sandia National Laboratories participants in the new Solid-State Lighting Science Energy Frontier Research Center.

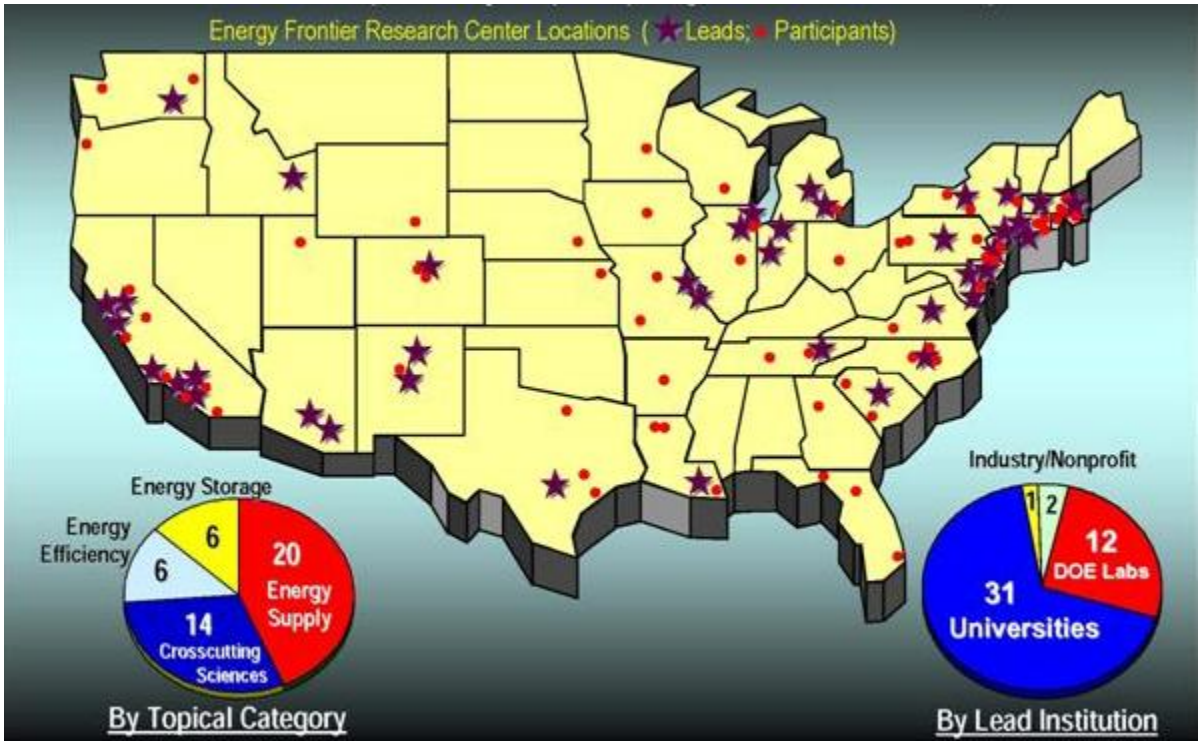

Figure 2. Distribution of EFRCs geographically across the United States, by topical research area, and lead institution.

Solid-State Lighting: An Integrated Human Factors, Technology and Economic Perspective

by J.Y. Tsao, M.E. Coltrin, M.H. Crawford, and J.A. Simmons

Motivation—Solid-state lighting (SSL) is a rapidly evolving technology now virtually certain to someday displace traditional lighting in applications ranging from the lowest-power spot illuminator to the highest-power broad-area illuminator. Moreover, SSL has considerable headroom for continued evolution even after this initial displacement. We have conducted a high-level analysis of solid-state lighting, with an emphasis on white lighting suitable for general illumination. We have examined in detail solid-state lighting's past and potential-future evolution using various performance and cost metrics, with special attention paid to inter-relationships between these metrics imposed by human factors, technology and economic considerations.

Accomplishment—

Human Factors: With respect to human factors, we considered the three key performance metrics associated with the desirability of white light for illumination purposes: luminous efficacy of radiation (K, with the units lm/W, or lumens per optical Watt); the "standard" color rendering index R_a; and correlated color temperature (CCT, with the units Kelvin, K). Importantly, these performance metrics are not independent of each other. For example, all other things being equal, as R_a or CCT increase, K decreases. Indeed, we have found, through simulations, that the relationship between K, R_a and CCT can be described by the equation:

$$\begin{aligned} K(R_a, CCT) &= 400\ \mathrm{lm/W} \\ &- 0.876\,(R_a - 85) \\ &- 0.0179\,(CCT - 3{,}800K) + 2.08\cdot 10^{-7}\,(CCT - 3{,}800K)^2 \end{aligned}$$

Technology: With respect to technology, we analyzed in detail the current SSL state-of-the-art and, using the above relationship, determined both its overall efficiency (14%) as well as the sub-efficiencies associated with its component pieces: blue LED (33%), phosphor+package (54%) and spectral (78%). An understanding of these sub-efficiencies enables us to assess how improvements in the various component pieces translate to improvement of the overall SSL lamp.

Economics: With respect to economics, we analyzed the overall ownership cost of light (including both operating and capital costs), and assessed past and potential-future trajectories for SSL. From advances already demonstrated in the research laboratory, we anticipate that 2012 will be the year in which the ownership cost of light of SSL will just dip below that of fluorescent and high-intensity discharge lighting, initiating a massive transformation to SSL. However, continuing this trajectory to so-called "ultra-high" (>70%) efficiencies will require advances of a significantly more challenging nature, including the development of narrow-linewidth orange-red phosphors or LEDs, and very high efficiency blue LEDs or laser diodes driven at very high currents.

Significance—Through an integrated analysis combining human factors, technology and economics, we have mapped past and possible-future trajectories for SSL. These trajectories enable a quantitative understanding (a) of how improvements in various SSL component pieces translate to improvement of SSL as a whole, and (b) of the relative importance of these various improvements.

Sponsors for various phases of this work include: DOE Office of Basic Energy Sciences

Contact: Jeff Y. Tsao, Physical, Chemical and Nano Sciences Center
Phone: (505) 844-7092, Fax: (505) 844-4045, E-mail: jytsao@sandia.gov

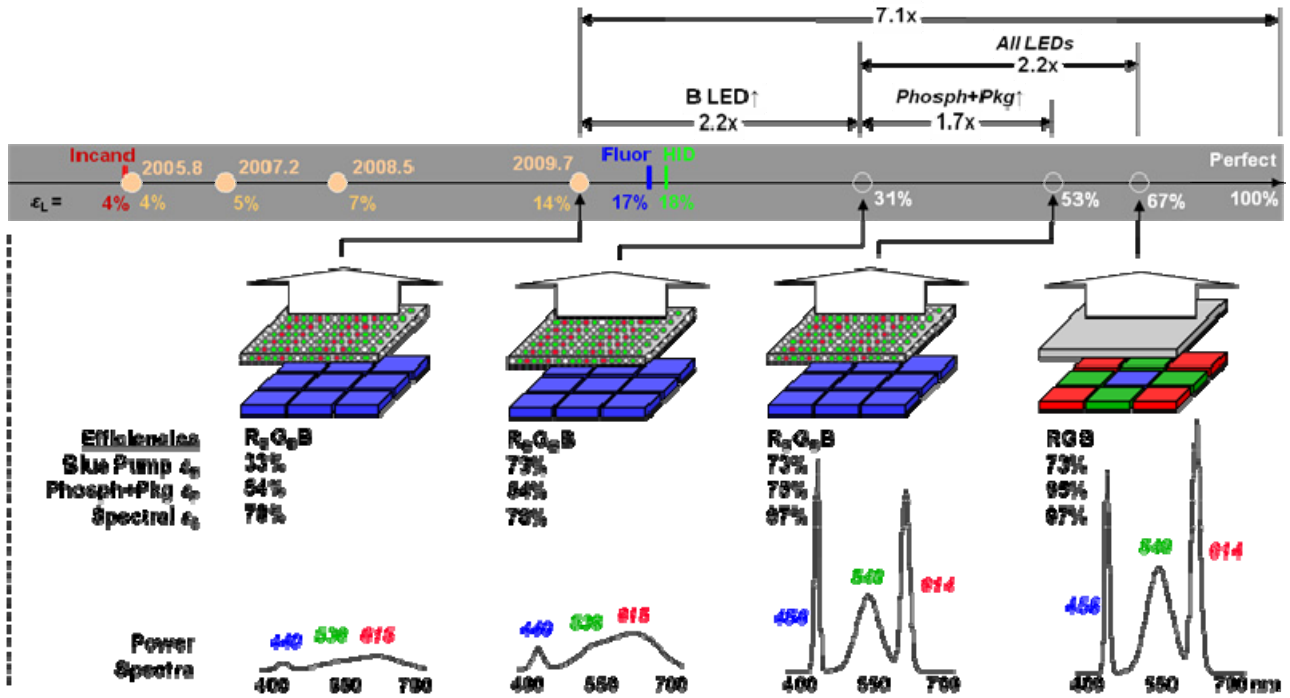

Figure 1.
Top: A lamp-efficiency ($\varepsilon_L = \varepsilon_B \cdot \varepsilon_P \cdot \varepsilon_S$) progress line illustrating the various classes of potential improvements in SSL. The progress scale is logarithmic, so equal horizontal distances correspond to equal percentage changes. At the far right of the plot is the 100%-efficient performance frontier. At the far left of the plot are the efficiencies of state-of-the-art solid-state white lamps achieved in the past four years (2006-2009). We have deliberately chosen data points for solid-state white lamps that correspond to commercial products, have a high R_a and, most importantly, are driven fairly hard (operated at high power) so as to have lower capital and ownership costs of light.
Middle: Potential-future lamps corresponding to three classes of improvements. The first two of these classes are associated with the current R_BG_BB approach to SSL: improvements to the blue LED pump source, and improvements to the phosphor and lamp package. The last of these classes is associated with non-phosphor approaches to SSL: the possible development of high-efficiency RGB sources, i.e., an "all-LED solution.
Bottom: Power spectra with center wavelengths labeled.

Energy Transfer from an Electron-Hole Plasma Layer to a Quantum Well

by ***S.K. Lyo***

Motivation—Energy transfer (ET) of charge-neutral optical excitations such as excitons and plasmas in confined structures is not only a fundamental physics problem that lacks full understanding but also has important applications to modern opto-electronic devices such as solid state lighting (SSL) structures. In SSL devices, optical energies or excitations are created through the diffusion of an electron/hole current into conduction/valence band. These excitations emit light after going through a series of ET. The optical excitations are in the form of excitons at a low density or a plasma at a high density of electrons and holes. The goal of our research is to investigate most efficient ET mechanisms between confined structures.

Accomplishment—As an initial study of various types of ET, we have studied the rates of ET from a two-dimensional (2D) quantum well (QW) populated by excitons/electron-hole (e-h) plasma in the low/high carrier-density regime to an empty QW as a function of the carrier density, the temperature, and the distance between the two QWs. The two QWs shown in Fig. 1(a) are assumed to be unequal with a finite energy-mismatch between the initial and final ground state sublevels and are coupled through dipole-dipole (i.e., Foerster) interaction. In ET processes, an e-h pair is destroyed in the initial QW, creating a free e-h pair in the final QW. The momentum of the center-of-mass is conserved. For anti-Stokes processes, energy is supplied through activation in the initial QW for energy conservation, while the excess energy is dissipated into the kinetic energies of the e-h relative motion for Stokes processes.

We found that the exciton ET rate (which is independent of the carrier density) is much faster than the plasma ET rate per e-h pair as shown in Fig. 1 (b). The latter increases sublinearly with the increasing density and saturates in the high-density limit. It dominates the former for the total ET power because of the large number of the carriers. Note that the temperature dependence of the exciton ET rate is strikingly different from the ET rates of plasmas as shown in Fig. 1 (b), indicating that the bound and unbound nature of the excitations can be distinguished from the temperature dependence of the rate. For excitons, the rate has a peak as a function of the decreasing temperature and vanishes at 0 K, while it increases steadily, saturating at 0 K for plasmas. This distinct behavior arises from 1) the linear dependence of the rate on the kinetic energy of the center-of-mass at low energy and 2) the Boltzmann/Fermi-Dirac statistics of excitons/plasmas. We have also calculated the ET power density as a function of the carrier density, the temperature, and the distance. The power is significantly large and decreases slowly as a function of the temperature as shown in Fig. 2. The rates and power decreases roughly as $1/d^4$ as a function of the distance d.

Significance—The power density of 2D-2D ET was shown to be significantly large even at room temperature, showing that plasmas are a useful power source for SSL applications. Our next step for the investigation is ET from a 2D plasma to quantum dots which have large oscillator strengths and are expected to be important for future efficient SSL devices.

Sponsors for various phases of this work include: DOE Office of Basic Energy Sciences

Contact: Ken Lyo, Semiconductor Material and Device Sciences
Phone: (505) 844-63178, Fax: (505) 844-4045, E-mail: sklyo@sandia.gov

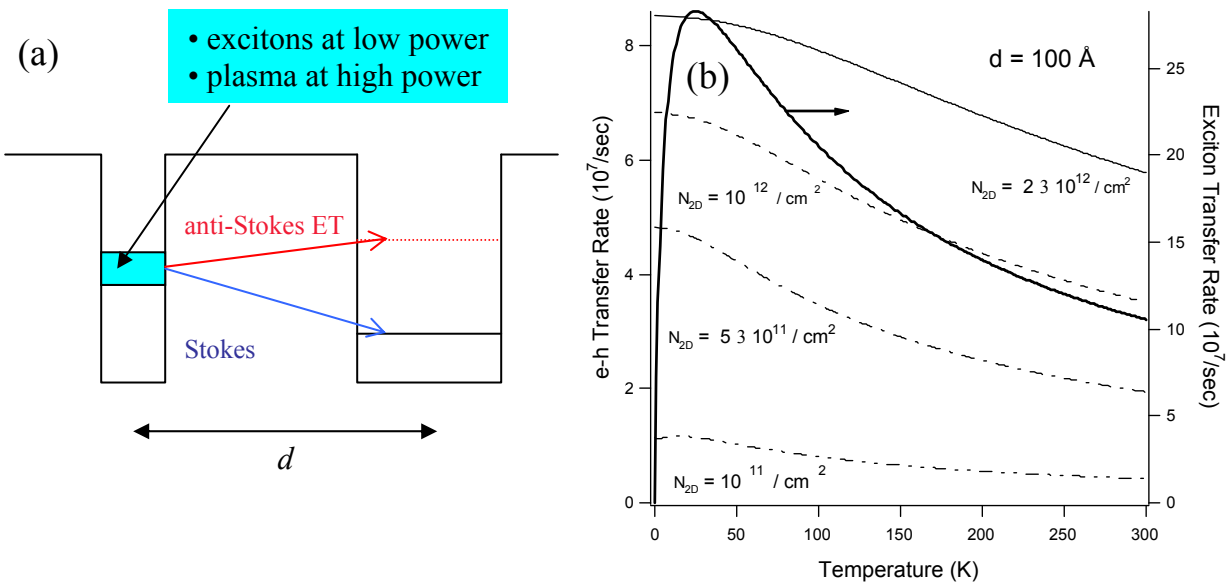

Figure 1. (a) Energy transfer from a quasi-2D exciton/plasma layer to an empty QW. (b) Energy transfer rates per e-h pair for plasmas for several pair densities (left axis: thin curves) at a distance *d* = 100 Å. The exciton transfer rate (right axis: thick solid curve) is independent of the density.

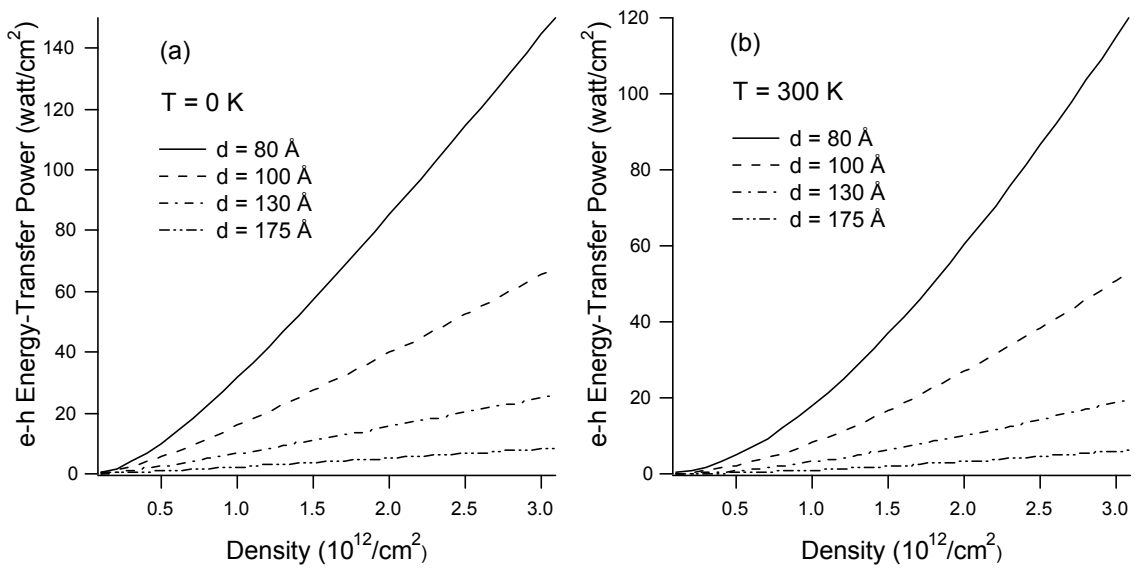

Figure 2. Energy transfer power per area as a function of the e-h pair density from a plasma layer to an empty QW at (a) 0 K and (b) 300 K for several distances *d*.

Growth Mechanisms that Control InGaN Step Morphology

by ***D. D. Koleske, S. R. Lee, M. H. Crawford, M. E. Coltrin, J. M. Kempisty, and K. C. Cross***

Motivation—Despite the high density of dislocations in GaN epitaxial layers grown on sapphire, InGaN-based light-emitting diodes (LEDs) grown on these GaN layers are surprisingly bright and efficient. Several theories have been proposed to explain this light emission efficiency. While important details of these theories vary, a unifying theme is the existence of carrier localization or potential barriers that prevent non-radiative recombination at dislocations or other defects. In this work, we explore nitride surface morphology and step height fluctuations and their role in carrier localization.

Accomplishment—For this study, green wavelength, 5-period InGaN/GaN multiple quantum wells (MQWs) were grown using two different temperatures of 800 and 900 ºC for the GaN barrier layers. The difference in the step morphology is shown in Fig. 1, where the steps heights are given as integer multiples of the c/2 step height of a single III-N monolayer. As evident in Fig. 1, the frequency of double-layer steps is larger for the GaN barriers grown at 800 ºC compared to 900 ºC barriers.

Motivated by this observation, we analyzed the power spectral densities, $g(q)$, of the AFM images shown in Fig. 1. The values of $g(q)$ vs. the reciprocal length scale, q, are calculated from the AFM height-height correlation function. Surface smoothing mechanisms can be discerned from $g(q)$'s power dependence, n, on q [1]. An example plot of this type is shown in Fig. 2, where $g(q)$ is plotted vs. q for the MQW samples shown in Fig. 1. For the MQW sample with 800 ºC barriers, the $g(q)$ vs. q plot gives an exponent, n, of 4.24, while for the MQW sample with 900 ºC barriers, the $\boldsymbol{g(q)}$ vs. $\boldsymbol{q}$ plot gives n = 1.97. Herring showed that n values near 2 are consistent with a smoothing mechanism involving *evaporation and recondensation* of atoms on the surface, while values near 4 are consistent with a smoothing mechanism involving *surface diffusion* [1]. Also shown in Fig. 2 for comparison is the $g(q)$ vs. q fit for the underlying high-temperature-grown GaN templates used for this study, where again $n \sim 2.0$. For other InGaN samples grown under a variety of conditions and composition ranges we typically measure $n \sim 4$.

Thus, our collective work suggests that during MQW growth, barrier growth at or above 900 ºC is smoothed via *evaporation and recondensation* mechanism ($n \sim 2$), which has longer gas-phase diffusion-length scales on the order of 1 to 10 microns. On the other hand, below 900 ºC, smoothing occurs by a surface diffusion ($n \sim 4$) mechanism, which operates over shorter length scales of order 10 to 100 nm. Corroboration for the length scale for the $n = 4$ mechanism is observed in Fig. 2 where the turnover in $g(q)$ for 800 ºC GaN barriers occurs near $q = 10\ \mu m^{-1}$, which corresponds to a length of 100 nm.

Finally, photoluminescence (PL) measurements find brighter luminescence from MQWs with barriers grown at 800 ºC compared to MQWs with barriers grown at 900 ºC, as seen in Fig. 3. X-ray diffraction studies of these two samples find similar indium concentrations (~20%) and QW thicknesses for both MQWs, suggesting that the difference in emission intensity may be due to enhanced localization in QWs grown on the more textured 800 ºC barrier layers.

Significance—Our work provides evidence that changes in growth mechanisms can be used to control InGaN/GaN MQW morphology; more-over, the morphology may be linked to emission efficiency. However, the causal link between the MQW growth morphology and PL emission intensity awaits further study.

[1]. Herring, J. Appl. Phys. 21, 301 (1950).

Sponsors for various phases of this work include: DOE Office of Basic Energy Sciences

Contact: Daniel D. Koleske, Advanced Materials Sciences
Phone: (505) 284-4531, Fax: (505) 844-3211, E-mail: ddkoles@sandia.gov

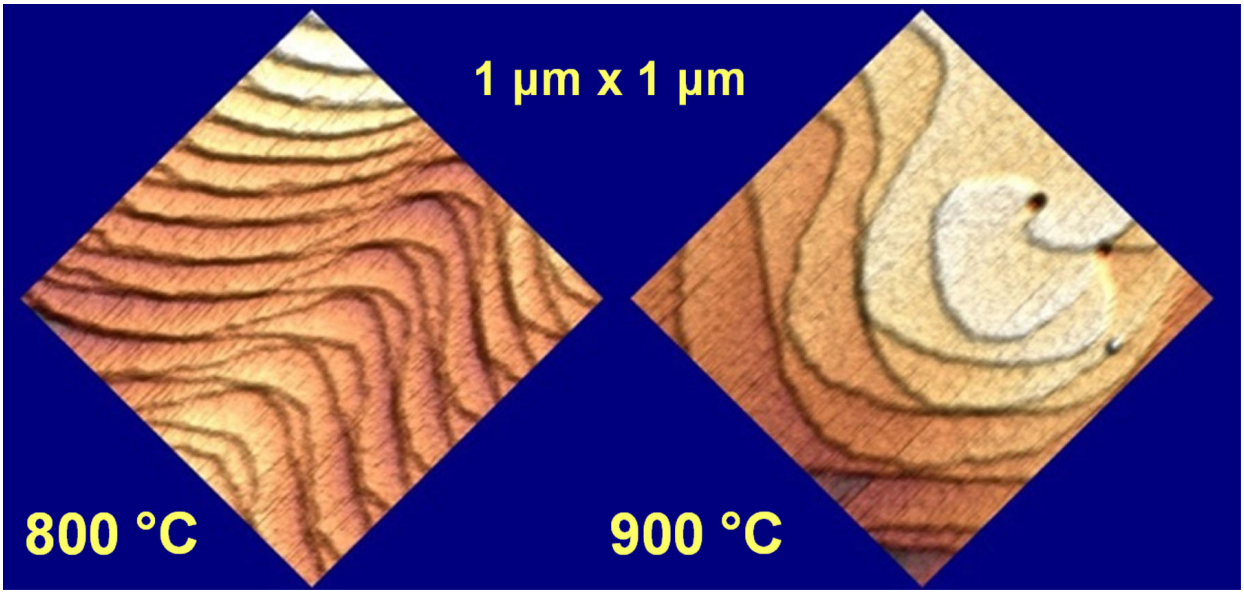

Figure 1. AFM images of green InGaN/GaN multiple quantum wells, with the GaN barriers grown at either 800 or 900 ºC.

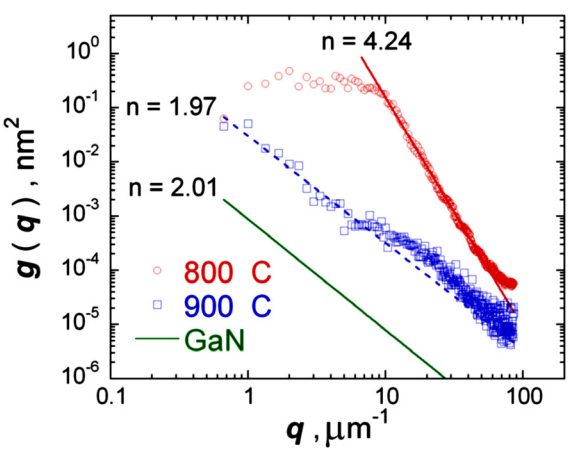

Figure 2. Calculated power spectral density, $g(q)$, plotted as a function of the reciprocal length, q, for green wavelength MQWs with the GaN barrier grown at either 800 °C (red) or 900 °C (blue). The separately measured $g(q)$ for high-temperature grown GaN is also shown in green.

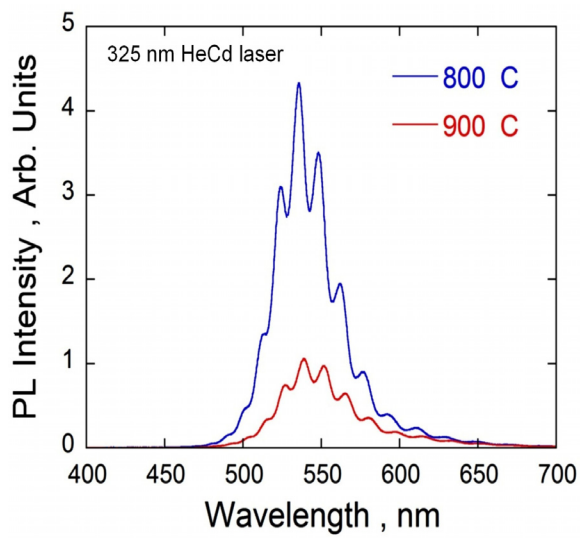

Figure 3. PL intensity for the two MQWs shown in Figure 1 with GaN barrier temperatures of 800 and 900 ºC.

Impact of Gas-Phase and Surface Chemistry During InGaN MOCVD

by J. Randall Creighton, Michael E. Coltrin, Daniel D. Koleske, and Jeffrey J. Figiel

Motivation—With bandgaps spanning the visible spectrum, InGaN alloys now form the basis of current solid-state-lighting technology. Metalorganic chemical vapor deposition (MOCVD) is the technique used to grow epitaxial InGaN thin films for such devices. However, indium incorporation into the growing InGaN films is very inefficient, temperature sensitive, and difficult to control. While these problems are often thought to be due to the limited thermodynamic stability of InGaN, other issues such as gas-phase parasitic chemical reactions during growth may also play an important role.

Accomplishment—As an extension to our earlier *in situ* light-scattering results we have employed a thermophoretic particle capture probe, whereby nanoparticles are collected on a TEM grid just "downstream" of the heated surface. During InGaN conditions we observe a significant population of particles with diameters in the 15-40 nm range, for example see Figure 1. This general observation of size range agrees well with our previous optical measurements. The particles appear to have a nearly spherical core, but often contain one or more irregular appendages, reminiscent of earlier GaN results. Many of the larger particles have well-defined lattice planes, and detailed analysis of the d-spacings revealed the presence of metallic indium, as expected, but also hexagonal InN and cubic In_2O_3. We believe the In_2O_3 results from the oxidation of the metallic indium during the air transfer of the grids to the TEM chamber. We therefore conclude that the gas-phase nanoparticles are actually a composite of metallic indium and InN. The composite structure possibly explains one peculiar aspect of the light-scattering measurements, which had suggested the presence of non-spherical particles. In order to test the relative importance of parasitic gas-phase chemistry versus surface chemistry we have examined the residence time dependence of the InGaN MOCVD process. In an ideal rotating-disk reactor (RDR) the residence time in the boundary layer is inversely proportional to the platen spin rate ($\mathbf{\Omega}$), so increasing the spin rate will tend to quench unwanted gas-phase reactions that may be depleting the growth precursors. For AlN and GaN MOCVD conditions where gas-phase parasitic reactions are very significant, the growth rate is strongly proportional to $\mathbf{\Omega}^n$, with n = 1.5-2.5. Therefore, if the parasitic gas-phase reactions are depleting the availability of indium, we would expect the InGaN growth rate and composition to respond dramatically to changes in $\mathbf{\Omega}$. We have instead found a rather weak dependence during growth of an InGaN multi-quantum well (MQW) structure at 770°C (see Figure 2). The GaN barrier layer thickness scales as $\sim\mathbf{\Omega}^{0.42}$, which is reasonably close to the $\mathbf{\Omega}^{1/2}$ dependence expected for transport-limited growth. The InGaN QW thickness scales as $\sim\mathbf{\Omega}^{0.25}$, which is even weaker than GaN barrier thickness dependence. The indium composition (not shown) is nearly independent of spin rate. These surprising results suggest that nanoparticles may play no significant role in limiting indium incorporation during InGaN MOCVD.

Significance—Results indicate that for growth temperatures of ~800°C nearly 100% of the indium near the surface is converted into gas-phase nanoparticles and is no longer available for InGaN growth. However, MOCVD results as a function of platen spin rate suggest that the nanoparticles may only be a "downstream" consequence and therefore play only a minor role in limiting indium incorporation. We are in the process of developing a detailed MOCVD chemical reaction mechanism that will hopefully reconcile the seemingly contradictory aspects of these findings.

Sponsors for various phases of this work include: DOE Office of Energy Efficiency & Renewable Energy

Contact: J. Randall Creighton, Advanced Materials Sciences
Phone: (505) 844-3955, Fax: (505) 844-3211, E-mail: jrcreig@sandia.gov

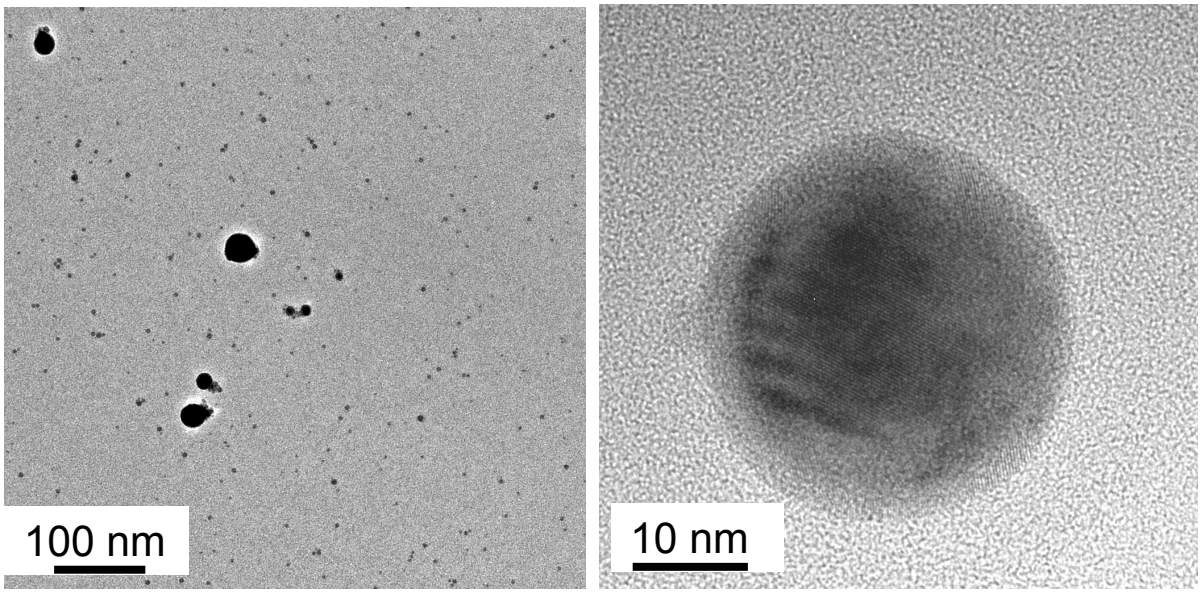

Figure 1. TEM of nanoparticles captured during InGaN conditions at 800°C

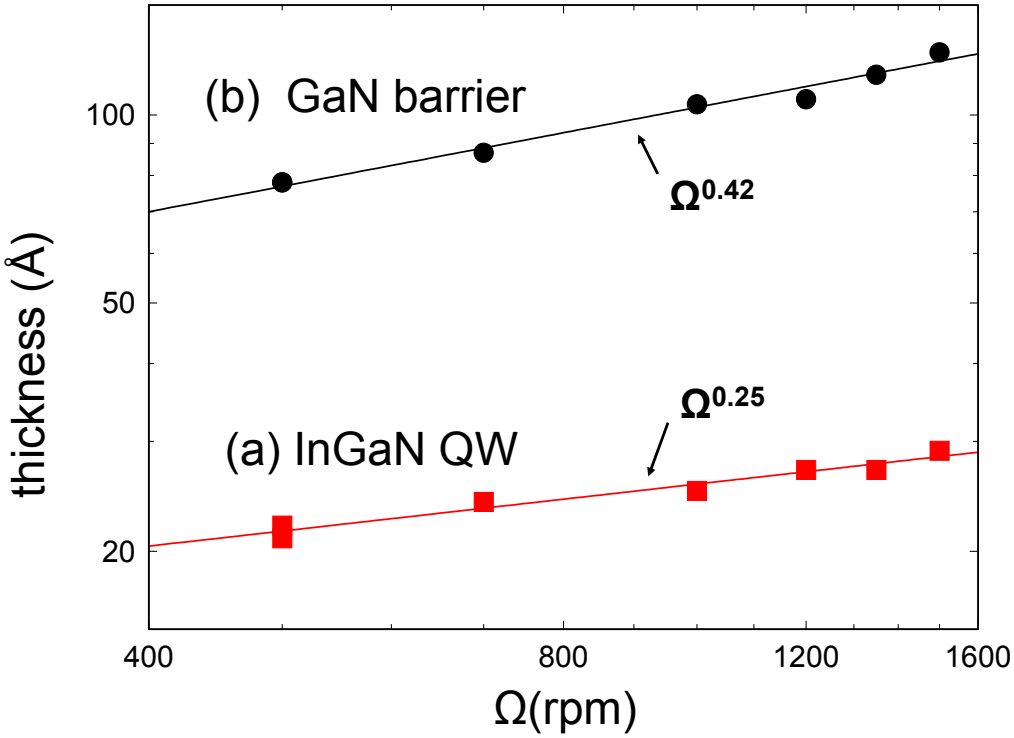

Figure 2. RDR spin rate dependence of InGaN QW thickness (curve-a) and GaN barrier layer thickness (curve-b) during MQW growth at 770°C.

Growth and Characterization of Mg-doped AlGaN/AlN Superlattices

by A. A. Allerman, M. H. Crawford, M. A. Miller and S. R. Lee

Motivation—AlGaN semiconductor alloys have tremendous potential for enabling deep ultraviolet (UV) LEDs and laser diodes for fluorescence-based bioagent sensing, water purification and other applications. To date, the realization of high performance devices has been frustrated by numerous AlGaN materials challenges. One of the most formidable challenges is obtaining effective p-type doping and hole transport in these wide bandgap alloys. In this work, we explore Mg-doped short-period superlattice structures as a method to overcome p-type doping limitations in deep UV light emitters.

Accomplishment—One promising approach to circumventing the high acceptor activation energies of III-nitride alloys is the application of superlattice (SL) structures doped with Mg. These periodic structures exploit the large polarization fields in wurzite III-nitrides to achieve enhanced hole activation and free hole concentrations. Much of the reported work on these structures has focused on GaN/AlGaN p-SLs with effective bandgaps suitable for near-UV and visible device applications. In this work, we developed Mg-doped short-period AlGaN/AlN superlattice structures (Mg-SPSLs) with significantly higher effective bandgaps suitable for deep UV devices. The Mg-SPSL structures employed nm-thick AlN and $Al_{0.23}Ga_{0.77}N$ epilayers grown by metal-organic vapor phase epitaxy. Mg-SPSL structures with periods ranging from 10-25 Å and with an average Al composition of 0.42 to 0.74 were investigated. Structures studied consisted of up to 1000 periods for a total thickness of 1 μm.

Optical, structural, and electrical characterization was performed to assess the applicability of these Mg-SPSLs to deep UV LED or laser structures. Optical transmission measurements demonstrated that these structures have an optical transparency similar to random-alloy $Al_xGa_{1-x}N$ epilayers of the same average composition (Figure 1). X-ray diffraction (XRD) measurements confirmed that the period and average Al composition of the Mg-SPSL were in agreement with targeted values. Additionally, we observed that Mg-doping of SPSL structures degraded or eliminated satellite peaks that were observed in XRD spectra from undoped or Si-doped SPSL structures, suggesting that the presence of Mg during growth alters the interfaces of the epilayers.

P-type lateral resistivities less than 10 ohm-cm were measured from Mg-SPSLs with an average Al composition from 0.42 to 0.74. Notably, a p-type resistivity of 6 ohm-cm was measured in a Mg-SPSL structure with an average Al composition of 0.74 and having an effective bandgap of ~5.3 eV. Analysis of temperature dependent resistivity showed an activation energy of 29 meV for a Mg-SPSL with an average composition of 0.62 and 18 meV for a Mg-SPSL with a composition of 0.49 (Figure 2). These values are significantly reduced from the > 200 meV values predicted for bulk AlGaN alloys. Overall, the combined characteristics of these Mg-SPSLs show promise for application to deep UV optoelectronic device structures.

Significance—Overcoming p-type doping challenges of AlGaN alloys represents a very significant step toward extending high performance LED and laser diode technology into the deep ultraviolet. These AlGaN materials may enable a new generation of compact, robust and highly integratable UV emitters for a wide array of applications including sensing, decontamination, spectroscopy and material processing.

Sponsors for various phases of this work include: Laboratory Directed Research & Development and Nuclear Weapons Technology Readiness Program

Contact: Andrew Allerman, Advanced Materials Sciences
Phone: (505) 845-3697, Fax: (505) 844-3211, E-mail: aaaller@sandia.gov

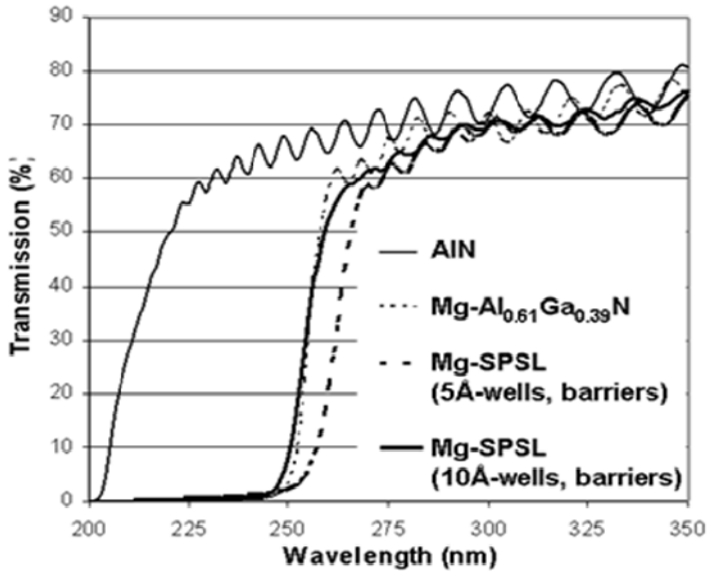

Figure 1. Optical transmission spectra are shown for an AlN-on-sapphire template, a 0.3µm-thick $Al_{0.61}Ga_{0.39}N$ Mg-doped epilayer, and two different 0.3µm-thick Mg-SPSL structures. Both Mg-SPSL structures have a target average Al composition of 0.61 but differing periods (10Å and 20Å). The data demonstrate that a Mg-SPSL structure with an average Al composition of 0.61 replicates the transmission properties of a random alloy of the same composition.

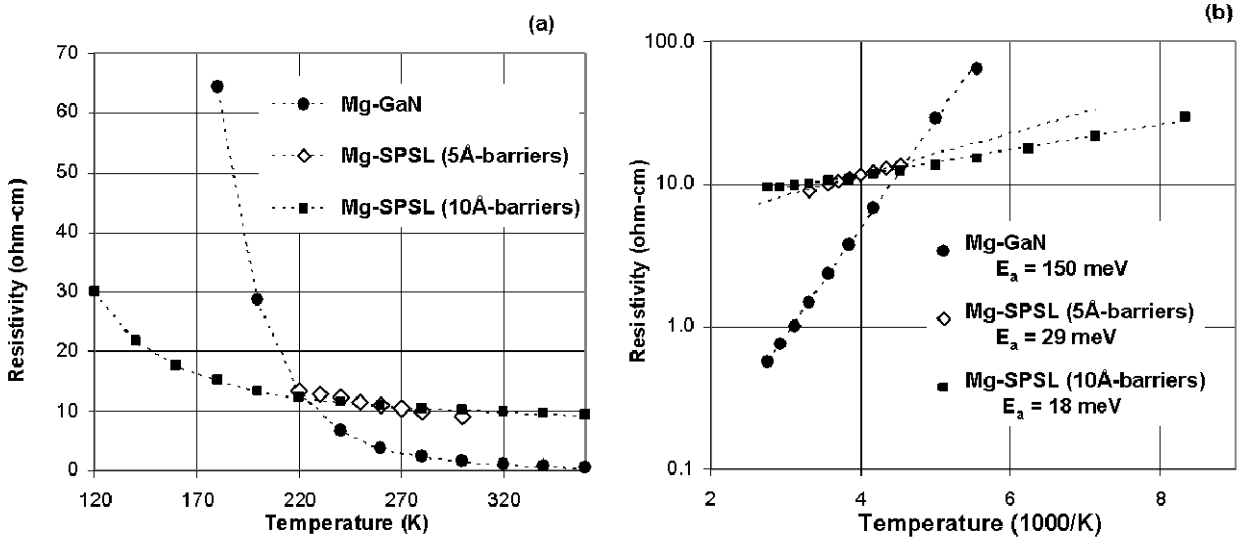

Figure 2. Resistivity vs (a) temperature and (b) inverse of temperature for p-GaN (circles), and a Mg-SPSL with 5 Å AlN barriers and 5 Å (diamonds) or 10 Å (squares) $Al_{0.23}Ga_{0.77}N$ well layers. Dashed lines in (a) are guides to the eye and in (b) are fits to the data using an Arrhenius model.

Dislocation Density Reduction in GaN Using Self-Assembled Masking Layers of Silica Microspheres

by George T. Wang and Qiming Li

Motivation—Gallium nitride (GaN) is an important semiconductor material used in light-emitting diodes (LEDs), laser diodes, and high-frequency, high-mobility, and high-power devices. Due to the lack in availability and high prices of bulk GaN substrates, GaN is typically grown heteroepitaxially on foreign substrates. The large resulting lattice mismatch results in the formation of high densities (mid-10^8-10^9 cm^{-2}) of extended defects called threading dislocations in the GaN layers. These dislocations degrade the efficiencies and lifetimes of visible LEDs, hindering the development of higher performance solid-state lighting (SSL).

Accomplishment—We have developed an innovative and inexpensive technique employing a monolayer of self-assembled silica spheres as a growth mask to achieve significant dislocation reduction in GaN epilayers on *c*-plane sapphire. Compared to conventional epitaxial lateral overgrowth (ELO) schemes currently used to reduce dislocations in GaN, this new technique is much less expensive and complex since no lithographic patterning is required. The technique involves depositing a close-packed layer of silica spheres onto a GaN epilayer grown on a substrate such as sapphire. The spheres are deposited using a Langmuir-Blodgett process which allows large-area, uniform monolayer sphere deposition. GaN is then selectively deposited through the sphere layer using selective metal-organic chemical vapor deposition (MOCVD) until a fully-coalesced film above the spheres is achieved. Figure 1 is a cross-section transmission electron microscopy (TEM) image showing GaN regrowth and coalescence through a single layer of 3 µm diameter silica spheres. Dislocations, appearing as dark vertical lines, are numerous in the initial "GaN-1" epilayer on sapphire, located beneath the sphere layer. However, upon reaching the sphere layer, the dislocations terminate, leading to a much lower dislocation density in the "GaN-2" regrowth layer coalesced above the sphere layer. Dislocations that would otherwise pass through the gaps between adjacent spheres are also seen to bend toward and terminate at the spheres, providing an additional mechanism for dislocation elimination. The dislocation densities of GaN films regrown with and without the use of the silica sphere masking layer were quantitatively determined by atomic force microscopy (AFM) and compared, as shown in Figure 2. The surface of the control GaN sample is dominated by a high density of dislocations (3.3×10^9 cm^{-2}) which manifest as pits, as shown in Figure 2(a). In contrast, a much lower density of dislocations (4×10^7 cm^{-2}) is seen on the GaN surface grown using the silica microsphere template, as shown in Figure 2(b), which represents a nearly two orders of magnitude reduction.

Significance—SSL has the potential to provide light that is much more efficient and longer-lasting that conventional technologies, resulting in huge future energy savings and reduced carbon emissions. By providing an inexpensive method for the improved growth of GaN, this technique could lead to improved efficiency and lower cost LEDs. In addition to better LEDs, this technology could also lead to improvements in other GaN-based technologies including blue laser diodes (e.g. Blu-Ray) and high-speed, high-power electronics. We anticipate that this method may be readily extended to other GaN orientations (e.g. nonpolar GaN) and substrates (e.g. Si), and even to other semiconductor materials systems.

Sponsors for various phases of this work include: DOE Office of Energy Efficiency & Renewable Energy, DOE Office of Basic Energy Sciences, and Laboratory Directed Research & Development

Contact: George T. Wang, Advanced Materials Sciences
Phone: (505) 284-9212, Fax: (505) 844-3211, E-mail: gtwang@sandia.gov

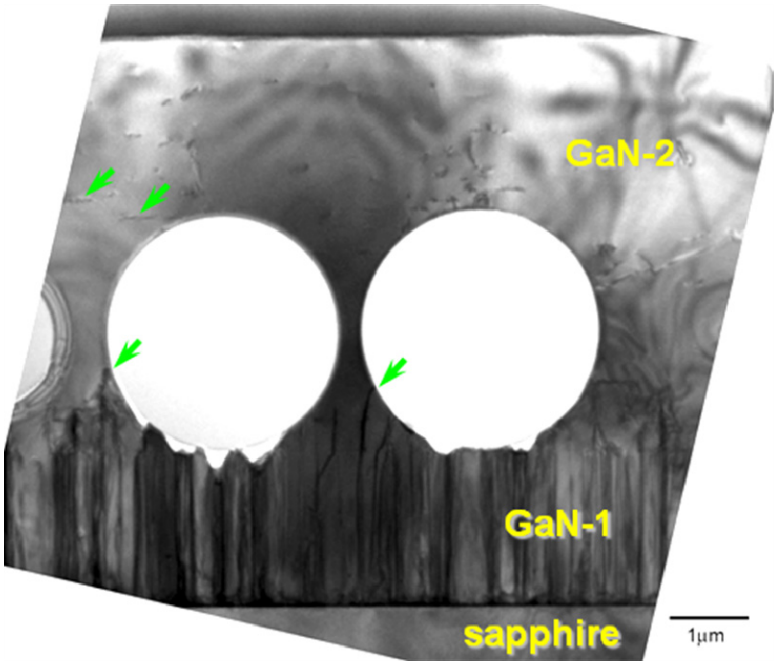

Figure 1. Cross-sectional TEM image showing GaN regrowth through a SiO_2 sphere layer. Dislocations (dark vertical lines) are seen bending towards a SiO_2 sphere and terminating at the GaN/SiO_2 interface, resulting in a low TDD film ("GaN-2") above the spheres.

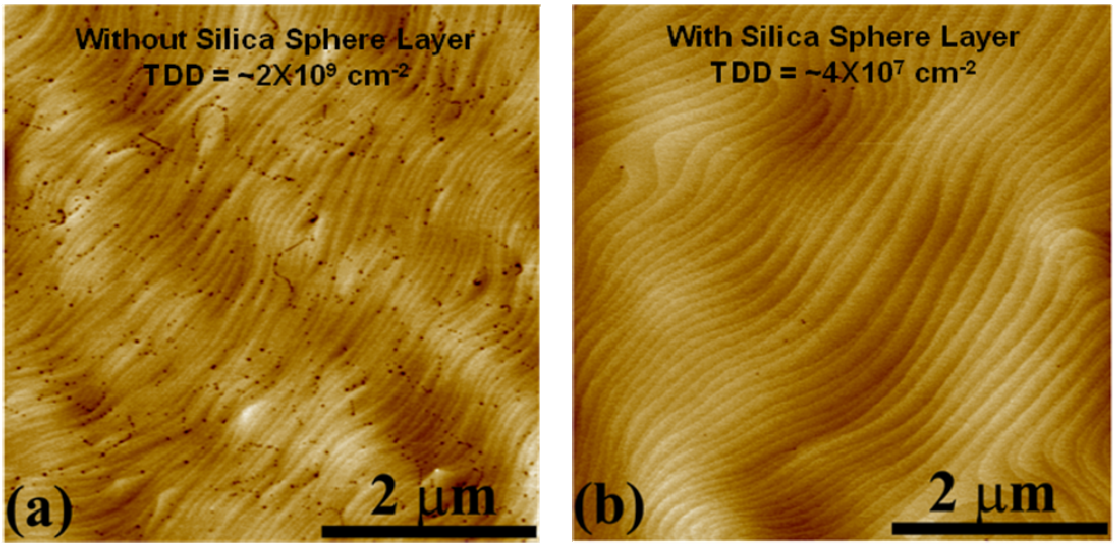

Figure 2. Typical 5×5 μm AFM scans of GaN regrown (a) without and (b) with the use of silica microspheres as a mask, which results in a nearly two-orders of magnitude reduction in dislocations (appearing as dark pits).

Science and Technology for Quantum Information Processing

Low Noise Exchange Gates in Double Quantum Dots

by Erik Nielsen, Malcolm Carroll, and Richard Muller

Motivation—Quantum computation relies on the coordinated operation of quantum bits, or qubits. In many solid-state qubit architectures, the exchange interaction is tuned in order to perform quantum operations (rotations) on the qubit. This requires precise control of the energy splitting between a spin-0 singlet state and a spin-1 triplet state, which is called the exchange energy and denoted by J. It is therefore important to understand and minimize the coupling between noise in the gate voltages and noise in J.

Accomplishment—We model a solid-state qubit formed by a pair of coupled quantum dots, called a double quantum dot (DQD), and compute the exchange energy J using a newly developed configuration interaction (CI) technique. The dots are approximated as parabolic, and the electrostatic potential is parameterized by the bias between the dots ε, half the dot spacing L, and the dot confinement energy E_0. This captures the general features of a DQD potential, and allows the technique to be easily applied to different dot materials (such as silicon and gallium arsenide) within the effective mass approximation. By applying our physical understanding of the DQD system along with the CI's ability to search large regions of parameter space quickly, we have identified regimes in which the exchange energy is relatively insensitive to variation in one or several of the electrostatic parameters determining the potential. These regimes are ideal locations for operating the qubit, since J is more robust against charge noise. We focus on regimes robust to variation in the bias energy ε, since one finds that varying ε independently of L and E_0 is more experimentally feasible than for other parameters. We have found that, within our approximation for the potential, multiple regimes exist in where J can be controlled on the energy scales necessary to perform a successful qubit rotation.

The configuration interaction method we use is more general than the Heitler-London, Hund-Mulliken, and effective Hubbard model approaches that have been used in past studies, yielding a more accurate exchange energy and capturing qualitative features that these more approximate methods miss. By using Gaussian basis functions, the CI possesses a substantial performance advantage over methods which require a large mesh, while still retaining semi-quantitative accuracy.

Significance—Understanding and mitigating the effects of charge noise in double quantum dot systems is crucial to the successful operation of a solid-state qubit. Using the CI method we have developed, it has been possible to identify the physical effects relevant to the coupling between charge- and exchange-noise, and to find specific regimes where this coupling is suppressed. The flexibility of the method makes it amenable to treating many solid-state systems, and its semi-quantitative accuracy can be used to suggest the design of qubit devices.

Sponsors for various phases of this work include: Laboratory Directed Research & Development

Contact: Erik Nielsen, Semiconductor Material and Device Sciences
Phone: (505) 844-6912, Fax: (505) 844-3211, E-mail: enielse@sandia.gov

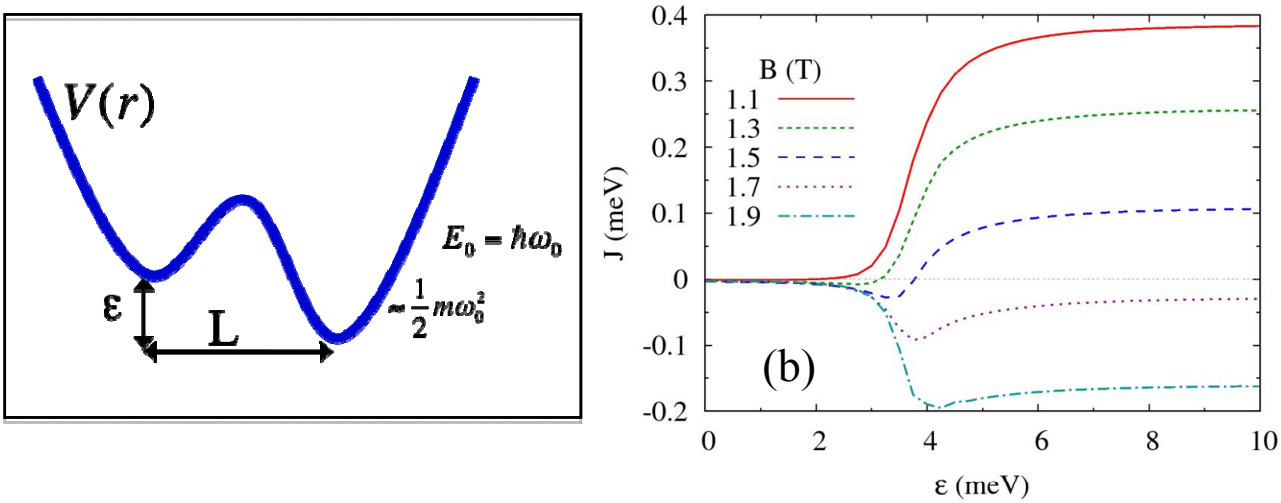

Figure 1. (a) DQD potential along x-axis showing parameters ε, L, and E_0. (b) Exchange energy as a function of bias for E_0=3meV and L=30nm. For a range of magnetic field the curve has a local minimum as well as two "flats" at high and low ε.

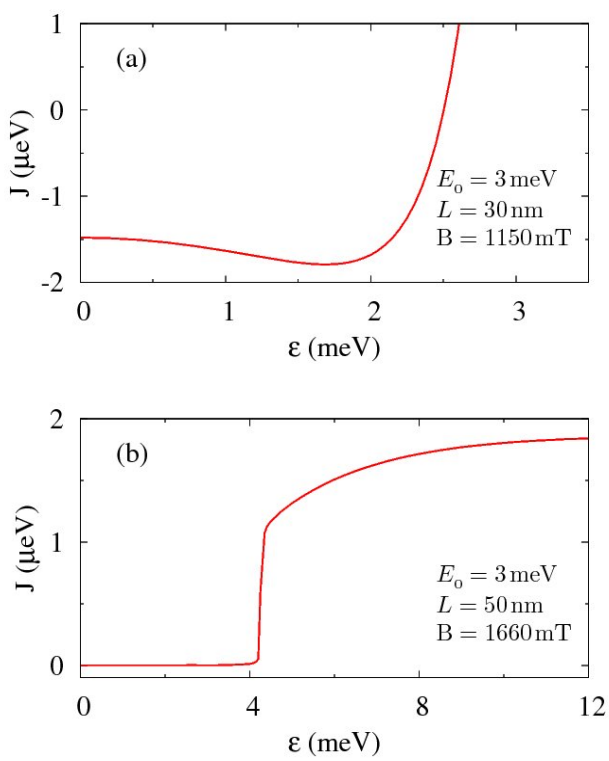

Figure 2. Exchange energy J as a function of bias in cases for where J is sufficiently robust to ε-noise that current electronics technology could produce operational quantum gates. In (a), these robust points are at ε=0 and 1.7meV, and in (b) at ε=0 and 12meV.

Observation of a Percolation-Induced 2D Metal-Insulator Transition in a Si MOSFET

by L. A. Tracy, E. H. Hwang, K. Eng, G. A. Ten Eyck, E. P. Nordberg, K. Childs, M. S. Carroll, M. P. Lilly, and S. Das Sarma

Motivation—The exact nature of the ground state of a two-dimensional electron gas (2DEG) at low temperatures is still not well understood. This is due to the complicated many-body physics involved, which is especially difficult when one tries to incorporate disorder, which is necessary in order to describe actual experimental systems. One aspect of this problem many have focused on is the temperature dependence of the 2DEG conductivity as a function of density. Varying the electron density changes the strength of electron-electron interactions relative to the kinetic energy and also varies both of these energy scales relative to the strength of the disorder. Experimentally and theoretically, there is some evidence suggesting a transition from metallic to insulating behavior upon varying the density. However, controversy exists over whether this transition is better described as an exotic, interaction-driven phase transition or by more straightforward physics of disordered conductors.

Accomplishment—We measured the temperature and density dependence of the resistivity of two MOSFET structures. In Fig. 1 we show our measured and calculated temperature and density dependent resistivity (P(T)) for sample A. The results for sample B are similar. The classic 2D metal-insulator transition (MIT) behavior is apparent in Fig. 1(a) where $\rho(T)$ for various densities shows a clear distinction between metallic $d\rho/dT > 0$ and insulating $d\rho/dT < 0$ behavior separated by a critical density $n_c \sim 1.4 \times 10^{11}$ cm^{-2}. In Fig. 1(c) and (d) we show our theoretically calculated $\rho(T)$ where the Boltzmann transport is calculated using the screened charged impurity scattering as the only resistive scattering mechanism [1]. Although the ratio of the Coulomb to Fermi energy can be as large as ~ 15 near the MIT for this sample, suggesting that Coulomb interactions could play an important role, we note that the basic features of the experimental metallic phase are well-captured by the screening theory.

In Fig. 2 we plot our measured conductivity as a function of n to see if a percolation behavior, $\sigma \propto (n - n_p)^p$, where n_p and p are the percolation transition density and exponent, respectively, is manifested. Our fit yields $p \sim 1.20$, $n_p \sim 1.2 \times 10^{11}$ cm^{-2} for sample A and $p \sim 1.24$, $n_p \sim 2.0 \times 10^{11}$ cm^{-2} for sample B. Our values for the exponent p are fairly close to the expected theoretical value of 1.31.

Significance—Our work provides the first experimental data together with theoretical calculations that show that the 2D MIT in a Si MOSFET can be explained by percolation physics. Our data and theoretical analysis show that the temperature dependence of the observed metallic state can be described by a finite-temperature semi-classical Boltzmann screening theory and that the density dependence of our resistivity data is consistent with a percolation model.

[1] S. Das Sarma and E. H. Hwang, *Phys. Rev. Lett.* **83**, 164 (1999).

Sponsors for various phases of this work include: Laboratory Directed Research & Development

Contact: Lisa A. Tracy, Semiconductor Material and Device Sciences
Phone: (505) 284-8567, Fax: (505) 284-7778, E-mail: latracy@sandia.gov

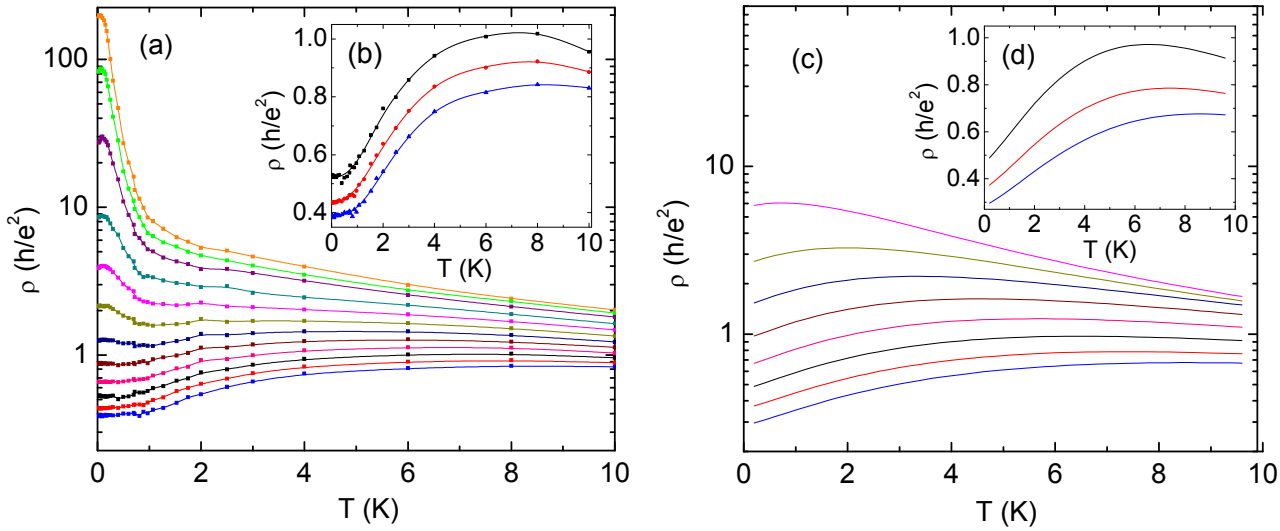

Figure 1. (a) Experimental resistivity ρ in units of h/e^2 as a function of temperature for sample A at 2D electron densities (from top to bottom) n = 1.07, 1.10, 1.13, 1.20, 1.26, 1.32, 1.38, 1.44, 1.50, 1.56, 1.62, and 1.68 × 10^{11} cm^{-2}. Inset (b) Enlarged view of data in the effective metallic regime at n = 1.56, 1.62, and 1.68 × 10^{11} cm^{-2}. Solid lines are guides to the eye. (c) Theoretically calculated temperature and density dependent resistivity for densities n = 1.26, 1.32, 1.38, 1.44, 1.50, 1.56, 1.62, and 1.68 × 10^{11} cm^{-2} (from top to bottom). Inset shows the resistivities for n = 1.56, 1.62, and 1.68 × 10^{11} cm^{-2}.

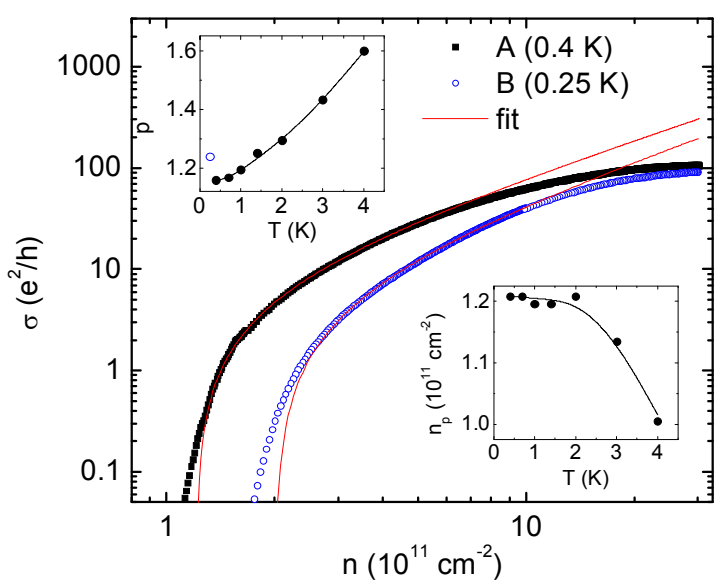

Figure 2. (a) Main plot: Points show experimental conductivity σ in units of e^2/h versus electron density n for sample A at T = 0.4 K (closed symbols) and B at T = 0.25 K (open symbols). The solid lines are fits to the data of the form $\sigma = A(n - n_p)^p$. The upper and lower insets show the exponent p and critical density n_p, respectively, as a function of temperature for sample A. Solid lines are a guide to the eye. The open symbol in the upper inset shows p for sample B at T = 0.25 K.

Charge Sensing in Silicon Metal-Oxide-Semiconductor Quantum Dots

by E.P. Nordberg, H.L. Stalford, R. Young, G.A. Ten Eyck, K. Eng, L.A. Tracy, K.D. Childs, J.R. Wendt, R.K. Grubbs, J. Stevens, M.P. Lilly, M.A. Eriksson, and M.S. Carroll

Motivation—In recent years, semiconductor lateral quantum dots have emerged as an appealing approach to quantum computing. The demonstration of electrically controlled spin qubits in GaAs/AlGaAs heterostructures and spin blockade within Si systems are recent advances toward that goal. Silicon offers the potential for very long spin decoherence lifetimes in both donors and quantum dots. The Si metal-oxide-semiconductor (MOS) system features highly tunable carrier densities and the possibility of very small dot sizes, as well as providing further opportunities to couple single donors to gated quantum dots

Accomplishment—Silicon MOS nanostructure devices are fabricated using a version of the CINT Electrical Transport Discovery Platform. In the Microelectronics Development Lab, silicon wafers are fabricated (Figure 1a,b) with a stack that included ohmic contacts, a high quality thermal oxide, a doped poly-silicon layer and a region for additional nanolithography (Figure 1c). In order to operate sub-100 nm structures, the poly-silicon gate is patterned using electron beam lithography and subsequent dry etching. A negative voltage expels electrons from the depletion gate regime and defines the nanostructure. Field-effect based devices also require a positive gate voltage to induce electrons at the silicon-silicon oxide interface, and this is implemented using a separate overall Al top gate (Figure 1d). The top gate and depletion gates are electrically isolated with atomic layer deposition of aluminum oxide.

The device shown in Figure 2a is designed as a double quantum dot (gates B-F,H) with narrow constrictions to the left and right of the double dot regime (gates A-B and F-G). In future experiments we plan to use the full double dot structure, but for the charge sensing demonstration we use the gates highlighted in red to form a single quantum dot (D-F and H) with an integrated charge sensor (F-G). The quantum dot has approximately 100 electrons, and a negative bias on the plunger gate, E, reduces the electron number of the dot by a single electron every 43 mV. The electron addition can be observed directly by monitoring the transport through the dot (Figure 2c, red line). Each time an electron energy level aligns with the reservoirs, the current increases and when the levels are not aligned the dot conductance is blocked. The point contact constriction can be used as a remote sensor for the changes in electron number (Figure 2c, black line). For a fixed bias, the current changes by approximately 3% every time the electron number in the dot changes. The charge sensor can effectively measure changes in electron occupation even when the direct conductance through the dot is too small to observed Coulomb blockade (V_E<-1 volt)

Significance—Spin quantum computing in semiconductors requires working with single electrons in quantum dots. In this regime it is important that no current flow through the dot. The successful demonstration of a point contact electrometer in a silicon MOS nanostructure is a critical element to both reducing the electron number to one, and eventually for measuring the spin using a spin-to-charge transduction technique. This approach is also compatible with sub-microsecond single electron measurements using an rf-SET approach.

E. Nordberg, *et al.*, Appl. Phys. Letters **95**, 202102 (2009).

Sponsors for various phases of this work include: Laboratory Directed Research & Development and DOE Office of Basic Energy Sciences

Contact: Michael Lilly, Center for Integrated Nanotechnologies Science
Phone: (505) 844-4395, Fax: (505) 844-3211, E-mail: mplilly@sandia.gov

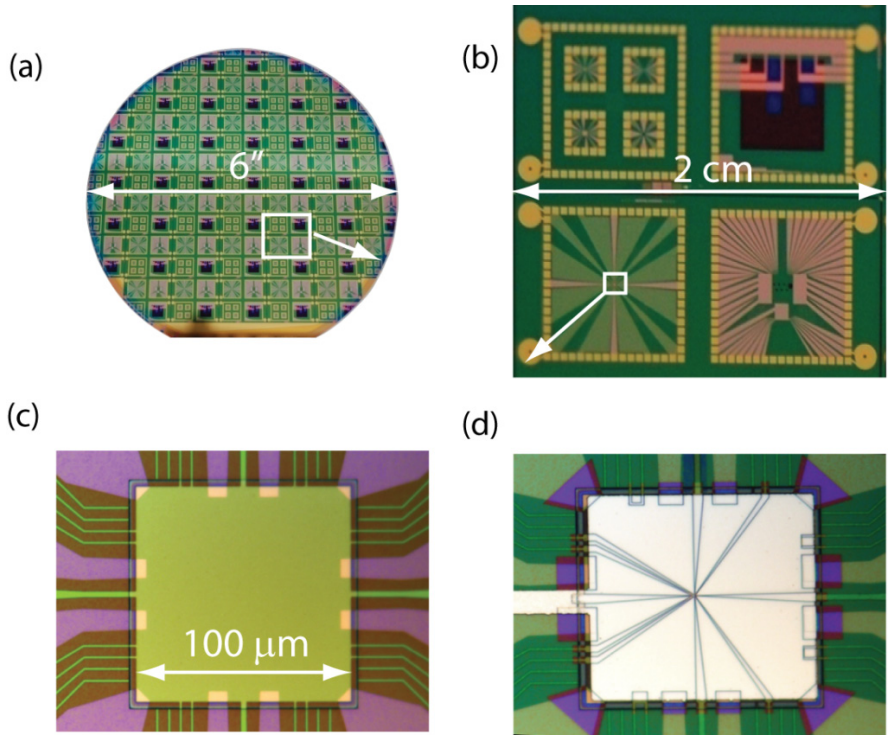

Figure 1. (a) Front-end 6 inch silicon wafer with many MOSFET structures. (b) 2 cm die with 4 quadrants for back-end nanolithography. (c) 100 micron poly gate (green) ready for depletion gate patterning. Ohmic contact to the 2D electrons are purple. (d) Same region after electron beam lithography, Al2O3 and top Al gate.

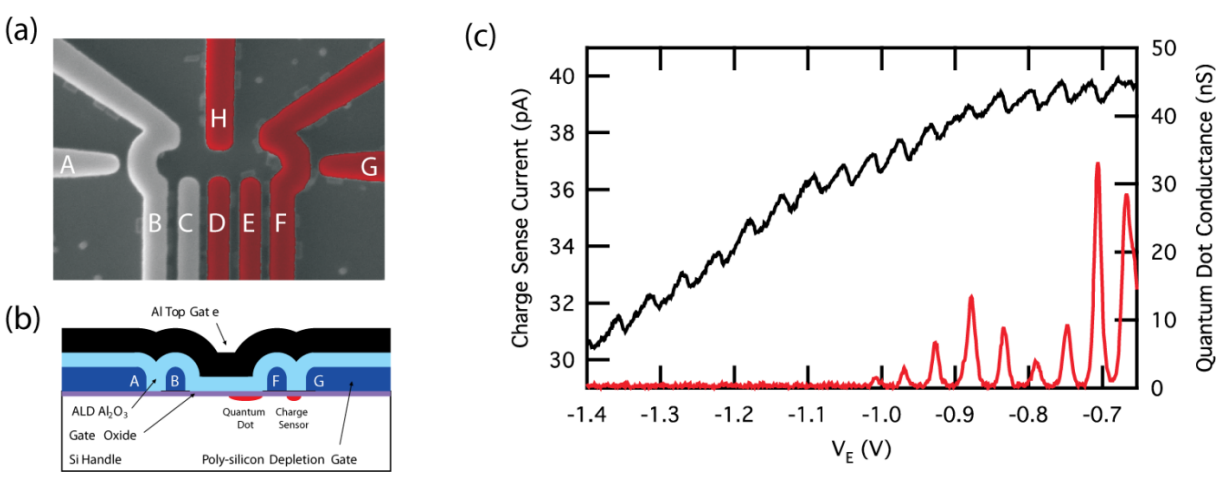

Figure 2. a) Double quantum dot is defined by depletion gates (B-F and H); integrated electrometers are the point contacts defined by A-B and F-G. (b) Cross section of double gated MOSFET layers with the dot and point contacts represented schematically. (c) Coulomb blockade peaks in a many-electron single dot (defined by H,D,E and F). The compensated charge sensor current shows a step each time another electron is added to the dot.

Observation of a Possible New Non-Abelian Quantum Hall State

by Wei Pan

Motivation—When two identical particles are exchanged, if they are bosons (for example, photons) the wavefunction is unchanged; if they are Fermions (for example, electrons) the wavefunction changes sign. If the two particles are the so-called non-Abelian particles, not only is the wavefunction changed but also the order of exchange of multiple particles becomes relevant, as shown in Fig.1. This topological degree of freedom is insensitive to local perturbations and can be utilized for achieving fault-tolerant quantum computation, which promises an exponential increase in computing power over a classical computer.

It is now generally believed that the quasiparticle excitations of the even-denominator fractional quantum Hall effect (FQHE) state at Landau level filling factor ν=5/2 may obey exotic non-Abelian statistics. Observations of other non-abelian even-denominator FQHE states have been rare beyond the ν=5/2 state more than twenty years since its discovery. On the other hand, an observation of a new non-Abelian FQHE state would not only be of interest by itself, but may also further elucidate the still enigmatic ν = 5/2 state.

Accomplishment—Recently, a new even-denominator FQHE state at ν=1/4 was observed in magnetic fields up to 45T in a high quality $Al_{0.24}Ga_{0.76}As/GaAs/Al_{0.24}Ga_{0.76}As$ modulation doped quantum well. The two-dimensional electron density of the sample was $n = 2.55 \times 10^{11}$ cm^{-2} and the mobility $\mu \sim 10^7$ cm^2/Vs. In Fig. 2 we display R_{xx} and R_{xy} as a function of perpendicular magnetic field ($B_\perp$) for $\theta = 0$ and $\theta = 20.3°$. A FQHE state is present at ν=1/2 with both a minimum in R_{xx} and a weak plateau in R_{xy}. This FQHE state becomes fully developed at $\theta = 20.3°$ with R_{xx} vanishingly small and R_{xy} precisely quantized at $2h/e^2$. Moving to higher magnetic fields, in the absence of tilt, a kink is noticeable in R_{xx} at ν=1/4 along with a very subtle deviation from the classical Hall slope in R_{xy}. With the sample tilted to $\theta = 20.3°$ degrees the kink at ν=1/4 in R_{xx} has developed into a well defined minimum on top of the rising background and a plateau has emerged in R_{xy}, indicating a FQHE state at ν=1/4. Furthermore, the comparison between the derivative of the Hall resistance $dR_{xy}/dB_\perp$ and R_{xx} also corroborates the formation of a ν=1/4 FQH state.

The nature of this FQHE state is not known at the present time and many theoretical models have also been proposed. More work is needed to address the question whether it is a non-abelian state, or an abelian two component state, or a non-abelian generalization of the two component state.

Significance—The non-Abelian FQHE states are at the center of current interests due to their potential applications in performing topological quantum computation. There has been an ongoing effort to discover more FQHE phases whose elementary excitations exhibit non-Abelian statistics. It can be expected that the observation of the new FQHE state at ν=1/4 will impact and stimulate a great deal of developments in theoretical physics and in quantum computing.

Sponsors for various phases of this work include: DOE Office of Basic Energy Sciences

Contact: Wei Pan, Semiconductor Material and Device Science
Phone: (505) 284-9545, Fax: (505) 844-3211, E-mail: wpan@sandia.gov

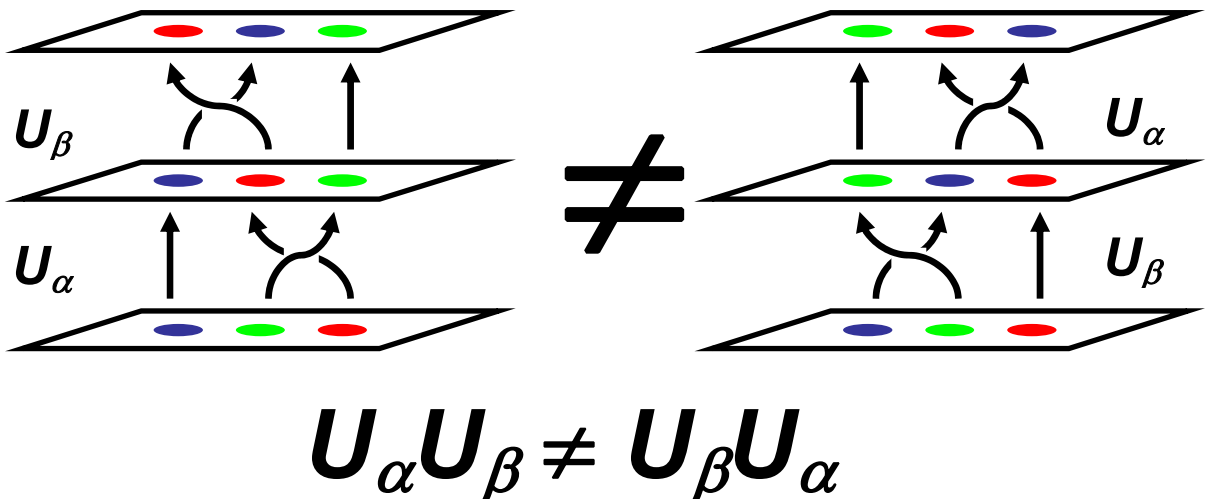

Figure 1. Shows schematically that the order of interchange of two particles is relevant for non-Abelian particles.

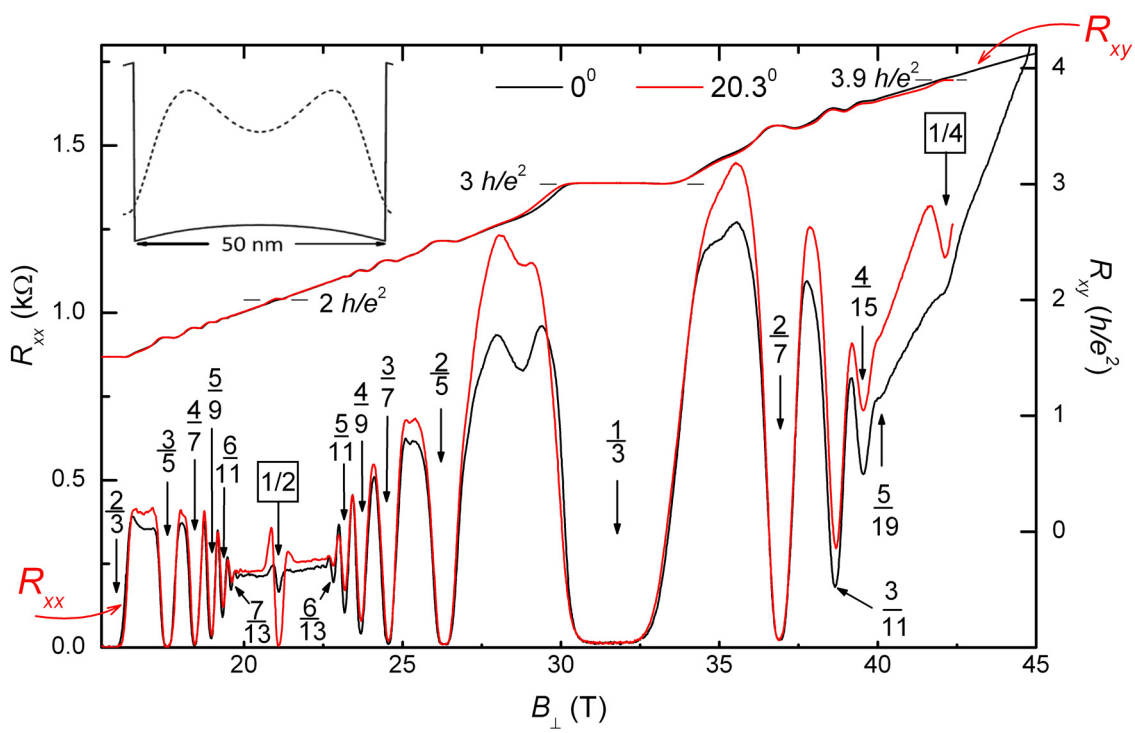

Figure 2. R_{xx} and R_{xy} as function of perpendicular magnetic field, $B_\perp$, for θ=0° and 20.3° at T ~ 35 mK. Some of the odd-denominator FQH states are labeled. The filling factors ν=1/2 and ν=1/4 are also marked. The horizontal lines at $R_{xy}=2h/e^2$, $3h/e^2$ and $3.9h/e^2$ highlight the plateaus at those values.

Advancements in Single Ion Geiger Mode Avalanche Photodiodes (SIGMA) Detectors for the QIST Grand Challenge

by E. Bielejec and M. S. Carroll

Motivation—Electronic devices that are designed to use properties of single atoms such as donors or defects have recently shown great promise with recent demonstrations of donor spectroscopy, single photon emission sources, and magnetic imaging using defect centers in diamond. In building single atom devices one of the key issues is the detection of the arrival of a single donor atom during the implantation step. We propose avalanche photodiodes (APD to detect the arrival of a single atom. APDs have been used to sense single e-h pairs generated by the arrival of single photons through the use of passively gated Geiger mode (GM) operation of the APD. Over the last two years, we have demonstrated single ion detection at 300 and 77K using similar techniques. Single ion Geiger mode avalanche diode (SIGMA) detectors operate by over-biasing past reverse breakdown for a short time period (which we call the gating window) during which the detector can be sensitive to a single electron or hole injected into the junction. The high fields produce an avalanche cascade leading to a Geiger signal. The gating window can coincide with a pulsed ion beam configuration to insure that the detector is on when an ion is expected to arrive. A challenge in this configuration is the high number of dark counts, due to thermally generated e-h pairs, that obscures the detection of a single ion arrival. Furthermore, extension of the lateral sensitivity using this approach has not been well established. Increased flexibility in remote lateral sensing is important for future integration with single donor device with additional nanostructures such as a double quantum dot structure.

Accomplishment—We report a mapping of the remote lateral sensing of the SIGMA detector combined with demonstrating a significant reduction in dark count. A dark count reduction by three orders of magnitude was accomplished through the introduction of a 77K cooled stage (see figure 1). The mapping of the lateral sensitivity was determined using the ion beam induced current (IBIC) response of the detectors. The lateral sensitivity of the SIGMA detector with a ~150 μm diameter has an estimated upper bound of 600 e-h pairs while maintaining 100% detection efficiency, within the uncertainty of the measurement (see figure 2). The SIGMA sensitivity provides a means of detecting lower energy ions (i.e., smaller straggle) and greater flexibility in the layout of single ion detector integration with the single donor device construction zones.

Significance—We have reported single ion detector performance at 300 and 77K that represents progress towards laterally remote, low energy (i.e., minimum straggle), single ion implant detection for single donor device fabrication. Detection of remote single ion strikes at least as far as ~75 μm from the ion detector with 100% detection efficiency is demonstrated. In principle, this lateral sensitivity provides a sufficiently large region to construct future single ion implanted Si devices. The detector sensitivity is bounded at ~600 e-h pairs which extends ion detector sensitivity to lower energies than previously reported and leads to potentially smaller ion straggle (i.e., improved longitudinal control in atom placement). The ion detector false count probability is significantly decreased by 77 K operation, leading to a drop from 10^{-1} to 10^{-4} false count probability at 300 and ~77K respectively. This reduction in false count probability has important implications for using this approach to reliably implant single ions.

Sponsors for various phases of this work include: Laboratory Directed Research & Development and National Security Agency Laboratory for Physical Sciences under contract number EAO-09-0000049393

Contact: Edward S. Bielejec, Radiation-Solid Interactions
Phone: (505) 284-9256, Fax: (505) 844-7775, E-mail: esbiele@sandia.gov

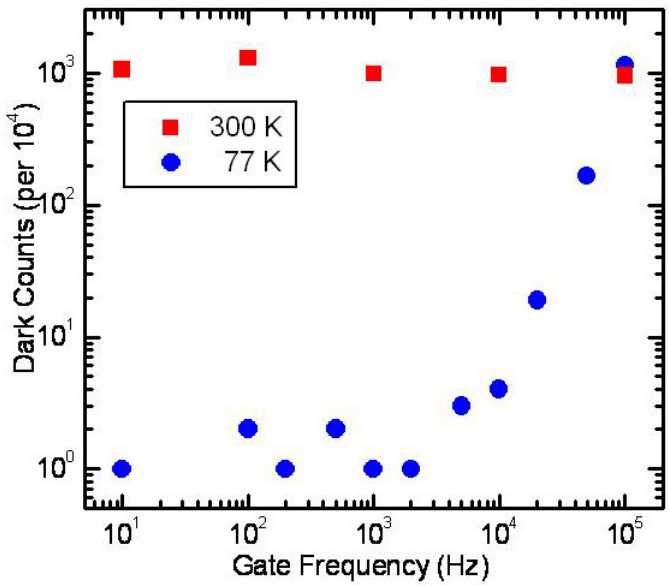

Figure 1. The dark counts from 10^4 gatings of the SIGMA detector with individual durations of 230 ns, pulsing 6.5 V past breakdown, as a function of the gate frequency taken at 300 K (squares, red) and LN_2 temperature (circles, blue).

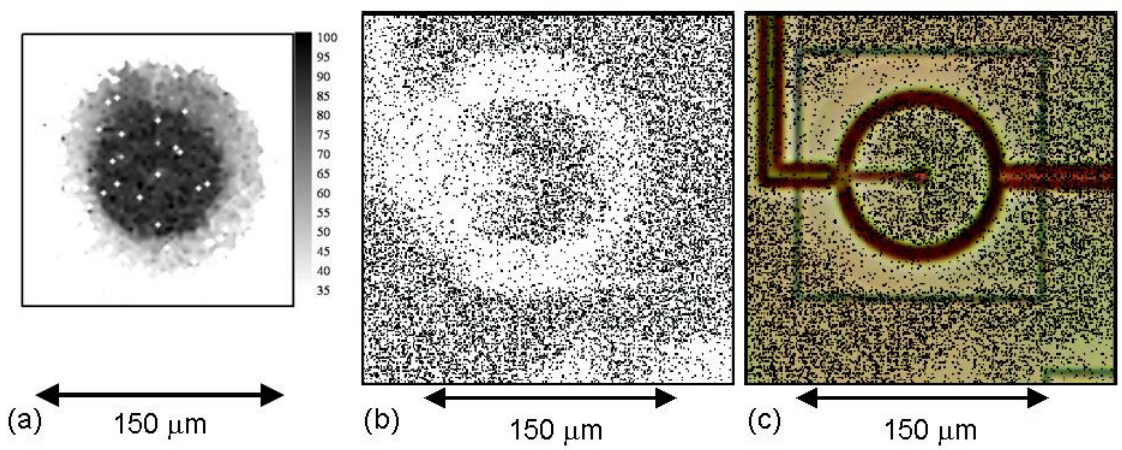

Figure 2. (a) The charge collection efficiency percentage of the APD in the SIGMA detector at zero bias as determined from IBIC with 250 keV H^+. Only inside the APD is the collection efficiency greater than the noise floor of 35%. (b) The digital IBIC map from the GM operation of the SIGMA at liquid nitrogen temperature. (c) GM-IBIC map superimposed upon a micrograph of the SIGMA detector. The low detection efficiency ring correlates with the anode metal contact and a heavily doped n^+ gettering ring.

Highlights in Condensed Matter Science

Superplastic Salt Nanowires

by N. W. Moore, J. E. Houston, and J. Y. Huang, in Collaboration with the S. X. Mao Group at U. Pittsburg

Motivation—Ions and nanometer-sized crystals of common salt (sodium chloride) play key roles in applications like water purification, the stability of rock salt for carbon sequestration and underground nuclear waste disposal, and for seeding atmospheric reactions. For example, it is now recognized that changes in crystal morphology can affect the reactions of sea salt aerosols, which have been implicated in problems as broad as smog formation, ozone destruction, and triggering asthmatic responses in humans.

Accomplishment—Experiments first aimed at understanding how water adheres to salt surfaces for desalination applications led to the surprising discovery that superplastic nanowires could be pulled from the surface of ordinary table salt*. In the initial experiments, the Sandia-developed interfacial force microscope (IFM) showed an unusual adhesive force when a sharp diamond tip approached within a few nanometers of a salt crystal. This adhesive force remained as the tip withdrew, suggesting that the tip was pulling long tendrils of salt from the crystal surface. Similar adhesion experiments with sharp gold tips in a transmission electron microscope (TEM) confirmed that superplastic nanowires could be pulled from the salt surface (Figure 1). The nanowires could be stretched >2 μm, or 280% of their original length, and could be bent >90° upon compression. As they were pulled, the nanowires necked down, rather than fracturing, as if the salt crystal were more akin to chewing gum than a brittle solid (Figure 2). Yet elemental analysis confirmed that the nanowires were indeed comprised of NaCl.

Superplasticity, or elongation to failure >100%, is a rare material property at room temperature, and even more rare for ionic crystals, having been seen for only a few compounds. That table salt can stretch into nanowires comes as a surprise, because one is accustomed to the tiny salt crystals shaken onto food, and which appear brittle and shatter like glass into small pieces upon crushing.

One key to understanding the super-elongation is the disruption of the regular arrangement of Na^+ and Cl^- ions in the salt crystal lattice. In the TEM measurements, the electron beam used to image the sample creates holes in the crystal lattice, opening spaces for ions to rapidly migrate and "heal" the nanowire as it elongates. Chemical analysis shows that the beam also reduces a small fraction of the Na^+ ions in the salt to metallic Na, which enhances ductility. In the IFM experiments, mechanical and adhesive perturbations are believed to disrupt the surface's native crystallinity.

Significance—This is the first demonstration of superplasticity in an ionic material at the nanoscale. Other materials that neck into nanowires far below their melting point have all been metals (e.g., gold, lead). Furthermore, the behavior of low-temperature-deforming, one-dimensional nanomaterials, such as carbon nanotubes and ceramic nanowires, would not have predicted similar behavior in ionic nanowires. The discovery may inspire new ways to create nanostructures through mechanical pulling or dissolvable templates. This work also raises broad questions about the presence of nanomaterials in the environment and their unseen influences. More fundamentally, the idea that common salt can be superplastic is a striking and unexpected example of how material properties can change when structures are reduced to nanoscale dimensions.

* Nano Letters 9(6), 2295 (2009).

Sponsors for various phases of this work include: DOE Office of Basic Energy Sciences and Laboratory Directed Research & Development

Contact: Nathan W. Moore, Surface and Interface Sciences
Phone: (505) 844-0278, Fax: (505) 844-5470, E-mail: nwmoore@sandia.gov

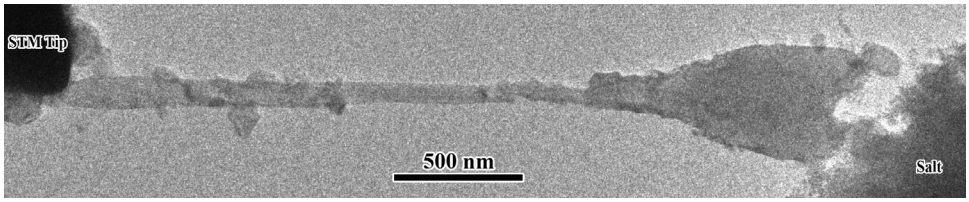

Figure 1. TEM image of a typical salt nanowire created after touching a gold tip to a salt crystal.

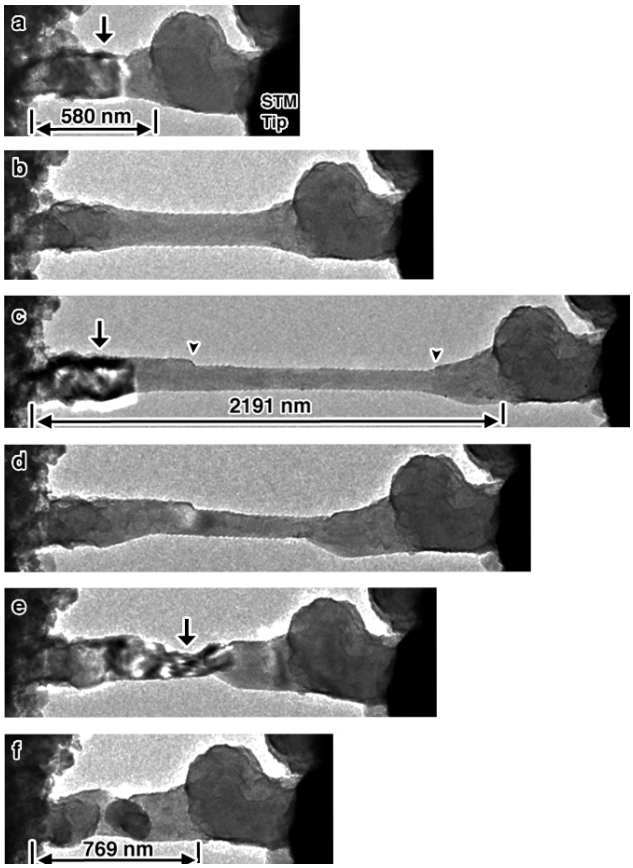

Figure 2. Time-lapsed TEM images showing super-elongation and subsequent compression of a nanowire (a → f; time = 0, 256, 502, 583, 684, and 744 sec., respectively). The gold STM tip (not shown) is adhered to the NaCl grain at the right side of these images. Arrows point to examples of steps and crystalline contrast on the nanowire surface. Roughness of the NaCl surface (left) appears exaggerated by the transverse imaging direction, which contracts the image.

The Role of Carbon Surface Diffusion on the Growth of Epitaxial Graphene on SiC

by Taisuke Ohta, N. C. Bartelt, Shu Nie, Konrad Thürmer, G. L. Kellogg

Motivation—Graphene is regarded as one of the candidate materials for post Si-based electronics. Its unique electronic properties have stimulated the development of synthesis routes for improved film quality. Graphitic films form readily on silicon-carbide (SiC) surfaces: sublimation of Si at elevated temperature leaves behind a high concentration of carbon atoms, which assemble ("graphitize") into graphene layers. The recent approach to higher quality films involves heating in argon at atmospheric pressure [K. V. Emtsev *et al.*, Nature Materials, 8, 203 (2009)]. This new approach leads to significant improvement in domain size and electronic properties compared to previously reported vacuum graphitization and call for comprehensive understanding of the kinetic pathways underlying this growth process.

Accomplishment—We have observed the formation of graphene on SiC by Si sublimation in an Ar atmosphere using low energy electron microscopy (LEEM), scanning tunneling microcopy (STM) and atomic force microscopy. Our work reveals that the growth mechanism depends strongly on the initial surface morphology and that carbon diffusion governs the spatial relationship between SiC decomposition and graphene growth.

Two examples of the growth fronts are shown in Figs. 1 and 2: isolated bilayer SiC steps generate narrow ribbons of graphene (Fig. 1), whereas triple bilayer steps allow large graphene sheets to grow by step flow (Fig. 2). The dark narrow regions in Fig. 1 (a) are single layer graphene, and the rest of the surface is the interface carbon-rich layer (so-called buffer layer) shown using LEEM. These graphene-terminated regions commonly appear as distinctive parallel ribbons forming arrow-shape geometry, which ultimately provide particular insight into the carbon diffusion process. We have developed a steady-state diffusion model of an arrow feature based on our LEEM and STM observations (Fig. 1 (c) and (d)), which indicates the diffusion-limited growth process and the low carbon attachment barrier at the growth front. The qualitatively different role of carbon diffusion is seen near receding triple SiC bilayer steps. A sequence of LEEM images of such a step (imaged in real-time at elevated temperature, >1080 C) is displayed in Figs. 2 (a) and (b). Here the graphene (medium gray) grows in a continuous step flow mode, where the carbon atoms emitted from the step edges can be immediately consumed at the growth front of graphene.

Significance—The graphitization process on SiC differs from normal epitaxial growth in that the source of carbon atoms is the substrate itself. Thus, different fundamental issues, such as how and where carbon atoms are created and how far they have to diffuse on the surface to form graphene layers need to be addressed. Our work establishes the fundamental role of carbon diffusion and revealed that there exist well-defined spatial relationships between where SiC is decomposed and how and where graphene grows. We also demonstrated that this high-temperature growth process can be revealed in real-time through LEEM observation, which will play a key role in further understanding the atomistic processes of this unique epitaxial growth.

Sponsors for various phases of this work include: Laboratory Directed Research & Development; DOE Office of Basic Energy Sciences, Division of Materials Science & Engineering, and Center for Integrated Nanotechnologies (DE-AC04-94AL85000).

Contact: Taisuke Ohta, Surface and Interface Sciences
Phone: (505) 284-3167, Fax: (505) 844-5470, E-mail: tohta@sandia.gov

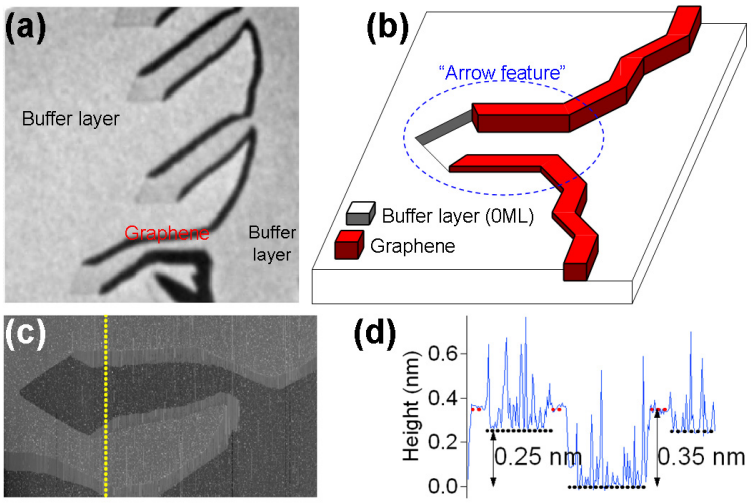

Figure 1. Morphology of the "arrow feature." (a) LEEM image (4.2x4.2μm^2) using incident electrons of E_{vac}+2.85 eV, where E_{vac} is the vacuum level. The dark grey regions consist of a graphene monolayer, and the light gray regions are buffer layer. (b) Schematic representation of an arrow feature. The red and white regions are graphene (1ML) and the interface carbon-rich layer (co-called buffer layer, and indicated as 0ML), respectively. (c) STM image (1.8x1.05 μm^2) with the cross section along the yellow line (d). Red and black dotted lines in (d) denote 1ML graphene and buffer layer regions.

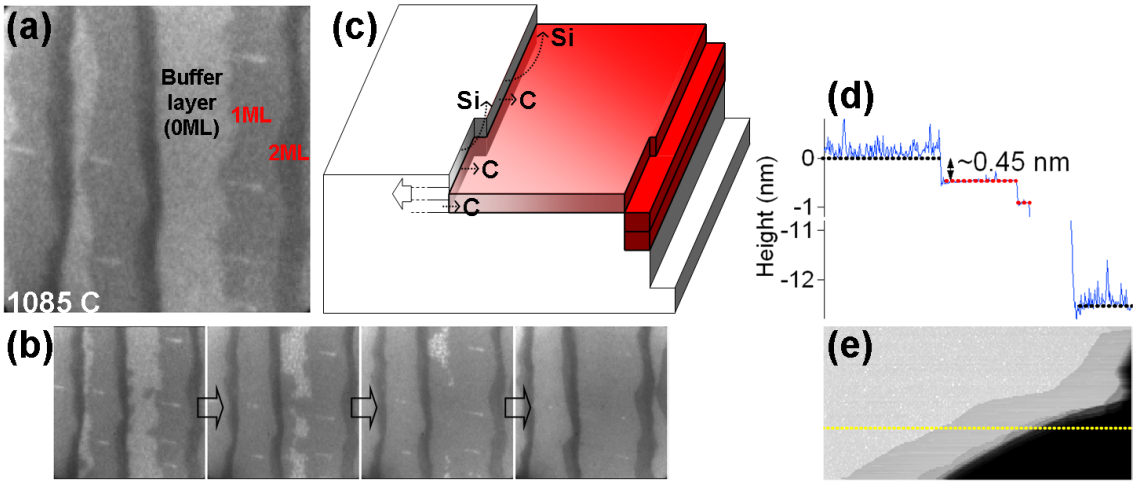

Figure 2. Step-flow growth of graphene layers. (a) and (b) Evolution of graphene growth observed in LEEM (3.5x3.5 μm^2) in an ultrahigh vacuum condition. The dark grey regions consists of >2ML of graphene, the medium grey regions are graphene monolayer, and the light gray regions are buffer layer. (c) Schematic illustration of the step-flow growth. The red and white regions are graphene (1ML and 2ML) and the buffer layer (0ML). Triple SiC bilayer (as indicated as discontinued lines) is transformed into a single graphene layer. (d) The cross section of the STM image in (e). (e) STM image (4x2 μm^2) of the sample with monolayer and bilayer graphene growing from the bunched step edge.

Isothermal Magnetic Advection: Functional Flows for Heat and Mass Transfer

by James E. Martin and Kyle Solis

Motivation—Thermal transport by convection cells was first visualized in 1900 by Henri Bénard, in an experiment wherein a thin layer of liquid with a free top surface was heated from below. This experiment produced a hexagonal pattern of flow cells that Bénard attributed to the buoyancy of the fluid near the hot surface. In 1916 Rayleigh obtained a theoretical understanding of the experimental conditions that give rise to "Rayleigh-Bénard" convection—at least for the case where the liquid surfaces are bounded by contacting plates—and predicted convective rolls, circles, and linear and square patterns. In 1970 it was discovered that applying a magnetic field gradient along the thermal gradient could enhance natural convection in magnetic fluids. The enhancement is dependent upon the thermal gradient and does not lead to new flow patterns. We have now discovered a method of stimulating heat and mass transport in fluids that requires neither a thermal or magnetic field gradient, nor gravity. This method gives rise to a unique class of vigorous, magnetic field-controllable flow patterns we call *advection lattices*, which can be used to transport heat or mass along any desired direction, using only the modest fields produced by Helmholtz coils.

Accomplishment—The formation of advection lattices occurs when a suspension of magnetic platelets is subjected to time-dependent, *biaxial* magnetic fields comprised of two orthogonal components whose frequency ratio can be expressed as a ratio of small integers. For such *just intervals*—octaves, perfect fourths and fifths, major thirds, etc.—a variety of flow patterns can be produced whose structure is largely determined by the phase between field components. These patterns consist of a checkerboard of anti-parallel flow columns that are normal to the plane of the biaxial field, Figure 1. With the platelets we employ, vigorous flow patterns are produced with field frequencies in the low audio range.

The simplest flow pattern we have observed occurs with an octave biaxial field having a phase angle of 45°. (This phase angle is added to the high-frequency component with both components expressed as sines.) Applying this field to the platelet suspension immediately stimulates the striking flow pattern in Figure 2 (left), which consists of 1.3 mm diameter flow columns that span the 3 cm cell. Each column has a sharp tail and a diffuse tip, with the flow running from tail to tip. Tracer particle studies show that the flow rate is about 3 $cm \cdot s^{-1}$, and that adjacent columns flow in opposite directions. Figure 2 (right) shows that these columns pack "antiferromagnetically" into a rectangular lattice. This symmetric flow pattern is unique to this effect and does not occur in Rayleigh-Bénard convection, presumably because gravity breaks up-down symmetry.

Significance—Isothermal magnetic advection is a useful technology that enables the transfer of heat and mass without pumps, seals or contact with the fluid—even in microgravity environments—and regardless of the magnitude of the thermal gradient. It can also be used to transfer mass without transferring heat, since the column size is frequency tunable, and thus can be small enough that the flow columns act as a counter-current heat exchanger without pipes. Understanding the unique symmetries of the flow patterns is a scientific challenge, and we have only begun to explore the experimental possibilities.

Sponsors for various phases of this work include: DOE Office of Basic Energy Sciences

Contact: James E. Martin, Nanomaterials Sciences
Phone: (505) 844-9125, Fax: (505) 844-5470, E-mail: jmartin@sandia.gov

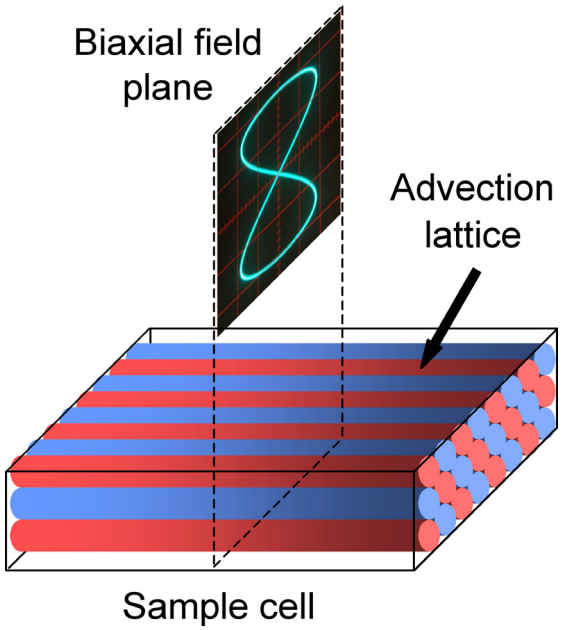

Figure 1. Advection lattice and biaxial magnetic field geometry. The flow columns form normal to the magnetic field plane. In this case the field components are a 2:1 frequency ratio.

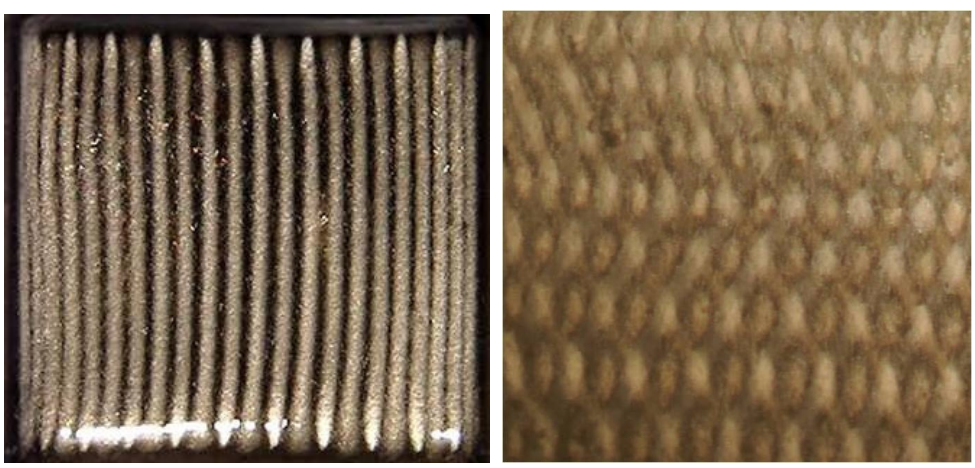

Figure 2. Morphology of an advection lattice. **(left),** View in the plane of the magnetic field of the advection lattice for an octave field (75 and 150 Hz components with rms amplitudes of 150 G) at a 45° phase angle. The pattern is insensitive to the boundaries, and the flow runs from the sharp column tails to the diffuse tips. **(right)** View of the advection lattice normal to the field plane shows the columns form a rectangular lattice.

Adatom and Addimer-Mediated Exchange Diffusion in the Ge/Si(001)Surface Alloy

by E. Bussmann and B. S. Swartzentruber

Motivation—In Si-Ge thin films, the influence of the composition on the morphology, electronic, and optical properties is widely exploited for technological purposes. At the Si(100) surface, Ge alloying is used to tune the bandgap and charge mobility for micro- and opto-electronic device applications. The Ge-Si(100) surface is also a model system for studying alloy growth, the role of strain in epitaxy, and self-organization of nanostructures. In the initial stage of Ge-Si(100) epitaxy, Ge embeds into the surface at apparently random substitutional sites to form a surface alloy, driven by the resulting reduction in surface stress. Many studies have examined the early stages of the growth process, making inferences about the most likely mechanisms of surface alloy formation and structure, however, the atomistic processes involved in Ge embedding have not been observed directly by an atomic-resolution technique.

Accomplishment—Using variable-temperature STM, we investigated the initial formation and kinetics of the Ge/Si surface alloy. We observe the diffusion of the embedded Ge atoms at elevated temperature (>100°C). The diffusion events have the distinct character of defect-mediated diffusion. That is, rapid sequential diffusion of neighboring atoms separated by longer time intervals. We discovered that there are two defects responsible for embedded Ge atom diffusion: adsorbed dimers and adsorbed monomers.. Adsorbed dimers on this surface come in two flavors: pure Si-Si dimers and mixed Si-Ge dimers. In previous atom-tracking studies of pure and mixed dimer diffusion, we observed rare events in which mixed Ge-Si dimers exchange their Ge atom with a surface Si atom to become a pure Si-Si dimer. We also observed the reverse – a pure Si-Si dimer picking up an embedded Ge atom through an exchange event – leading to a mixed Ge-Si dimer. In the current work, we find that this process occurs much more frequently than previously thought leading to long-range diffusion and rearrangement of embedded Ge atoms in the surface alloy, as adsorbed dimers continually pick up and remotely deposit Ge atoms over the surface. Dimer-mediated Ge diffusion is shown in [Figure 1.]

Unlike dimers, adsorbed monomers on this surface are not imaged by STM at room temperature because they diffuse too fast. Nevertheless, there are configurations on the Ge/Si(001) surface in which a trapped monomer can be observed at the ends of adatom chains separated by a dimer row. Monomer diffusion is inferred by disappearance of the adatom at the end of one chain and the almost instantaneous appearance at the other. Exchange events between the diffusing monomer and alloyed Ge are detected as the monomer moves back and forth with an activation barrier of 0.8 eV.

Significance—Since the barrier for monomer diffusion (0.7 eV) is only slightly smaller than barrier to exchange into the surface, Ge-Si mixing will occur for any growth condition in which diffusion is operative. This is important because it makes atomically abrupt interfaces between Si and Ge, by Ge deposition alone, unlikely. Under growth conditions, in which there may be nonequilibrium concentrations of adsorbed monomers and dimers, the dominant process will depend on the populations of monomers and dimers, determined by kinetics, as well as thermodynamics.

Sponsors for various phases of this work include: DOE Office of Basic Energy Sciences and Laboratory Directed Research & Development

Contact: Brian S. Swartzentruber, Center for Integrated Nanotechnologies Science
Phone: (505) 844-6393, Fax: (505) 284-7778, E-mail: bsswart@sandia.gov

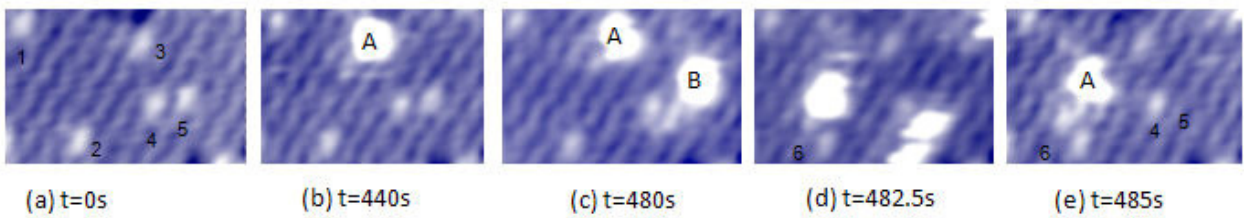

Figure 1. An image (4x8 nm^2) sequence showing the rearrangement of embedded Ge by mobile addimers on the dilute Ge-Si(100) surface at T=200°C. (a) The initial configuration of embedded Ge sites (numbered 1,2,3…). Ge does not move until addimers diffuse into the region. (b) After 440s (170 STM frames) an addimer labeled A is observed in the area. The image is deceptive: addimers are moving sufficiently fast that in most images, such as (d), the addimers appear as blurs because they hop several times during the STM image (c) At t=480s, a second addimer, B, arrives in the area. (d) A new Ge atom, 6, appears to have been exchanged into the surface, and dimer B passes over Ge site 5. A subsequent image (e) shows that the site 5 Ge atom is no longer present after the addimer B has passed, in addition, the new Ge atom at site 6 is now evident.

Determining the GaSb/GaAs-(2x8) Reconstruction and Its Impact on Stress Relaxation

by Jessica E. Bickel, Normand A. Modine, Joanna Mirecki Millunchick

Motivation—The critical film thickness of lattice-mismatched heterostructures, such as GaSb/GaAs, is limited to a few mono-layers before 3D islands form. This transition limits the types of devices, such as lasers, detectors, solar cells, and transistors that can be fabricated. Therefore, increasing this critical thickness has been the focus of much recent research. In this work, we focus on understanding the role of surface reconstructions in dislocation formation, because of their ability to relax the misfit stress at the interface and avoid 3-D island growth.

Accomplishment—The (2x8) reconstruction of GaSb/GaAs has been reported by the Huffaker group to be associated with nearly complete misfit strain relief through the formation of an array of misfit dislocations at the GaSb/GaAs interface. We examine three possible structures of the (2x8) reconstruction of GaSb for various strain conditions. The first structure was initially proposed for the InSb (2x8) reconstruction, and is referred to here as the α(2x8) (Fig. 1a). The second structure, the β(2x8), (Fig. 1b) is similar, except that it is built from the III-As β2(2x4) reconstruction that contains two Sb surface dimers (outlined in Fig. 1b) and exhibits a similar simulated STM image and line scan. The addition of an extra Sb surface dimer to the backbone results in wider rows along the [110] changing the line scan shape to a cycloid. The third structure was proposed by Laukkanen et al as a possible structure for the GaSb-(2x8) reconstruction. Because this structure also contains the β2(2x4) unit cell as a basis structure, we call it the β2(2x8) reconstruction. The β2(2x8) only has a single Sb dimer in the topmost surface layer, which requires the introduction of Sb atoms into anti-sites in the topmost cation layer to maintain charge neutrality. At the GaAs lattice parameter, our model demonstrated that the stable GaSb/GaAs-(2x8) reconstruction is the α(2x8) or β(2x8) depending on Sb chemical potential. The β(2x8) has a lower energy than the α(2x8) at the InP lattice parameter, but the α(2x8) decreases much more rapidly in energy as the lattice constant is reduced further to become stable at the GaAs lattice parameter. These results also show that the proposed β2(2x8) reconstruction is never stabilized, as it is always >25meV per unit area higher than the stable reconstruction at any Sb chemical potential. This higher energy is likely due to the Sb antisites in the structure. This also agrees with the experimental STM images (Fig. 2), which show no periodic change in intensity along the topmost dimer row as would be expected with an anion dimer every second position. Using this structural information, we were able to investigate the interaction between the α(2x8) and β(2x8) reconstructions and an array of misfit dislocations with an eight lattice constant spacing at the GaSb/GaAs interface. The trench associated with these reconstructions was observed to strongly concentrate the stress in the GaSb films in the underlying region resulting in a strong attraction between the dislocations and the trench. For thin layers, this suggests that the barrier for dislocation nucleation would be greatly reduced consistent with experiments.

Significance—In this work we use a combination of experimental and computational techniques to examine the structure of the (2x8) reconstruction of GaSb/GaAs as a function of strain. The resulting structures suggest a mechanism to increase the critical thickness for the islanding transition by providing a pathway for inducing an array of strain relieving misfit dislocations at the GaSb/GaAs interface.

Sponsors for various phases of this work include: DOE Office of Basic Energy Sciences and Laboratory Directed Research & Development

Contact: Normand Modine, Center for Integrated Nanotechnologies Science
Phone: (505) 844-8412, Fax: (505) 284-7778, E-mail: namodin@sandia.gov

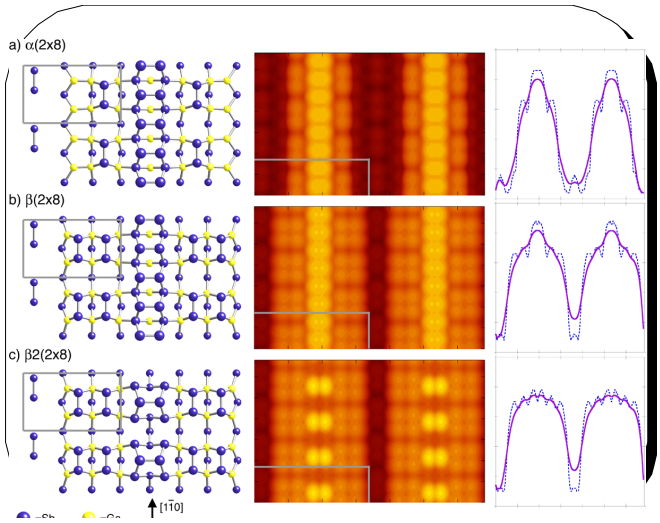

Figure 1. Proposed structures for the GaSb/GaAs-(2x8) reconstruction. (a) α(2x8), (b) β(2x8), and (c) β2(2x8). On the left are the atomic structures (Note: Some atoms removed for clarity). In the middle are simulated filled-state (negative bias) STM images. (ticks = 10Å). On the right are line scans of the simulated STM images with the original data (dotted line) and a smoothed line (solid line) calculated using a Steinman function and applying a geometric weighting of the nearest 10% of data points. (x-ticks = 10 Å, y-ticks = 1Å).

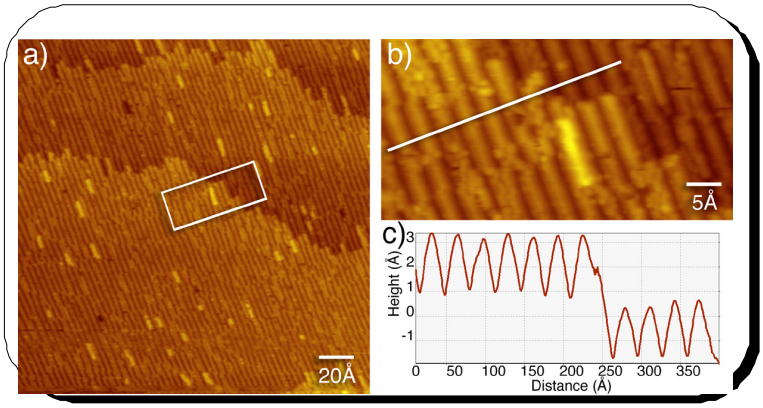

Figure 2. (a) STM image (V=-4.07V, I=100pA) of 2.0ML Sb/GaAs cooled under Sb flux to form the (2x8) reconstruction. (b) High resolution portion of the image in (a). (c) A line scan across the line indicated in (b).

In-Situ Structure and Property Correlation of Nanostructured Materials by Using a TEM-SPM Platform

by Jianyu Huang

Motivation—While excellent tools exist for the study of nanomaterials, such as scanning probe microscopies, high resolution TEM (HRTEM), near-field optical microscopy, etc., these tools generally lack the ability to correlate the measured properties with the material's structure, especially in real-time or under dynamic conditions. We are focused on developing research platforms and techniques that enable simultaneous structure-property correlation in nanoscale materials.

Accomplishment—1. *In-situ studies of batteries.* We are developing electrochemical cells inside a TEM with nanometer to atomic scale spatial resolution. We are also using the existing TEM-scanning probe microscopy (SPM) platform to study the battery process in real time and at an atomic scale. The research provides fundamental understanding of the science in batteries.

2. We are developing micro-electro-mechanical systems (MEMS) platforms that isolate individual nanowires/nanotubes and permit thermal property measurement while simultaneously presenting those materials inside a HRTEM for atomic-scale structural studies (see Figs. 1, 2).

3. *Cold-welding of ultrathin Au nanowires.* Collaborating with a CINT user from Rice University, we realized for the first time cold welding of individual Au, Ag,and Ni nanowires. We demonstrate that single-crystalline gold nanowires with diameters between 3 and 10 nanometers can be cold welded together within seconds by mechanical contact alone, and under relatively low applied pressures. In-situ measurements reveal that the welds are nearly perfect, with their electrical and mechanical properties approaching that of single crystalline nanowires, which is never achievable in macroscopic weldings. The high quality of the nano welds is attributed to the nanoscale sample dimensions, oriented attachment mechanisms and mechanically assisted fast surface atom diffusion. The welding of metals at the nanoscale is likely to play an important role in the bottom-up fabrication of electrical and mechanical nanodevices. The results will appear in **Nature Nanotechnology**.

4. *Discovered fractal sublimation of graphene and graphene bilayer edges* (see Fig. 3). The results are reported in **Proceeding of National Academy of Sciences** (Vol. 106, 10103 (2009)), and may provide important insight into the electronic application of graphene.

5. *Discovered for the first time superplastic deformation of salt and carbon nanotubes.* The results may guide the development of high toughness carbon nanotube composites for structural applications. These results are published in **Nano Letters** (Vol. 9, 2295 (2009)) and several **Physical Review Letters** (Vol. 97, 075501 (2006); 98, 185501 (2007); 100, 035503 (2008)) papers.

Significance—These studies provide unprecedented details regarding size, defects and surface effects on the electron, phonon, chemical, and mass transport processes in nanowires, nanotubes, and other nanomaterials (e.g. graphene), and to open a new path to study nanoscale transport phenomena in general. The results provide the fundamental science in tailoring the nanostructure fabrications for integrated device applications.

Sponsors for various phases of this work include: DOE Office of Basic Energy Sciences and Laboratory Directed Research & Development

Contact: Jianyu Huang, Center for Integrated Nanotechnologies Science
Phone: (505) 284-5963, Fax: (505) 284-7778, E-mail: jhuang@sandia.gov

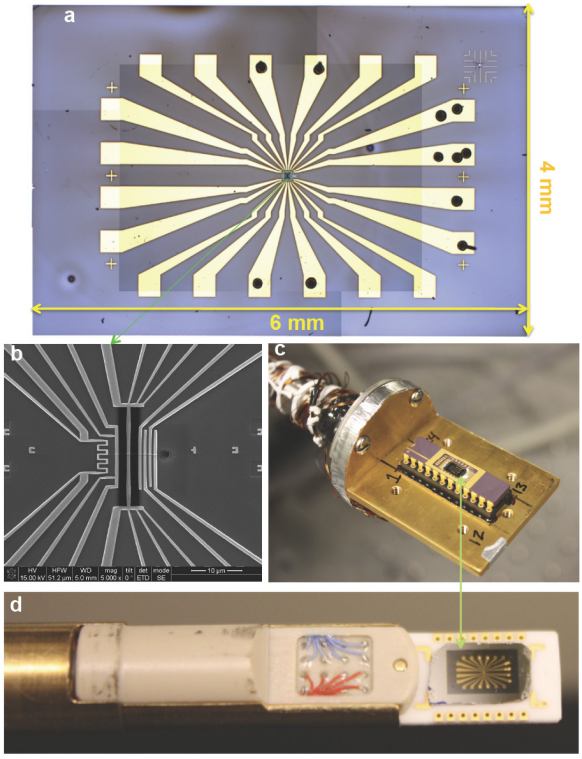

Figure 1. A MEMS device to enable both thermal/thermoelectric property measurements and TEM microstructure studies of nanomaterials.

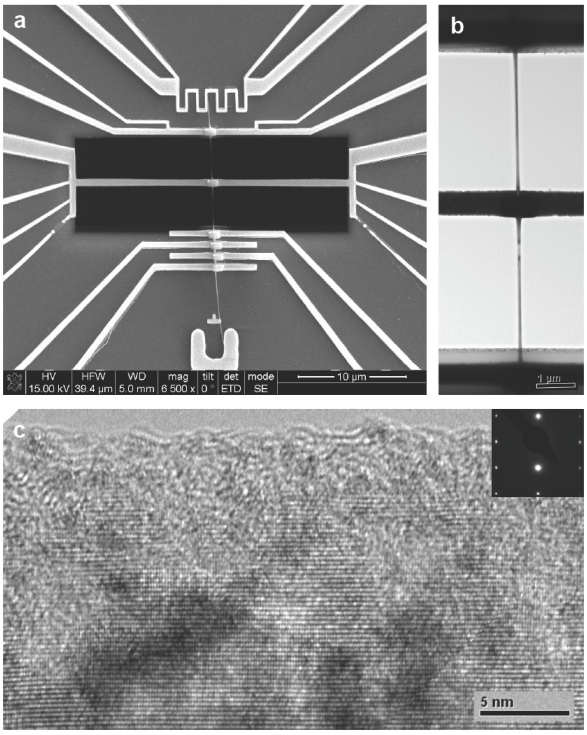

Figure 2. A GaN nanowire (NW) is mounted in a thermal microscopy platform. The atomic structure of the NW was determined.

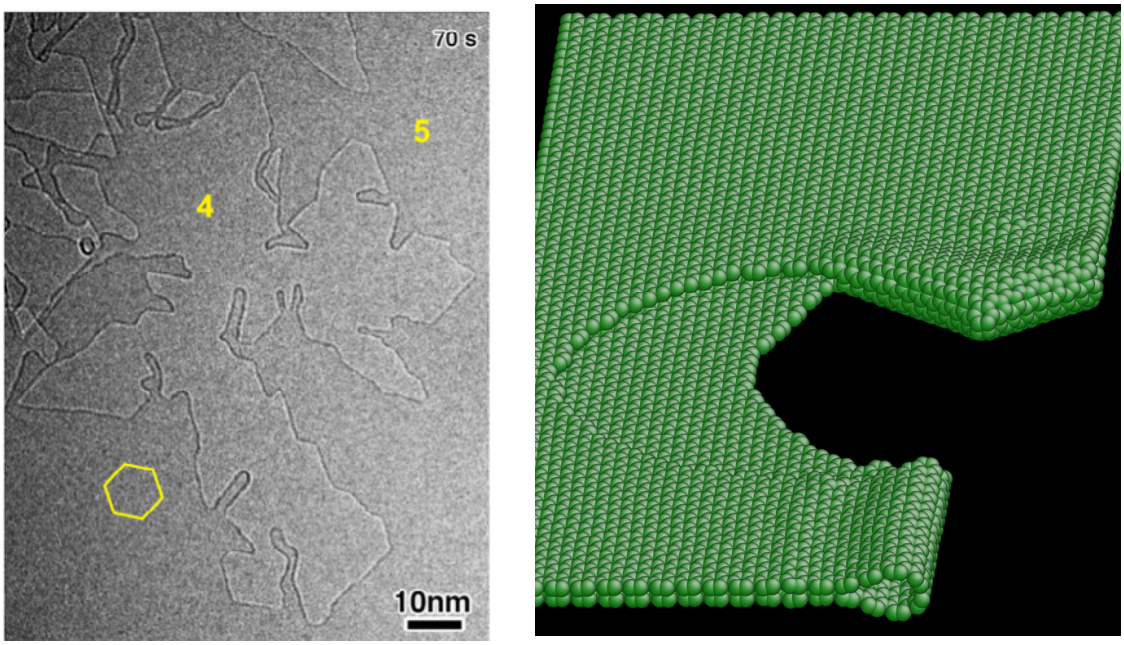

Figure 3. (Left) A snow-flake-like graphene sublimation pattern formed by in-situ Joule heating. (Right) The graphene edges formed by sublimation are bilayer edges rather than monolayer edges. The yellow hexagon marks the six sets of zig-zag planes, and the numbers mark the number of layers.

In-Situ Structures for Nanoscale Electrochemistry

by J. P. Sullivan, M. J. Shaw, A. Subramanian, and J. Huang

Motivation—Dramatic improvements in electrical energy storage are required in order to meet our nation's goals for energy efficiency and environmental management. Li-ion batteries offer great promise for achieving these goals, but there are issues with limited energy storage and long-term performance and reliability. To overcome these issues, we need fundamental understanding of electrochemical processes in real-time with atomic to nanoscale spatial resolution. In this work, we describe the development of novel *in-situ* platforms to probe battery electrochemistry at the nanoscale. These platforms are designed to isolate individual nanoparticle battery components and permit their characterization during electrochemical cycling inside a high resolution transmission electron microscope (HRTEM).

Accomplishment—We have developed a silicon micromachined platform to encapsulate Li-ion battery materials and electrolytes between a narrow gap created between two thin, electron transparent windows. The platform has been designed to enable – for the first time – HRTEM measurements of the structural and chemical changes that occur in Li-ion battery cathodes and anodes during charge and discharge cycling. Specifically, we will image the processes of lithium insertion and de-insertion in intercalation and conversion anode and cathode materials, such as graphitic anodes, represented as multi-wall carbon nanotubes, and oxide cathodes, represented as $Li_xMn_2O_4$ nanowires. In addition, we will image the chemical processes that result in loss of battery capacity with cycling, specifically the mechanism and morphology of solid electrolyte interphase (SEI) formation. The mechanisms of Li insertion and capacity loss during cycling represent some of the most important areas where deeper understanding is required in order to develop higher capacity and longer lifetime batteries.

A schematic of our *in-situ* platform is shown in Figure 1(a). The platform is created by bonding two chips using a flip-chip approach, with the bottom chip containing a dense array of buried electrical interconnects that permit electrical contact to battery materials. Figure 1(b) shows the bottom chip and a close-up of the electrical interconnect structure. The interconnect structure was designed to permit the assembly of nanoparticles and nanowires across a narrow electron-transparent aperture using the process of dielectrophoresis.

Dielectrophoresis (DEP) is a technique that enables the assembly of individual nanoparticles and nanowires spanning narrow electrode gaps by a process of applying AC electric fields in solutions containing suspended nanoparticles. We have designed special structures for DEP that permit the assembly of battery electrode materials on electron transparent membranes. Figure 2(a) shows a HRTEM image of a multi-wall CNT, and Figure 2(b) shows a scanning electron microscopy image of a MnO_2 nanowire assembled using DEP. These structures isolate battery-relevant nanoscale materials, enabling HRTEM studies of electrochemistry at the nanoscale.

Significance—Many research reviews have cited that the greatest need for battery research is to understand the mechanisms of energy storage and degradation with atomic-scale resolution during real-time electrochemical cycling. The platforms that we are developing will enable these studies for the first time. New understanding will enable the development of new materials and architectures with greatly improved performance compared to today's Li-ion storage cells.

Sponsors for various phases of this work include: Laboratory Directed Research & Development and DOE Office of Basic Energy Sciences

Contact: John P. Sullivan, Center for Integrated Nanotechnologies Science
Phone: (505) 845-9496, Fax: (505) 284-7778, E-mail: jpsulli@sandia.gov

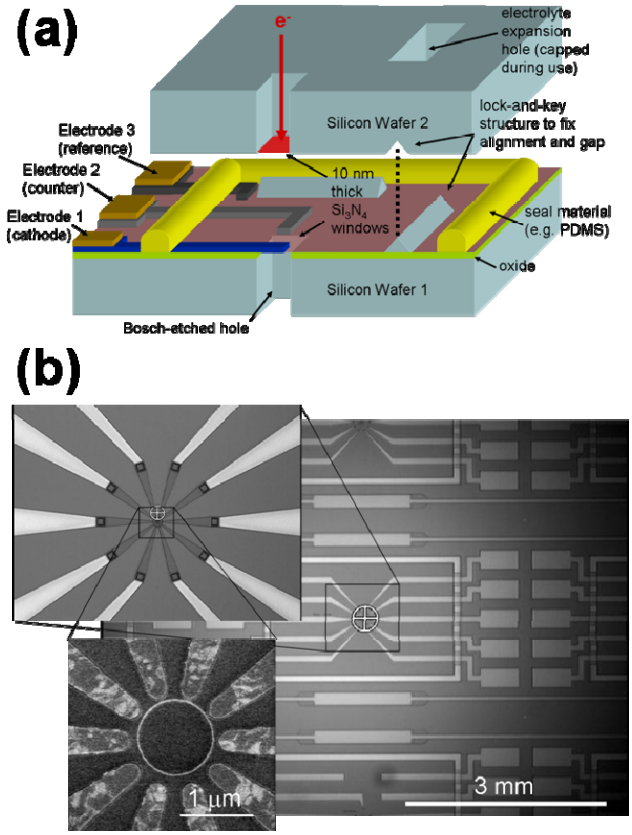

Figure 1. (a) A schematic of the *in-situ* electrochemistry platform for HRTEM studies of battery electrochemical processes. The platform is constructed using a flip-chip approach combing two MEMS chips that encapsulate a thin layer of electrolyte between electron-transparent windows. (b) Images of the lower chip of the platform showing the dense array of closely-spaced electrodes. This electrode geometry enables DEP of nanoscale battery materials.

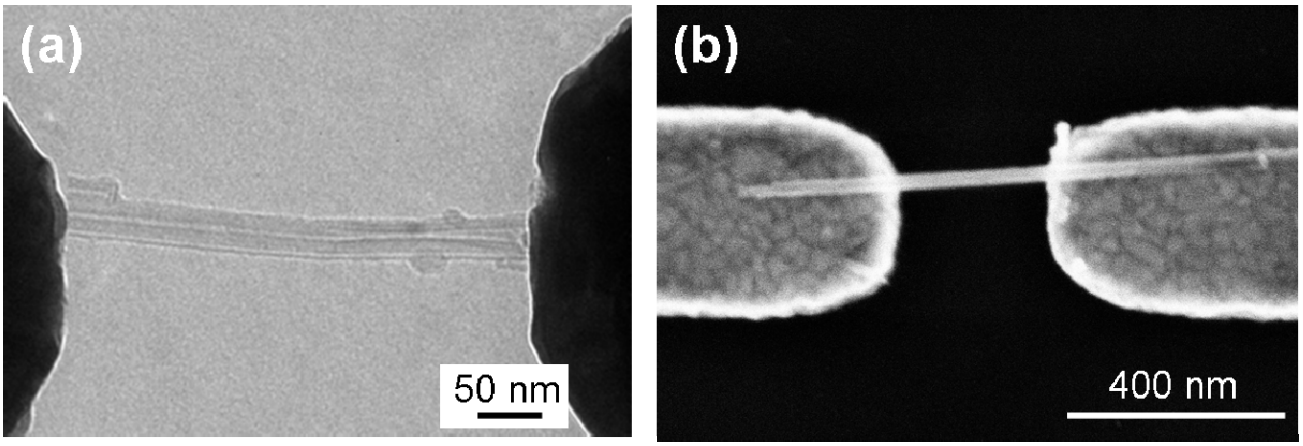

Figure 2. Examples of our work using DEP to assemble battery electrode materials. (a) A multi-wall carbon nanotube was assembled across a silicon nitride electron-transparent membrane using DEP. This image was taken using a HRTEM. (b) A scanning electron microscope image of a MnO_2 nanowire assembled using DEP. When reacted with Li, MnO_2 is a common Li-ion cathode material.

Nuclear Weapons Science and Technology

Evolution of Mechanical Properties during Aging of ErT_2 Target Films

by J. A. Knapp, J. F. Browning (ORNL), and G. M. Bond (NMT)

Motivation—The tritiated target films of neutron tubes are subject to aging problems because of the unavoidable decay of tritium into ^{3}He, forming bubbles which eventually limit the lifetime and performance of the tube. A detailed understanding of the effect of bubble growth on film properties was needed to help quantify tube reliability and margin to failure. We studied model ErT_2 films loaded with 100% tritium over a period of more than three years to measure the evolution of their properties as the He content grew through the entire range that production films might experience.

Accomplishment—The changing mechanical properties of the model films were monitored using ultra-low load nanoindentation, combined with finite-element modeling to separate the mechanical properties of the thin films from their substrates. The size of the growing ^{3}He bubbles was followed in parallel with transmission electron microscopy, while ion beam analysis was used to monitor total T and ^{3}He content.

The mechanical properties (yield strength, Young's modulus) of the films exhibited two behavior regimes, shown in Fig. 1: an initial period of increasing strength and approximately constant modulus followed by a period of decreasing modulus and slowly decreasing strength. The ^{3}He bubbles were observed in TEM micrographs to have a thin platelet morphology aligned with {111} planes in the matrix. Combining measurements of the platelet diameters with theoretical models of bubble growth, we deduced the density and thicknesses of the bubbles and showed that their growth also divided into two regimes which correspond to the observed changes in mechanical properties. First is an initial "Griffith-crack" nucleation and growth, where the ^{3}He forces apart {111} planes and forms the platelet-like bubbles. Once the bubbles are thick enough, they transition to a dislocation dipole mode, where circular dislocations form around each platelet, further increasing the thickness and lowering the pressure. The bubbles continue to grow in this mode until they overlap enough that the layer fractures.

A model of dispersion hardening was used to show that the increase in yield strength during the initial aging can be explained through binding of dislocations by the bubbles, resulting in strengthening much like that resulting from hard precipitates. As the bubbles transition to a dipole mode of growth, the lack of further strengthening is due to increasing bubble overlap combined with the large increase in available dislocations and a lowered pressure in the bubbles. The elastic behavior during aging was more difficult to model, but the general trend is the expected elastic softening due to the increasing fraction of ^{3}He in the material. The approximately constant Young's modulus during the initial aging may be partly due to the concurrent increase in yield strength. Some models predict a dependence on gas pressure in the bubbles which may be reflected in the data.

Significance—The new understanding of metal tritide film aging provided by this study is important as input to theoretical modeling of ^{3}He bubble growth and its effect on aging of neutron tube target films, helping to quantify margin to failure in present and future neutron tube designs. In particular, the previously unknown transition in properties at intermediate age may have unsuspected implications for film stability.

Sponsors for various phases of this work include: Nuclear Weapons Program Enhance & Surveillance Campaign, Readiness in Technical Base & Facilities (RTBF), and Neutron Tube Memorandum of Understanding

Contact: James A. Knapp, Radiation-Solid Interactions
Phone: (505) 844-2305, Fax: (505) 844-7775, E-mail: jaknapp@sandia.gov

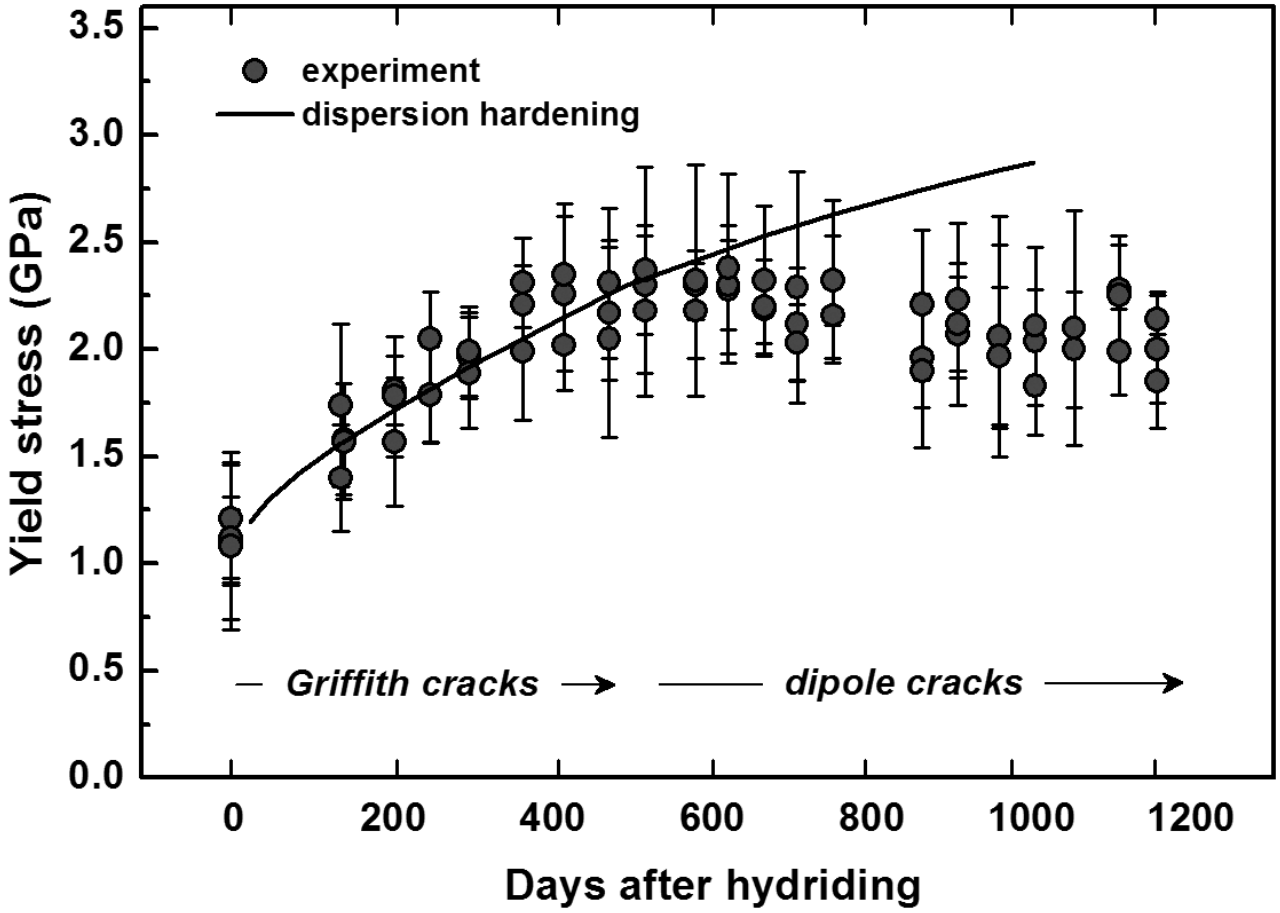

Figure 1. Yield strength of the tritiated films as a function of age, determined by nanoindentation. Two regimes are evident, associated with two different modes of bubble growth. The solid line is a prediction of strength from dispersion hardening theory.

Two-Dimensional Mapping of Electron Densities in an Ionized Plasma Using Laser-Collision Induced Fluorescence

by E. V. Barnat

Motivation—Sandia is developing a 3 D unstructured-mesh plasma code which will provide unprecedented capabilities for modeling plasma and charged-particle flows. This will greatly improve Sandia's computational capabilities for design and manufacturing of critical components that employ plasma for ion generation. In parallel with this code work, we are developing novel plasma diagnostic techniques and conducting experimental tests for code validation. The diagnostics and tests are designed to isolate key pieces of plasma physics that the code must be able to treat accurately for eventual success.

Accomplishment—A laser-based diagnostic technique that can quantify both electron densities and electron temperatures has been developed and implemented for mapping out the plasma plume generated by an arc undergoing initiation. The technique is known as laser-collision induced fluorescence (LCIF) and is illustrated in Figure 1a. A nanosecond laser is used to excite an atom from a lower lying state to a higher energy state. The excited state is either re-radiated to a lower energy states via spontaneous emission or redistributed to adjacent states via electron collisions. These redistributed states can then undergo radiative relaxation to lower energy states. It is this radiation which is termed LCIF, and it is this radiation, coupled with a predictive collisional-radiative model (CRM) that can be used to measure both electron density and electron temperature distribution of the plasma plume.

Central to the ability to use LCIF as a quantitative technique is the use of the CRM to predict the temporal evolution of the re-distribution of the excited state to nearby states during and after laser excitation. Such a prediction is illustrated in Figure 1b (red line) for the LCIF emitted from the 3^3D state in helium after excitation of the 3^3P state. For comparison, measured LCIF data (blue circles) is included in Figure 1b. The temporal shape and the intensity of the LCIF ultimately yield both electron temperature and electron densities. Simplifications to the LCIF technique can be realized by using temporally integrated LCIF as opposed to temporally resolved LCIF. Such integrated trends, expressed as ratios of LCIF from emitted from adjacent states to that emitted from the pumped state, are presented in Figure 1c. The resulting electron density dependent trends for the various transitions near the 3^3P state can then be used to construct two-dimensional maps of electron densities from measure data. Likewise trends in LCIF between higher energy states can be used to provide two-dimensional maps of the electron temperature.

In Figure 2, snap shots of an expanding plasma plume are presented. In the left hand column, LCIF from the pumped 3^3P state is presented and in the center column, LCIF from the adjacent 3^3D state is presented. Using the two data sets and the trends presented in Figure 1c, spatial maps of the electron densities are constructed and presented in the right column. At early times, little LCIF from the 3^3D state is observed because little plasma has been generated. As time progresses, the plasma becomes more dense and occupies greater volume. After 400 ns of operation, the plume reaches a steady state.

Significance—The development and implementation of the LCIF technique provides a unique tool for the quantification of both temporal evolution and spatial distribution of plasma generated by a vacuum arc ion source. This technique provides critical data to validate predictive simulations being developed at Sandia.

Sponsors for various phases of this work include: Nuclear Weapons Program

Contact: Ed Barnat; Lasers, Optics, and Remote Sensing
Phone: (505) 284-9828, Fax: (505) 844-5459, E-mail: evbarna@sandia.gov

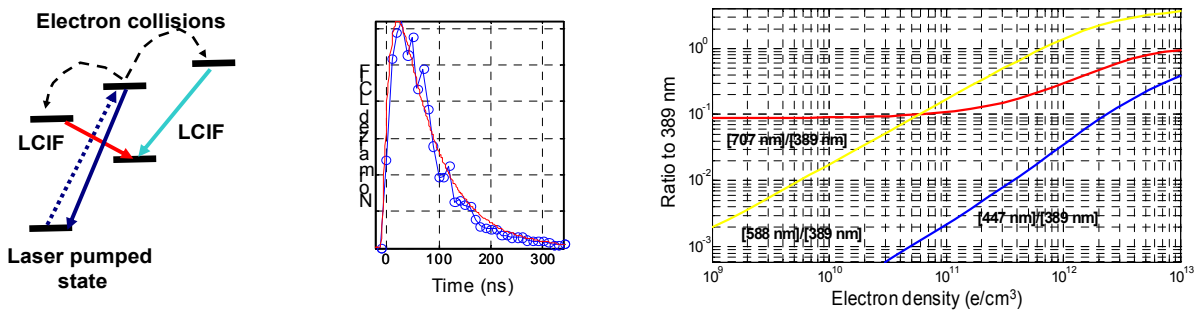

(a) (b) (c)

Figure 1. (a) Conceptual illustration of the LCIF technique, (b) time resolved demonstration of the LCIF technique and (c) time integrated trends utilized for the construction of two-dimensional map of electron densities.

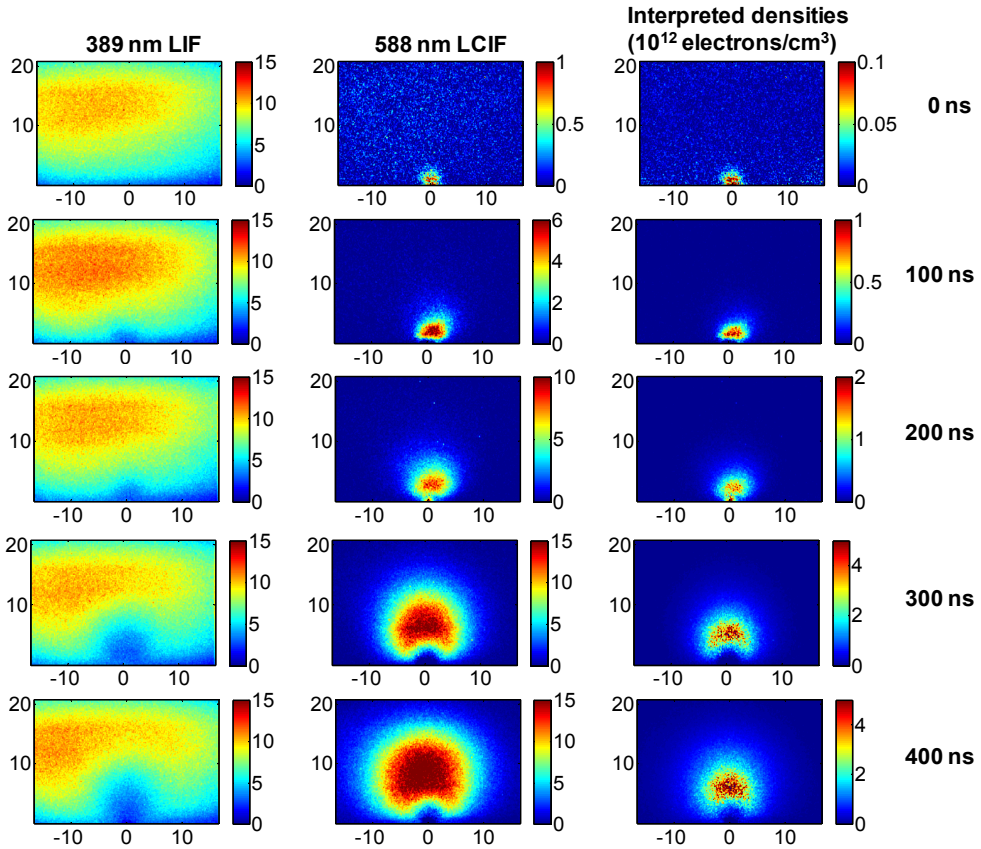

Figure 2. A series of images illustrating the temporal evolution of an expanding plasma plume generated by a vacuum arc. Two-dimensional images of LIF emitted from the 3^3P state at 389 nm (left column) and the LCIF emitted from the adjacent 3^3D state at 588 nm (center column) are used along with the trends presented in Figure 1(c) to yield two-dimensional maps of electron densities (right column).

Resolving Neutron Induced Defects in the Silicon Bipolar Transistor

by R. M. Fleming

Motivation—A number of issues complicate the accurate measurement of defects responsible for gain reduction in neutron irradiated silicon devices. These include the clustered nature of neutron displacement damage, the higher doping of the base, and an understanding of the types of defects in neutron damage cascades. A particularly difficult issue is that the deep level transient spectroscopy (DLTS) signatures of the important defects overlap making the relative contribution of the various defects difficult to assess.

Accomplishment—From earlier work on silicon point defects, it is well known that two deep levels in silicon, the vacancy phosphorous (VP) and the divacancy (V_2) contribute to gain reduction following irradiation. We showed earlier that an additional defect can be found within neutron damage cascades that is not present when the defects are uniformly distributed. We term this additional defect V_2^*. The structure of V_2^* is not known, and the name is chosen to reflect the fact that it has the same broad annealing characteristic seen using infrared absorption of V_2 after neutron irradiation. V_2^* may contain other primary defects, e.g. the interstitial, but it does not contain impurity atoms. It is the goal of this work to separate the overlapping DLTS signature of VP, V_2 and V_2^* in the transistor base into its constitutive components.

We accomplished this task by understanding the annealing characteristics of each of these defects at annealing temperature above room temperature. The annealing characteristics of V_2^* were obtained from our own measurements in the transistor collector where little VP is present. The annealing characteristics of VP were taken from the literature where it is shown that VP anneals faster in the zero charge state and from our own measurements of transistor irradiated with non-end of range (EOR) 36 MeV silicon ions where less V_2^* is present. Based on the literature and our own measurements, we assume that the single acceptor level of the isolated V_2 defects does not anneal over the temperature region of interest.

We constructed polynomial functions that give the proper shape of the annealing functions and we fit the amplitude of these functions to measured DLTS spectra as a function of annealing temperature and junction bias. The results for neutron irradiation in the Sandia Pulsed Reactor (SPR) are shown in Fig. 1 where the black squares represent the DLTS spectrum before annealing and the red triangles are the spectrum after annealing at 530 K. VP_2 grows as the annealing temperature is raised because VP becomes mobile and moves to a P^+ donor. V_2 (=/-) decreases because V_2 becomes mobile above 500 K and it may also move to a P^+ donor. Our analysis shows that the deep defects responsible for gain reduction after neutrons consist of about 42% VP and equal parts of V_2^* and V_2 (29% each). DLTS spectra of 36 MeV Si ion damaged transistors, which have fewer damage cascades and less V_2^*, are shown in Fig. 2. A similar analysis shows a larger VP and a smaller V_2^* component in this case as expected.

Significance—The separation of the DLTS spectrum into its constitutive components is the first step toward measuring the relative effectiveness of each of these defects in reducing gain. We are currently in the process of correlating these data with similar annealing measurements of transistor gain.

Sponsors for various phases of this work include: Nuclear Weapons Program Nuclear Survivability Campaign

Contact: Robert M. Fleming, Semiconductor Materials and Device Sciences
Phone: (505) 284-8460, Fax: (505) 844-1197, E-mail: rmflemi@sandia.gov

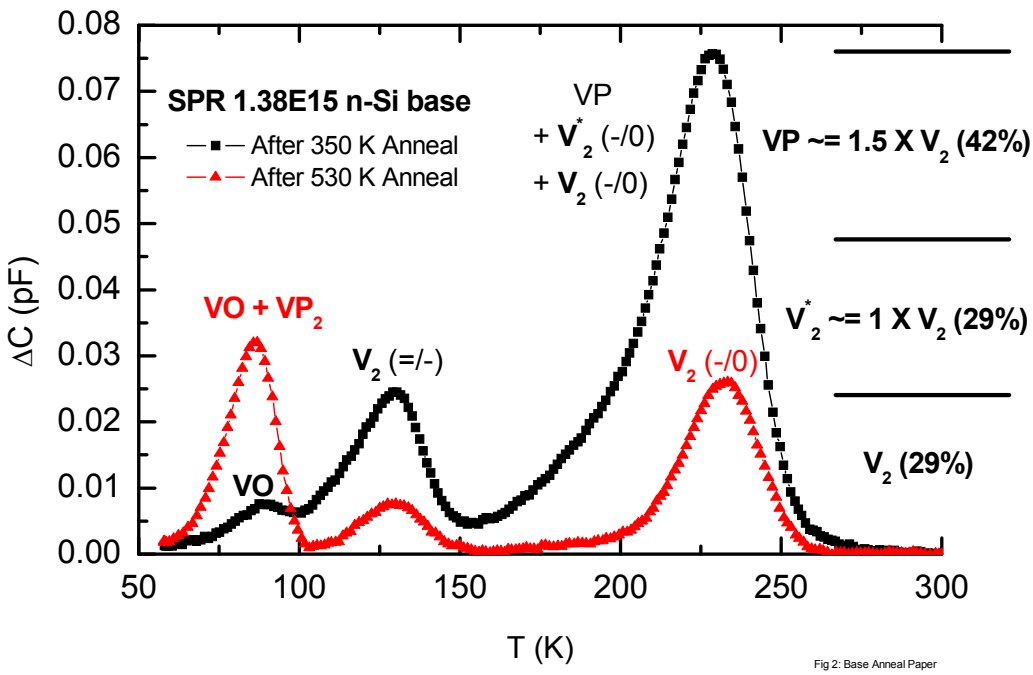

Figure 1. DLTS of the n-type base after annealing a neutron-damaged pnp to 350 and 530 K. Analysis of the deep DLTS peak at about 230 K reveals that it is composed of about 42 % VP and equal parts of V_2^* and V_2.

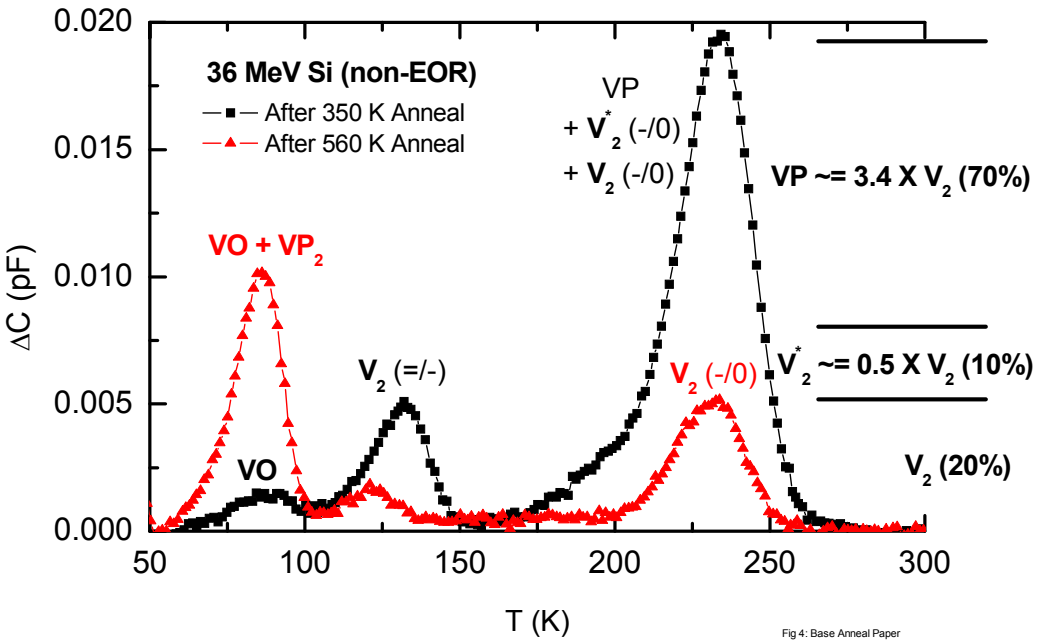

Figure 2. DLTS of the n-type base after annealing a pnp transistor damaged with 36 MeV Si ions to 350 and 530 K. Damage with ions of this energy are expected to produce less clustering and less V_2^*. Here, analysis of the deep DLTS peak at about 230 K reveals that it is composed of about 70 % VP.

Semiconductor Q-switch Demonstrated in Solid-State Microlaser

by Jeff Cederberg, Daniel Bender, Michael Pack, Randy Schmitt

Motivation—Timing control is critical for solid-state microlasers. In a microlaser, the saturable absorber holds off laser oscillation until the field is high enough that the circulating photons can saturate the optical transition, rendering the absorber partially transparent. Existing lasers use doped insulators that either saturate at a low fluence or require high voltages. Semiconductor saturable absorbers (SESA) based on multiple-quantum-well (MQW) structures can be used as Q-switches and present the opportunity for improved pulse control. Developing such MQW structures, evaluating their optical characteristics, and demonstrating their suitability were necessary to evaluate if semiconductors saturable absorbers are suitable for this application.

Accomplishment—We developed epitaxial growth on InP substrates of MQW SESAs based on AlGaInAs quaternary materials. AlInAs serves as the barrier material with thickness corresponding the half the mode spacing in the material. The composition and thickness of the AlGaInAs well was set to produce a ground state transition at 1064 nm. We have optimized our epitaxy to achieve the growth of a SESA with 30 two-MQW periods, over 6 µm in total thickness.

We have optical characterization of the MQW saturable absorber focused on quantifing the absorbance bleaching lifetime, the modulation depth, and the unsaturable loss. Fig. 1b shows the transmission decay observed with a transient pump-probe measurement. A single exponential decay is observed with a lifetime exceeding 100 nsec. The modulation depth of the transmission was measured with a similar technique by monitoring the pump power incident on the sample. The transmission was increased by 8% for the sample shown in Figure 1a. The unsaturable loss was as high as 50% in the sample shown, but was reduced to 20% by using compensated substrates.

The SESA was tested as a passive Q-switch in a microlaser cavity (Fig.2). Pump light emitted from the fiber is imaged onto the gain medium, which is AR-coated at 808 nm and HR-coated at 1064 nm on one surface and AR-coated at 1064 nm on the second surface. The AR-coated MQW SESA, located approximately in the middle of the cavity, allows lasing modes to align with the QWs. Our SESA microlasers feature high efficiency (25%), single-mode operation, Gaussian beam profiles and repetition rates exceeding 1 MHz.

Significance—Through this demonstration, we have established that semiconductor heterostructures can withstand the high optical fluences produced in microlaser cavities. The use of semiconductors as saturable absorbers opens new possibilities for improving the timing control and jitter in Q-switched microlasers. The demonstration of long absorbance bleaching lifetimes suggests AlGaInAs heterostructures possess a high carrier lifetime, a critical requirement for optoelectronic devices.

Sponsors for various phases of this work include: Nuclear Weapons Program

Contact: Jeff Cederberg, Advanced Materials Sciences
Phone: (505) 284-5456, Fax: (505) 844-3211, E-mail: jgceder@sandia.gov

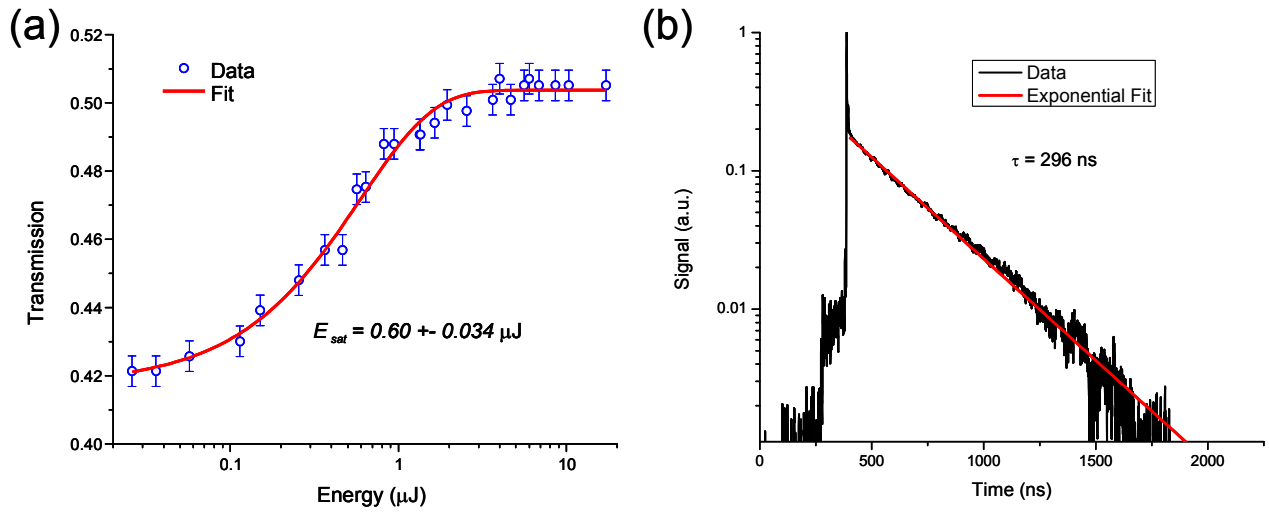

Figure 1. (a) Energy dependent transmission (blue dots) for a SESA containing 40 QWs. Exponential fit (red line) depicts a 600 nJ saturation energy (76 μJ/cm^2 saturation fluence). (b) Transmission decay after bleaching (black line) and exponential fit (red line) for a 60 QW sample. The fit gives bleaching lifetime of 296 ns.

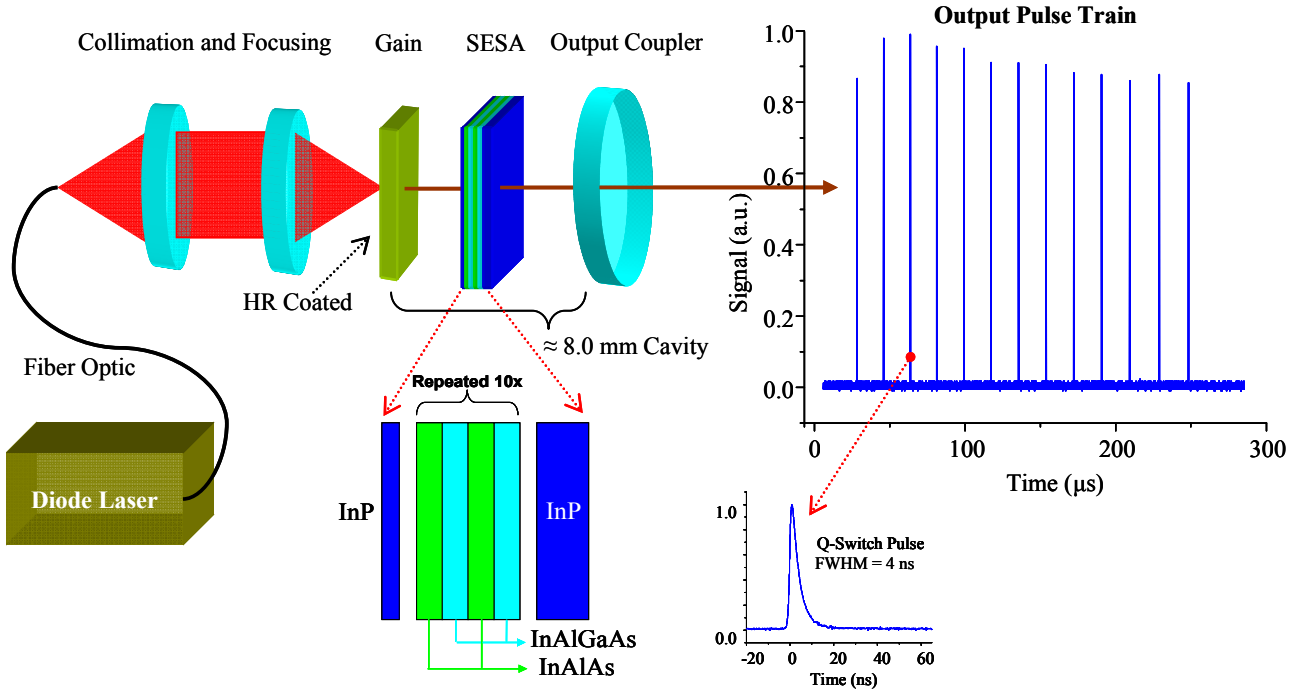

Figure 2. Complete SESA-based microlaser system with only three cavity elements. Expanded view of SESA shows QW structure. Depiction at right shows the output pulse train and a blow-up of a single pulse showing the pulse width.

A New Capability for Using Orbital-Dependent Functionals in Density-Functional-Theory Calculations

by A. F. Wright, N. A. Modine, D. M. Day, L. Romero, and M. P. Desjarlais

Motivation—Density-functional theory (DFT) is widely used at Sandia to obtain information about materials under extreme conditions and defects in semiconductors. The accuracy of this information depends on the *functional* used to describe quantum mechanical interactions between electrons. All functionals currently in use approximate these interactions and, in addition, all but the type noted below depend explicitly on the total electron density. As a result of this density-dependence, each electron incorrectly interacts with itself, yielding non-negligible errors in DFT results. These self-interactions can be eliminated by defining the functional to be the Fock expression, which correctly describes electron exchange inter-actions. However, the Fock expression is challenging to evaluate since it depends on single-electron orbitals. Before the development of the iterative technique described below, finding DFT solutions for the Fock expression was so computationally demanding that less than 10 atoms could be treated when using the plane wave basis sets and periodic boundary conditions preferred by physicists.

Accomplishment—We have developed a new iterative technique for obtaining DFT solutions when using orbital-dependent functionals such as the Fock expression, and have implemented this technique in Sandia's Socorro code. This technique allows calculations to be performed for hundreds of atoms and thus is a significant improvement over prior techniques. Moreover, this technique can also be applied to density-dependent orbitals, thereby making it possible to use *hybrid* (combined density- and orbital-dependent) functionals, which have yielded highly accurate results in quantum chemistry studies.

In developing this new technique, we addressed a difficult technical issue related to the use of periodic boundary conditions: When using the Fock expression, an integral divergence arises in the energy due to the long range of electrostatic interactions. We discovered that this divergence has significant, detrimental consequences for the convergence rate of the energy with respect to numerical sampling: When the divergent term is ignored, the convergence rate is 1/N where N is the number of sampling points (Fig. 1). This is much slower than the exponential convergence found using density-dependent functionals. Our analysis and tests showed that $1/N^2$ convergence can be achieved by using an analytic continuation technique and exponential convergence can be achieved by utilizing an attenuated Coulomb kernel to restrict the range of the electrostatic interactions. Although calculations using the Fock expression and our new iterative technique are significantly faster than prior calculations, they are still roughly an order of magnitude slower than DFT calculations using density-dependent functionals. Compute times using the Fock expression are dominated by double-precision fast-Fourier transforms (FFT). Substantial reductions in these times may be possible in future computers via the use of threaded processes and/or dedicated FFT co-processors.

Significance—To the best of our knowledge, the new capability described herein is available nowhere else in the world. When used with the Fock expression, this capability eliminates self-interaction errors and also yields semiconductor band gaps in good agreement with measured values (Fig. 2). More importantly, this new capability allows hybrid functionals to be seamlessly used in calculations with a plane wave basis. This opens the possibility of obtaining significantly higher accuracy in results for solids and plasmas, akin to what has been found by the quantum chemistry community.

Sponsors for various phases of this work include: Laboratory Directed Research & Development and Nuclear Weapons Program Dynamic Materials Campaign

Contact: Alan F. Wright, Nanomaterials Sciences
Phone: (505) 845-0445, Fax: (505) 844-5470, E-mail: afwrigh@sandia.gov

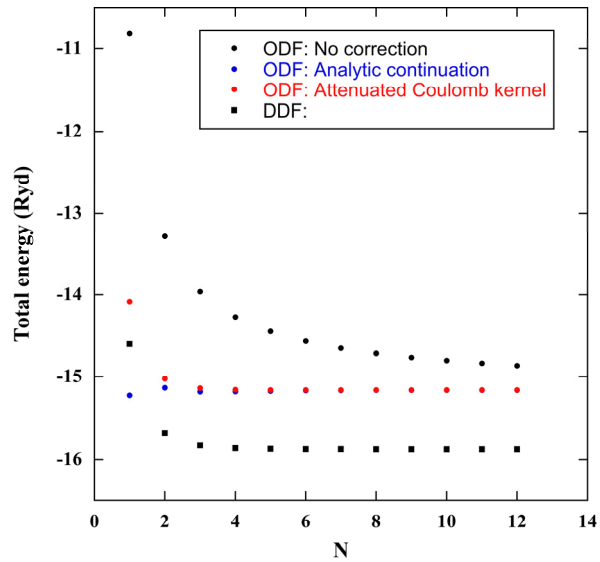

Figure 1. Convergence of the silicon total energy versus the number of sampling points (N) using: an orbital-dependent functional (ODF) with no correction for the integral divergence, analytic-continuation correction, attenuated Coulomb kernel correction; and a density-dependent functional (DDF).

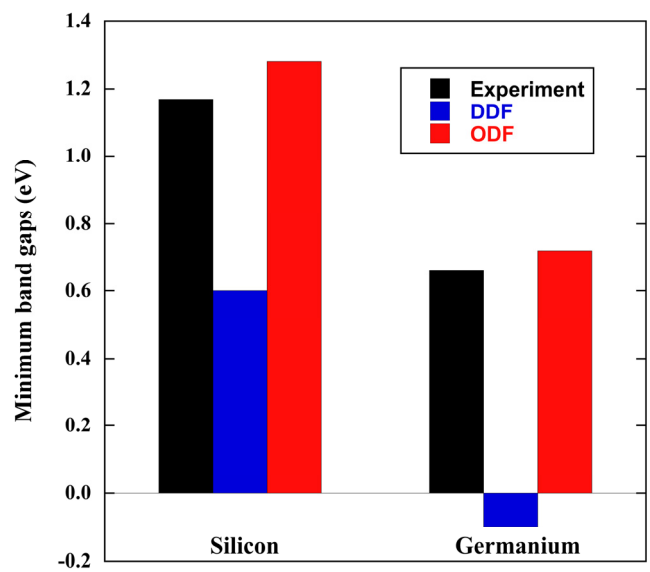

Figure 2. Measured and computed minimum energy gaps for silicon and germanium: Density-Dependent Functional (DDF) and Orbital-Dependent Functional (ODF).

Evolution of Oxide Stability During Localized Corrosion of Model Al-Cu Alloys

by N. Missert, R. G. Copeland, P. Kotula, J. J. Hren, and J. Rivera

Motivation—Al-Cu alloys are important for the aerospace, automobile, and micro-electronics industries. Although localized corrosion of aluminum-copper alloys in halide electrolytes is known to occur in the vicinity of intermetallic Cu-rich particles, a detailed understanding of the evolution of attack, from the mechanisms responsible for breakdown, to the transition to stable pitting, is still lacking. Since corrosion is a redox reaction, where the anodic oxidation of the metal must be balanced by the cathodic reduction of oxygen from solution, the mechanisms governing both processes must be understood in order to provide a complete picture. High cathodic reaction rates can generate local alkalinity, altering the properties of the passive oxide layer. Understanding the stability and charge transfer properties of the passive film in alkaline environments is therefore critical.

Accomplishment—We have used electron beam co-evaporated Al-3.5%Cu thin films as a model system for studying the effects of alkaline exposures on the loss of passivity in Al-Cu alloys. After annealing, Al_2Cu intermetallic particles form at grain boundaries in an Al-0.5%Cu matrix, with nanometer scale surface roughness as measured by AFM. In-situ fluorescence microscopy shows that initially, high cathodic reaction rates (which significantly raise the pH) occur locally on the electrode surface in response to remote anodic attack. The area available for high cathodic reaction rates continues to expand with time of exposure to the high pH solution, suggesting that exposure to the high pH environment enables more facile electron transfer to support high oxygen reduction reaction rates.

Areas exposed to the high pH environment (Figure 1) show localized attack adjacent to some particles, at grain boundaries and on grain faces, where an increase in attack site density is directly correlated to exposure time. Ex-situ AFM imaging shows no evidence for de-alloying of the particles or matrix even after a 30 minute exposure to pH 11.5, suggesting that on time scales important for corrosion initiation, an understanding of the evolution of oxide electronic conductivity as a function of pH is required. In order to evaluate the conductivity of the passive films, the current-voltage characteristics near the open circuit potential (OCP) were measured as a function of pH. The open circuit potential dropped as the pH increased, consistent with an increase in corrosion rate; that is an increase in both passive film oxidation rate and the balancing oxygen reduction rate. The slope of the cathodic branch, measured near the OCP, gives the polarization resistance, which decreased by over four orders of magnitude, as the pH increased from 6 to 11.5, demonstrating a huge activation of the surface for both the anodic and cathodic reactions. Electrochemical impedance spectroscopy (Figure 2) also showed a dramatic drop in the oxide impedance as the pH increased. The specific mechanism responsible for this activation is postulated to be a thinning of the surface oxide or an increased electronic conductivity, since Cu surface enrichment was ruled out through x-ray absorption, ToF-SIMS imaging, and cross-sectional TEM/EDS.

Significance—These studies show that the charge transfer properties of the passive oxide on Al-Cu alloys are sensitively dependent upon the solution pH. In alkaline environments, the charge transfer rates can increase by several orders of magnitude. These results will be used to develop accurate, predictive models for component lifetime and reliability limitations due to localized corrosion.

Sponsors for various phases of this work include: DOE Office of Basic Energy Sciences and Nuclear Weapons Program

Contact: Nancy Missert, Nanomaterials Sciences
Phone: (505) 844-2234, Fax: (505) 844-1197, E-mail: namisse@sandia.gov

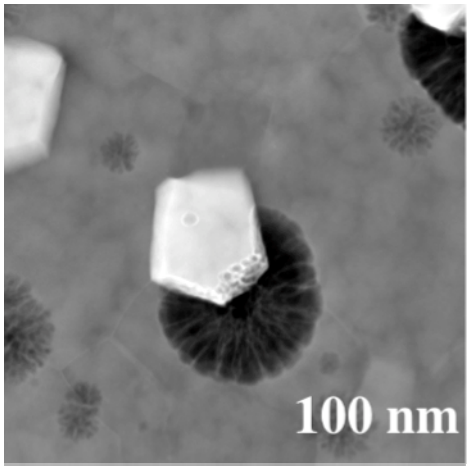

Figure 1. Early stages of localized attack on cathodic regions of the electrode occur on the grain faces, at grain boundaries, and at the interface between Al_2Cu intermetallic particles and the surrounding matrix.

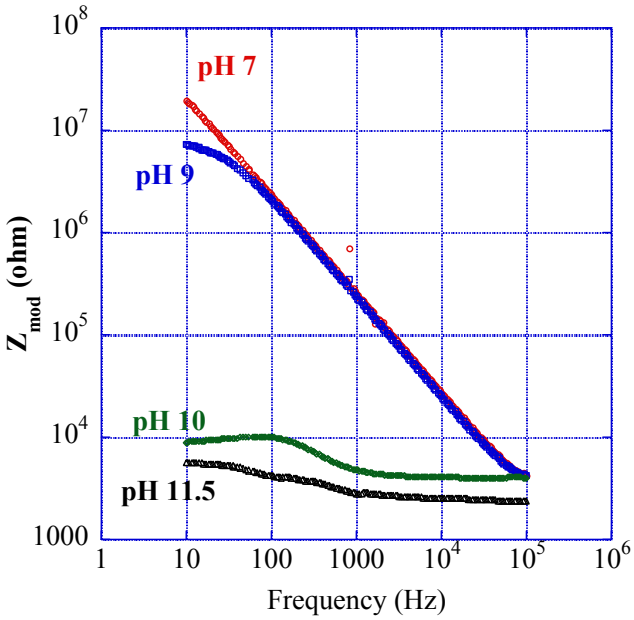

Figure 2. Electrochemical impedance spectroscopy showing several order of magnitude decrease in impedance with increasing alkalinity.

Science and Technology for National Missions

Monolithically Integrated Solid-State Terahertz Transceivers

by M. C. Wanke, E. W. Young, C. D. Nordquist, M. J. Cich, A. D. Grine, C. T. Fuller, J. L. Reno. and Mark Lee

Motivation—The "unconventional" terahertz (THz) frequency electromagnetic spectrum offers disruptive advantages for security, defense, scientific, and industrial missions. However, THz solid-state technology remains immature compared to microwave electronics and infrared photonics. A central component of THz technology, a heterodyne transceiver, has until now relied on large, high-maintenance gas- or vacuum-tube sources to supply coherent THz radiation of sufficient power and mechanically aligned optical coupling to deliver power to a THz receiver. Clearly any widely practical THz system requires an integrated semiconductor-based technology. Only recently has this become realistic with the invention of high-power microelectronic THz quantum cascade lasers (QCLs). This project's goal was to integrate a QCL and diode mixer onto a single chip. The result is the first true THz integrated circuit (IC) that performs all the functions of existing THz transceivers but at a small fraction of the size and in a robust platform scalable to semiconductor fabrication production.

Accomplishment—The starting point for this integrated transceiver exploits a structural advantage unique to QCLs. In a THz QCL, at least one of the metal contacts is nearly in direct contact with the optically active region and hence has large overlap with the optical mode. Our transceiver capitalizes on this overlap to literally embed a small Schottky diode mixer into the ridge waveguide cavity of a QCL, as depicted in Fig. 1. Here the semiconductor cathode of the Schottky diode and the top bias contact of the QCL ridge waveguide share the same *n*+ doped GaAs layer. The QCL top (ground) contact is made using an ohmic metal while the diode is made using a Schottky metal. This integration strategy takes advantage of the fact that the QCL ridge waveguide cavity's *internal* electric field is strongest near the metal-semiconductor interface and thus permeates the diode's cathode. The internal field modulates the width of the diode's depletion region, leading to mixing of the THz signals. An image of a completed transceiver is shown in Fig. 2. After processing, the lasing characteristics of the QCL showed no significant degradation in power or threshold bias conditions, thus confirming operation as a coherent transmitter. Operation of the THz IC as a heterodyne receiver was also explicitly demonstrated. An external signal was supplied by a molecular gas laser, using the 2.841143 THz line of difluoromethane. Heterodyne reception of the external signal was clearly observed at the output of the Schottky diode, which generated down-converted microwave signals at difference frequencies between several of the QCL's internal Fabry-Perot (F-P) modes and the external molecular gas line. The F-P difference frequency generated by the diode was also be used as an active feedback signal to phase lock the difference modes of the QCL to a microwave reference and hence maintain constant mode spacing to high precision. The THz IC significantly simplifies the ability to phase lock by eliminating optical coupling between physically separate components.

Significance—Widespread use of the THz spectrum outside the laboratory has awaited a viable solid-state technology platform. The monolithically integrated solid-state THz transceiver developed here represents a broadly applicable answer to this technological challenge in the form of the first working THz IC. Such a transceiver IC is the initial step towards higher stages of chip-level integration of multiple THz functionalities in a miniature, reliable, and scalable platform.

Sponsors for various phases of this work include: Laboratory Directed Research & Development

Contact: Mark Lee, Semiconductor Materials and Device Sciences
Phone: (505) 844-5462, Fax: (505) 844-4045, E-mail: mlee1@sandia.gov

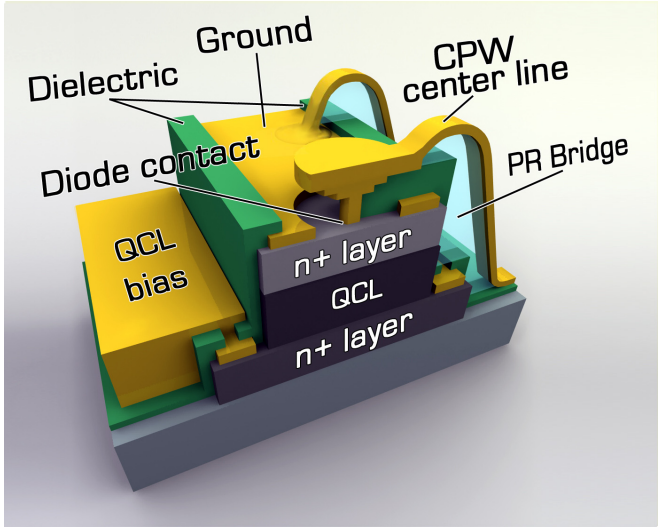

Figure 1. Design drawing showing the Schottky diode position atop a QCL ridge waveguide and ground-signal-ground co-planar waveguide (CPW) contacts to the diode mixer. Some of the insulating layer under the diode (green) and the photoresist (PR) bridge (light blue) have been cut-away for clarity.

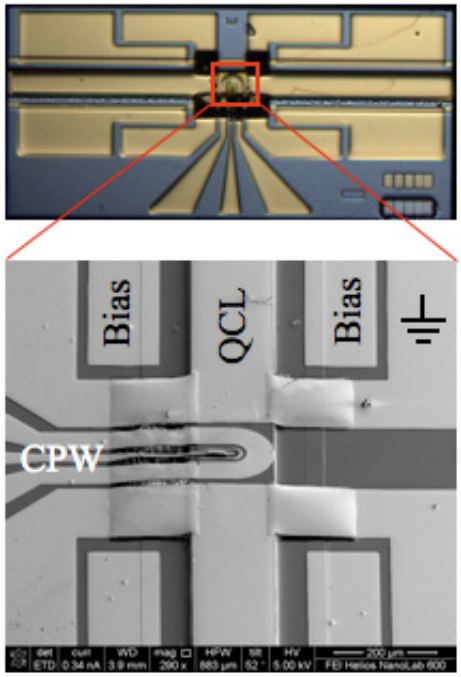

Figure 2. (top) Optical microscope plan view image of a complete THz transceiver IC with all electrical contacts, and (bottom) expanded focused ion-beam image showing the CPW contact configuration to the Schottky diode anode.

Longwave Infrared Optical Cross Sections for Biological Warfare Agents and Simulants

by R. L. Schmitt, S. M. Sickafoose, M. S. Johnson, M. V. Pack, J. W. Porter, C. F. Briner, and D. Castillo

Motivation—LIDAR (Light Detection and Ranging) systems are now a key component in the DoD strategy to protect troops from biological weapons on the battlefield. These standoff detection systems can only be tested against aerosol clouds of simulants, not against the real threat agents. In order to evaluate system performance against threat agents, we project the performance using field test data collected on simulant clouds using the lidar equation and knowledge of the optical cross section values for the simulants and threat agents. For several years, we have been measuring the optical backscatter and laser induced fluorescence cross sections of biological simulants and threat agents for a DoD customer. Recently, we have added measurement capability in the 9.3 to 10.7 µm region, a key wavelength region for a bio standoff system now under consideration.

Accomplishment—We modified the Sandia B70 LIDAR trailer, adding a tunable pulsed CO_2 laser that was programmed to tune over 19 discrete CO_2 lines in the 9.3 to 10.7 µm region. One of the major challenges in making the longwave infrared (LWIR) cross section measurements was measuring cross sections at Nd:YAG wavelengths at the same time. This required designing a beam combiner for the out-going lasers that was able to transmit (coaxially) 355 nm, 1064 nm, and 9.2-10.7 µm laser radiation and a receiving wavelength separator to send the returning signals to the wavelength appropriate detectors. To combine the outgoing laser beams we used an optical-grade Si wafer to transmit the CO_2 laser beam while reflecting the other wavelengths. On the receiver, we were able to use a custom dielectric coating to separate the LWIR return from the other wavelengths. In order to incorporate control of the new laser and detectors and streamline the data acquisition process, the entire software control program was re-written.

To measure agent cross sections, we first collect standoff lidar data for aerosol clouds of simulants released in a controlled outdoor facility. After calibration of our lidar system, we calculate the optical cross sections of these simulant aerosols. Next, we measure the optical response at all of the wavelengths of the simulant materials and threat agents contained in specially designed cuvettes. Finally, we compute the agent cross sections by comparing their optical signals relative to simulants using knowledge of the cross sections of the simulants.

To enable in-trailer LWIR measurements, we designed and built new stainless steel cuvettes with a ZnSe window on one side for LWIR optical access and a fused silica window on the other side for UV – NIR optical access.

A key capability of the B70 LIDAR trailer is its capability of propagating laser radiation for stand-off measurements and, after minimal reconfiguration, performing in-trailer measurements on the same materials contained in sample cuvettes, with the same laser sources and detectors.

Significance—The elastic backscatter optical cross sections of 24 biological simulants and 8 agents at 21 separate wavelengths and the fluorescence cross section at 355 nm will be computed from the data by early 2010. These values, delivered to the DoD customer, will allow the Joint Biological Standoff Detection Systems program to evaluate performance of standoff systems.

Sponsors for various phases of this work include: DOD Joint Biological Standoff Detection Systems Program

Contact: Shane Sickafoose, Lasers, Optics, and Remote Sensing
Phone: (505) 845-8362, Fax: (505) 844-5459, E-mail: smsicka@sandia.gov

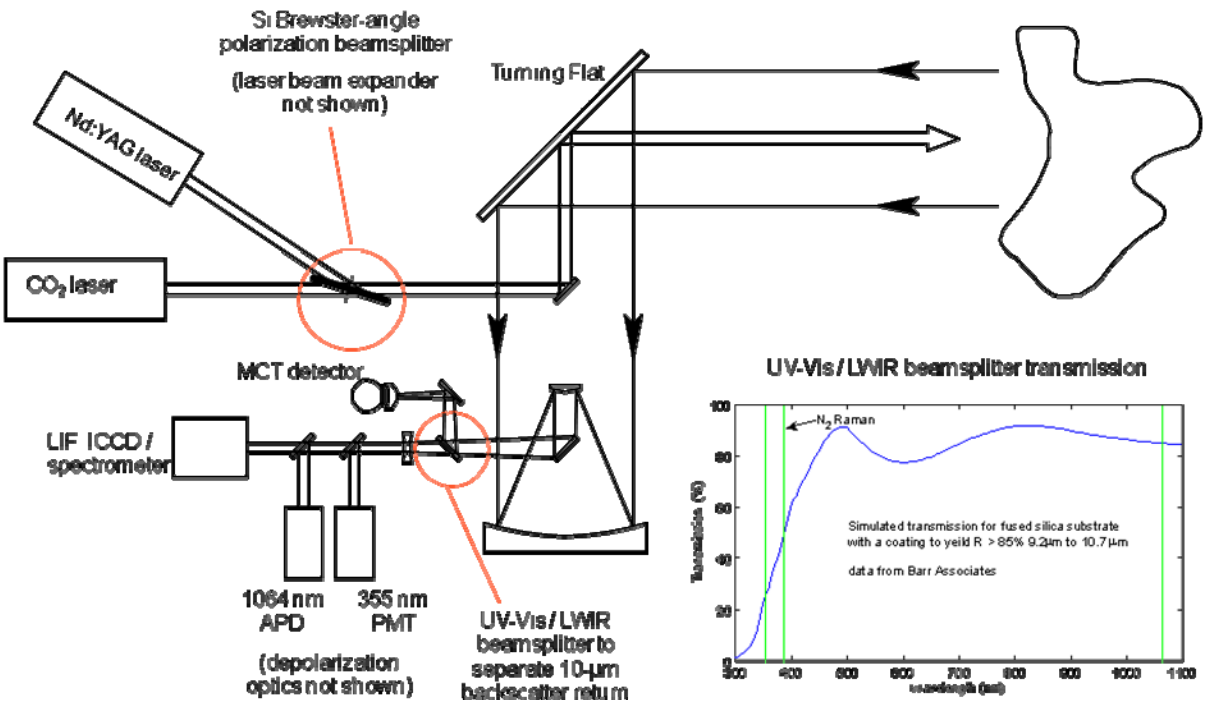

Figure 1. Schematic diagram of the new multi-wavelength range-resolved setup in B70.

Figure 2. Specially designed stainless steel cuvette with ZnSe window for 9 – 11 um use and fused silica window for UV – NIR use

Nanoporous-Carbon Coated SAWs for ppb Detection of Trihalomethanes in Water

by M. P. Siegal, C. D. Mowry, K. B. Pfeifer, and A. L. Robinson

Motivation—The treatment of water results in many disinfection products; trihalomethanes (THMs) are among the most common and of greatest concern to regulatory bodies and the public due to their known adverse health effects, which include cancer and miscarriage. The Environmental Protection Agency (EPA) regulatory limit for THMs (chloroform, bromodichloromethane, dibromochloromethane, and bromoform) is 80 parts-per-billion (ppb). Current detection methods involve retrieving water samples from reservoirs, wells, etc. and sending them to a chemical laboratory for analysis, often taking many months for results to be reported. A need exists for a reliable, light-weight, low-cost, highly-sensitive, and easily deployable water sensor that performs THM analysis in just a few minutes.

Accomplishment—We developed a portable system for THM detection in water using purge and trap, followed by isothermal gas chromatography and finally detection using a nanoporous-carbon (NPC) coated surface acoustic wave (SAW) sensor device. The SAW sensor device is at the heart of this detection scheme. SAWs respond to increased surface mass as a function of analyte concentration, which changes the acoustic propagation speed and can be measured as a phase shift in the wave over a fixed length. Sorbent coatings on a SAW surface can increase device response. We find that NPC coatings are reproducible, sensitive, and stable for long term use. Fig. 1 shows a 100 MHz SAW device coated with 1-µm-thick NPC (mass density ~ 1 g/cm^3), previously shown to be sufficient to achieve limits-of-detection (LOD) < 1 ppb for most volatile analytes studied. Fig. 2 shows the detection of each THM from fixed mixtures that are separated via a gas chromatograph and directed over the NPC-coated SAW. Chloroform elutes first, followed in succession by each chemical in order of molecular weight, with bromoform appearing last. Each response peak is integrated and plotted versus the known concentration for each THM in Fig. 3. We find similar functional behavior at these near-ppb concentration levels as we did previously for other volatile analytes at higher concentration levels, i.e. power-law behavior that fits to a straight-line on a log-log graph. These results demonstrate that 1 µm-thick NPC-coated SAW devices have LODs < 1 ppb for chloroform and ~ 1 part-per-trillion for bromoform!

Finally, we studied the relationship between the NPC coating thickness and the SAW response to controlled chloroform exposures, shown in Fig. 4, for thicknesses ranging from 0.25 to 2.5 µm, this time using only the response peak height, or phase shift. These results provide a defining property for NPC used for SAW device chemical detection. The chloroform LODs decrease exponentially with increasing NPC thickness, not linearly, as expected. Increasing NPC thickness from 1.1 to 2.5 µm, a factor of 2.2, improves the LOD by 20-fold, nearly an order-of-magnitude greater than expected!

Significance—Nanoporous-carbon coatings sorb volatile chemicals better than any other materials ever reported, improving SAW device microsensor LODs by multiple orders-of-magnitude. In particular, optimally NPC-coated SAW devices can detect THMs at part-per-trillion levels. This enables the development of portable chemical analysis systems for numerous field applications, including Homeland Defense, ES&H, Industry, and EPA regulations for our Nation's clean (and safe) water supply.

Sponsors for various phases of this work include: Laboratory Directed Research & Development and Work for Others

Contact: Michael P. Siegal, Nanomaterials Sciences
Phone: (505) 845-9453, Fax: (505) 844-1197, E-mail: mpsiega@sandia.gov

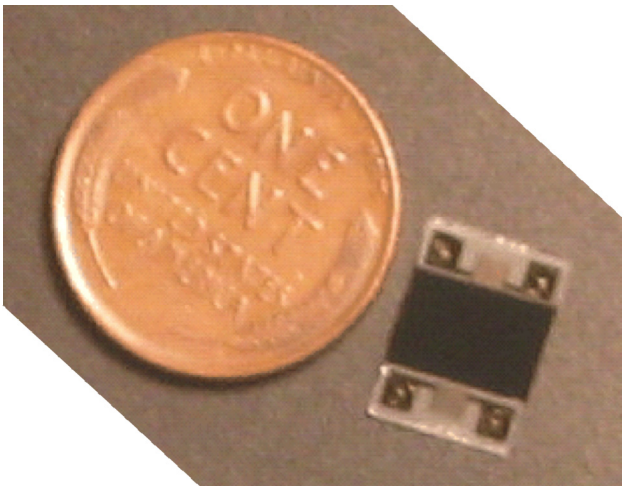

Figure 1. Photo of an NPC-coated 100 MHz SAW device next to a penny. Electrical contacts are made to the four large Au contact pads, and the Au transducer lines between them generate and detect the acoustic wave.

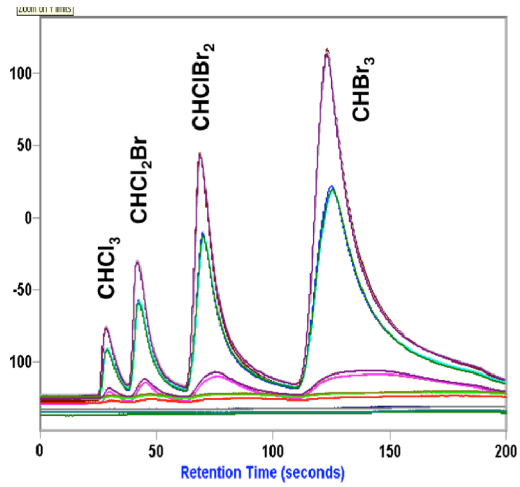

Figure 2. Phase-shift response from a 1 µm thick NPC-coated SAW device for controlled exposures to various concentration THM mixtures.

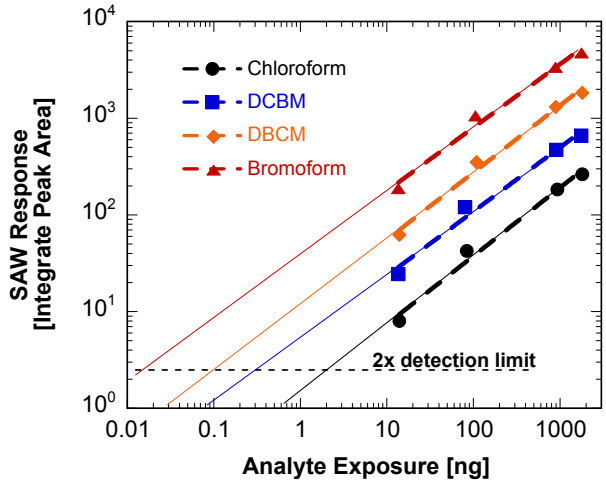

Figure 3. SAW response vs. analyte exposure for all four THMs, using the data shown in Fig. 2. (Note: 12 ng ~ 1 ppb.) The dashed line is placed a factor of two times above the SAW device detection limits, due to signal-to-noise. Therefore, the LODs for chloroform, DCBM, DBCM and bromoform are 0.16, 0.026, 0.0088, and 0.0013 ppb, respectively.

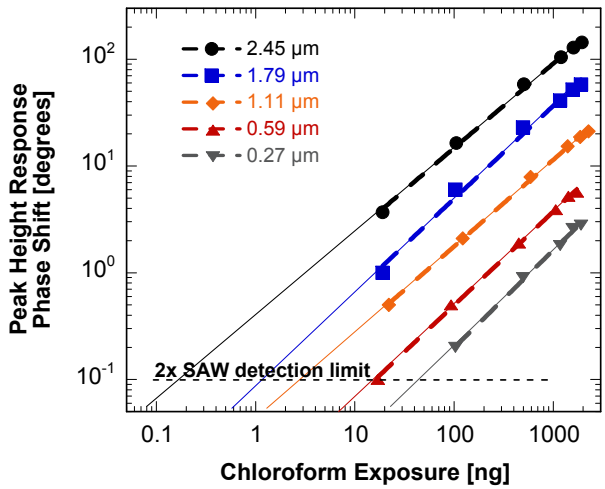

Figure 4. SAW response for chloroform detection as a function of NPC coating thickness. The LODs improve from 3.8 to 0.008 ppb for thicknesses ranging from 0.27 to 2.45 µm.

Trapping of Deuterium at Displacement Damage in Tungsten and the Implications for Tritium Retention in ITER

by W.R. Wampler

Motivation—The International Thermonuclear Experimental Reactor (ITER) is expected to produce enough fusion neutrons to cause atomic displacements approaching one displacement per atom (dpa) in plasma-facing materials. Tritium from the fusion plasma can diffuse into materials and become trapped at lattice defects, such as vacancies, produced by the neutron irradiation. This possibility has raised a concern that neutron damage might increase tritium retention and hence the in-vessel tritium inventory to the 700 gram limit and thereby restrict further operation. Of particular concern is T retention in the proposed 220 m^2 of tungsten which will receive high fluxes of energetic tritium ions from the plasma. To resolve this concern, experiments were conducted to determine the influence of displacement damage on the retention of deuterium in tungsten exposed to deuterium plasma. Retention of tritium is expected to be similar to that of deuterium.

Accomplishment—Tungsten samples were irradiated with 12 MeV silicon ions at various doses to produce up to 0.6 dpa to depths up to 2 microns, to simulate neutron damage. Irradiated samples were exposed at various temperatures to deuterium plasma at the PISCES-A high-flux linear plasma device at UCSD to simulate tokamak divertor conditions. Nuclear reaction analysis was then used to measure the concentration of retained deuterium versus depth. Deuterium retention was much lower at 500ºC than at 200ºC, due to the less effective binding to the traps, and annealing of damage at higher temperature. Deuterium retention was observed to be increased by displacement damage to depths up to 2 µm (figure 1). However, damage 250 µm beneath the plasma-exposed surface produced no increase in D retention. In addition to trapping at damage, near-surface retention from internal precipitation was observed at lower temperatures in both damaged and undamaged tungsten. These experiments determine the number of traps produced by displacement damage (figure 2) and the rate at which they are filled during exposure to plasma. Since helium will be present in fusion plasmas, the effect of helium in the deuterium plasma was also examined. Addition of 5% helium to the deuterium plasma greatly reduced D retention due to precipitation, but trapping at displacement damage still occurred.

Significance—Deuterium or He injected into tungsten by a plasma precipitates into bubbles near the surface. These bubbles act as sinks for diffusing D or T which lower its chemical potential and permeation to greater depths. This limits the depth to which T retention extends into the material and therefore the quantity retained. Based on trap production rates and kinetics of trap filling during exposure to plasma determined in this investigation, the inventory of tritium retained in tungsten in the ITER divertor due to trapping at displacement damage is predicted to be less than 10 g. This amount of tritium is much less than the 700 g in-vessel inventory limit, and also less than the quantity of tritium (50 g) to be injected per discharge. The low retention in tungsten is due to the shallow depth of penetration of tritium to traps at lower temperatures and the annealing of displacement damage and less effective binding to traps at higher temperatures. The conclusion is that neutron damage in tungsten should not increase tritium inventory enough to impact operation of ITER.

Sponsors for this work include: DOE Office of Science Fusion Energy Sciences Program

Contact: William R. Wampler, Radiation-Solid Interactions
Phone: (505) 844-4114, Fax: (505) 844-7775, E-mail: wrwampl@sandia.gov

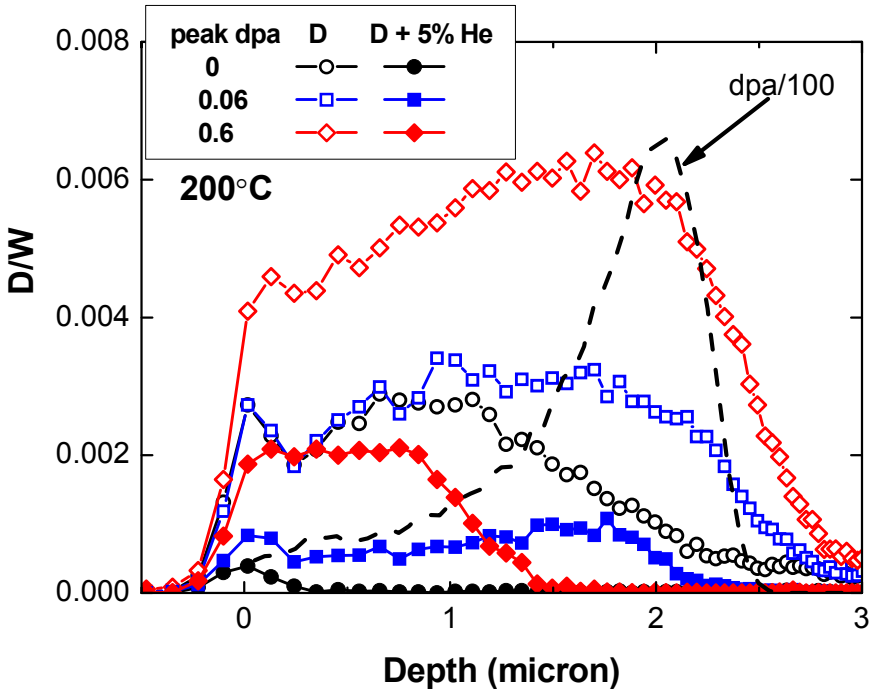

Figure 1. Deuterium content in tungsten exposed to deuterium plasma is increased by displacement damage and reduced by addition of helium to the plasma. The dashed curve shows the damage vs depth corresponding to a peak damage level of 0.6 dpa. The symbols show measured D profiles after exposure to D (open symbols) or D+5% He (solid symbols) plasma for various peak damage levels (black circle=undamaged, blue square=0.06dpa, red diamond=0.6 dpa).

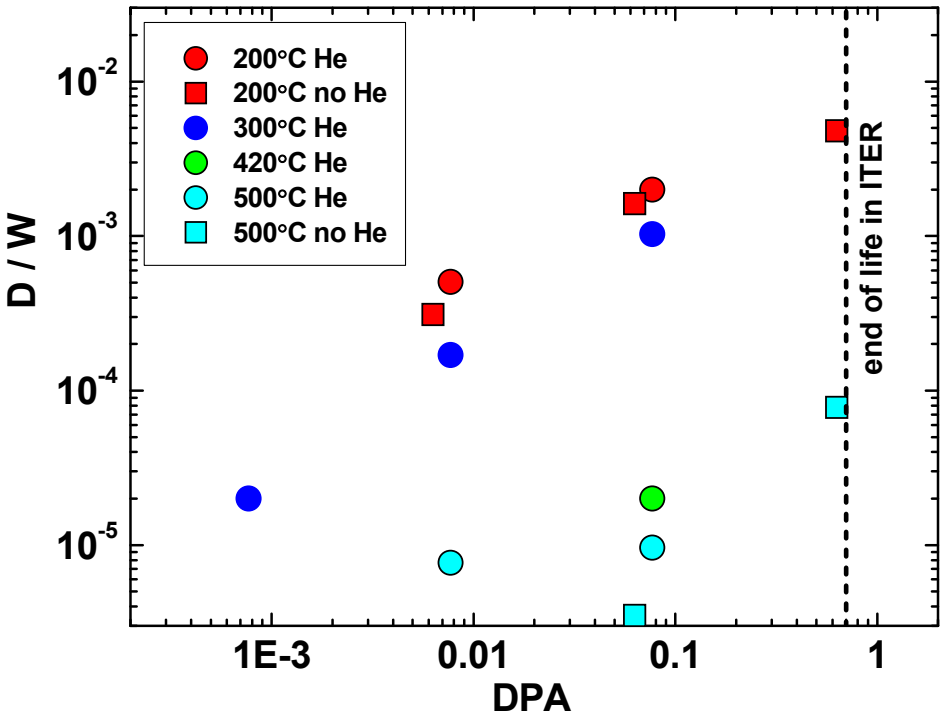

Figure 2. Increase in D concentration versus displacement damage for tungsten exposed to plasma at various temperatures.

Recent Awards & Prizes

Recent Awards & Prizes

National and International Awards

2009 — **Hispanic Engineer National Achievement Awards Corporation (HENAAC):** "For professional achievement." (Carlos Gutierrez)

2008 — **National Academy of Engineering (NAE):** "For development of large-scale simulations for improved understanding of metals, polymers, and particulate matter." (Gary Grest)

2005 — **American Academy of Arts and Sciences Fellow:** "For outstanding contributions in her profession." (Julia Phillips)
— **R&D100 Award:** "For the development of Ion Photon Emission Microscope (IPEM)." (Barney L. Doyle, Michael Mellon, Floyd D. McDaniel, and Paolo Rossi)

Other Awards

2009 — **American Physical Society Award:** "For outstanding referee." (Gary L. Kellogg)
— **Lockheed-Martin Award for Excellence in Research:** "For excellence in research regarding the Lockheed-Martin Shared Vision project on CNT photodectors." (Normand Modine and Alan Wright)

2008 — **American Physical Society Aneeesur Rahman Prize in computational physics:** "For ground-breaking development of computational methods and their application to the study of soft materials, including polymers, colloids, and granular systems." (Gary Grest)
— **American Physical Society George E. Pake Prize:** "For her leadership and pioneering research in materials physics for industrial and national security applications." (Julia Phillips)
— **Presidential Early Career Award for Scientists and Engineers (PECASE):** "For the combination of innovative research at the frontiers of science and technology and community service demonstrated through scientific leadership and community outreach." (Wei Pan)
— **Fellow, American Physical Society:** "For his pioneering experiments on metal-on-metal epitaxy leading to fundamental advances in understanding the structure of thin metal films, and for his exceptional service in the advocacy of nanoscience in the United States." (Robert Q. Hwang)
— **Fellow, American Association for the Advancement of Science:** "For outstanding accomplishments in chemically reacting flows and chemical vapor deposition modeling." (Michael E. Coltrin)
— **Fellow, American Association for the Advancement of Science:** "For outstanding accomplishments in semiconductor science and technology through personal research and leadership of group efforts, particularly in low dimensional physics and solid state lighting." (Jerry A. Simmons)
— **Fellow, American Association for the Advancement of Science:** "For outstanding contributions to compound semiconductor research through personal research, research management, and service to the research community." (Jeffrey Y. Tsao)

2006 — **Fellow, American Physical Society:** "For investigations of, and contributions to, the science of atomic and molecular processes in plasmas through development of innovative optical, microwave, and rf diagnostics." (Greg Hebner)

2005 — **Fellow, American Physical Society:** "For experiments advancing the understanding of electron correlation and electrodynamic response in oxide superconductors, ferromagnets, Coulomb glasses and nonlinear optical polymers." (Mark Lee)
— **Materials Research Society (MRS) "Science as Art" Competition First Prize Award:** "For Garden of ZnO Nano-Yuccas." (Julia Hsu, Tom Sounart, Neil Simmons, Jim Voigt, and Jun Liu)

Sandia National Laboratories Awards

2009 — **Laboratory Directed Research & Development Award for Excellence:** "*Exploiting Interfacial Water Properties for Desalination and Purification Applications*". (Dale Huber)

2008 — **Laboratory Directed Research & Development Award for Excellence:** "*For Ion-Neutron Simulation (INSIM)*". (Gyorgy Vizkelethy)

2007 — **Laboratory Directed Research & Development Award for Excellence:** "*For Nanolithography Directed Materials Growth and Self-Assembly.*" (Julia Hsu)
— **Laboratory Directed Research & Development Award for Excellence:** *"For Microwave to Millimeter Wave Electrodynamic Response and RF Applications of Semiconductor Quantum Nanostructures."* (Mark Lee)

2006 — **Laboratory Directed Research & Development Award for Excellence:** *"Elucidating the Mysteries of Wetting."* (Gary Grest)

2006 — **Laboratory Directed Research & Development Award for Excellence:** *"For an efficient implementation of finite-temperature, exact-exchange density-functional theory for Sandia's Socorro code, providing a breakthrough capability for condensed matter and high energy density sciences."* (Normand Modine and Alan Wright)

Patents Awarded

2009

— Patent 7,435,297
Title: Molten-Salt-Based Growth of Group III Nitrides
Originators: Karen E. Waldrip, Jeffrey Y. Tsao, Thomas M. Kerley
— Patent 7,449,404
Title: Method for Improving Mg Doping during Group-III Nitride MOCVD
Originators: Randall J. Creighton, George T. Wang
— Patent 7,491,423
Title: Directed Spatial Organization of Zinc Oxide Nanostructures
Originators: Julia Hsu, Jun Liu

— Patent 7,550,734
Title: Integrated Heterodyne Terahertz Transceiver
Originators: Mark Lee, Michael C. Wanke
— Patent 7,566,429
Title: Catalytic Reactive Separation System for Energy-Efficient Production Cumene
Originators: Genoveva Buelna, Tina M. Nenoff

2008
— Patent 7,338,590
Title: Water-Splitting using Photocatalytic Porphyrin-Nanotube Composite Devices
Originators: John A. Shelnutt, James E. Miller, Craig Medforth, Zhongchun Wang
— Patent 7,374,599
Title: Dendritic Metal Nanostructures
Originators: John Shelnutt, Yujiang Song, Eulalia Pereira, Craig Medforth
— Patent 7,376,403
Title: Terahertz Radiation Mixer
Originators: Michael C. Wanke, S. James Allen, Mark Lee
— Patent 7,420,225
Title: Direct Detector for Terahertz Radiation
Originators: Michael C. Wanke, Mark Lee, Eric A. Shaner, S. James Allen
— Patent 7,422,724
Title: Biological Preconcentrator
Originators: Ronald P. Manginell, Bruce C. Bunker, Dale L. Huber

2007
— Patent 7,223,474
Title: Heteroporphyrin Nanotubes and Composites
Originators: John A. Shelnutt, Craig J. Medforth, and Z. Wang
— Patent 7,248,397
Title: Wavelength-Doubling Optical Prametric Oscillator
Originators: Darrell J. Armstrong and Arlee v. Smith

2006
— Patent 7,148.974
Title: Method for Tracking the Location of Mobile Agents Using Stand-off Detection Technique
Originators: Susan F.A. Bender, Philip J. Jargis, Jr., Mark S. Johnson, Philip J. Rodacy, and Randal L. Schmitt
— Patent 7,132,163
Title: Hereroporphyrin Nanotubes and Composites
Originators: Jahn A. Shelnutt, Craig J. Medforth, and Z. Wang
— Patent 7,122,164
Title: Niobate-Based Octahedral Molecular Sieves
Originators: Tina M. Nenoff and May D. Nyman
— Patent 7,119,245
Title: Synthesis of an Un-supported, High-Flow ZSM-22 Zeolite Membrane
Originators: Steven G. Thoma and Tina M. Nenoff

— Patent 7,064,817
Title: A Method to Determine and Adjust the Alignment of the Transmitter and Receiver Fields of View of a LIDAR
Originators: Philip J. Hargis, Jr., Tammy D. Henson, Leslie J. Krumel, and Randal L. Schmitt
— Patent 7,041,616
Title: Enhanced Selectivity of Zeolites by Controlled Carbon Deposition
Originator: Mutlu Kartin, Tina M. Nenoff, and Steven G. Thoma

2005
— Patent 6,980,354
Title: A Self-Seeding Ring Optical Parametric Oscillator
Originator: Darrell J. Armstrong and Arlee V. Smith
— Patent 6,964,936
Title: Method of Making Maximally Dispersed Heterogeneous Catalysts
Originator: Dwight R. Jennison
— Patent 6,866,560
Title: Method for Thinning Specimen
Originator: David M. Follstaedt and Michael P. Moran
— Patent 6,844,378
Title: Method of Using Triaxial Magnetic Fields for Making Particle Structures
Originator: James E. Martin, Robert Anderson, and Rodney Williamson

Government & National Advisory Boards, Professional Societies, International Committees, and Journals

Government & National Advisory Boards

Argonne National Laboratories

— Review Panel, Electron Microscopy Center for Materials Research (EMC) Operations Review: Jianyu Huang, 2009

Department of Energy, Office of Basic Energy Sciences

— Idaho State DOE ESPCoR program, Princeton Center for Complex Materials (MRSEC) and UMass EFRC. External Review Committee, Julia Hsu, 2009
— BES Advisory committee on Facing Our Energy Challenges in a New Era of Science; Julia Phillips, member; 2008
— Council of the BES Division of Materials Sciences & Engineering; Julia Phillips, member; 2006-2008
— BES Advisory Committee Subcommittee on Grand Challenges in BES; Julia Phillips, member; 2006-2007
— Workshop on Basic Research Needs for Solid State Lighting: Julia Phillips, Workshop Chair; Jerry Simmons, Panel Chair; Mary Crawford, Panel Member; 2006

Department of Defense / Central Intelligence Agency

— Advisory Committee for the Modeling and Simulation component of the Energetic Materials Net Assessment; Alan Wright, member; 2009

Los Alamos National Laboratory

— Materials Capability Site Review; Julia Phillips, participant; 2008-2009
— Materials Capability Site Review; Tina Nenoff, participant; 2007

The National Academies

— Panel Member; Nuclear Waste Form Development, Tina Nenoff, 2009

National Academy of Engineering

— Council; Julia Phillips, member: 2008-2011
— Peer Committee, Materials Section: Julia Phillips, member, 2007-2009, Chair, 2009
— U. S. Frontiers of Engineering Program: Julia Phillips, Chair, 2005-2008; Mary Crawford, participant, 2005; George Bachand, participant 2007, Greg Hebner, Session Organizer, 2008
— Draper Prize Committee; Julia Phillips, member; 2005-2007

National Research Council

— Committee on Nanophotonics Assessability and Applicability; Jerry Simmons, member; 2006-2007
— Review Panel, National Research Council Associateship Program: Diane Peebles, Neal Shinn, and Greg Hebner, members; 2006-2009
— Committee on Benchmarking the Research Competitiveness of US Chemical Engineering; Julia Phillips, member; 2006
— Committee to Assess the Impact of the MRSEC Program; Julia Phillips, BPA liaison; 2005-2006
— Board on Chemical Sciences & Technology; Bob Hwang, member; 2004-2007
— Board on Physics and Astronomy; Julia Phillips, member; 2000-2006

New Mexico State University
— New Mexico Nanoscience Education Initiative, Advisory Board; Neal Shinn, member; 2007
— Physics Advisory Board: Neal Shinn, member, 2004-2007; Alan Wright, member 2002-2004, 2006-2008

Oak Ridge National Laboratory
— BES Chemical Sciences Site Review; Tina Nenoff, participant; 2007
— BES Site Review; Gary Kellogg, participant; 2006

Texas State University
— Materials Science & Engineering Advisory Board; Carlos Gutierrez, member; 2006-2008

Wessex Institute of technology (UK)
— Scientific Committee; Frank Van Swol, member, 2006-present

Professional Societies/International Committees/Journals

American Association for Crystal Growth
— 20th American Conference on Crystal Growth and Epitaxy; Sean Hearne, Symposium Chair; 2006, Symposium Organizer, 2009, West Program Chair 2010
— American Conference on Crystal Growth and Epitaxy; Robert Biefeld, Conference Organizer; 2009
— Executive Committee; Bob Biefeld, member; 2005-present

American Association for the Advancement of Science (AAAS)
— Board of Directors; Julia Phillips, member; 2003-2005
— Physics Section; Julia Phillips: Chair-elect, Chair, Past Chair; 2003-2005
— Physics Section Nominating Committee: Julia Phillips, member, 2003-2004; Chair, 2005

American Chemical Society (ACS)
— Committee on Science; Tina Nenoff, associate; 2007
— COLL Division; Tina Nenoff, councilor; 2006-2010

American Physical Society (APS)
— March Meeting Program Committee, Invited Session; Program Organizer; Robert Biefeld; 2010
— March Meeting Focused Session; Robert Biefeld, organizer; 2010
— Topical Group on Energy Research and Applications (GERA); Robert Biefeld; Executive Committee member
— March Meeting Program Committee, Workshop on Energy for Young Physicists; Julia Hsu, member; 2008-2010
— Aneesur Rahman Prize Committee; Gary Grest, member; 2008
— George E. Pake Prize Committee; Julia Phillips, member; 2008
— McGroddy Prize Committee; Julia Hsu, member; 2007-2008
— March Meeting Focused Session; Julia Hsu, organizer; 2007
— Division of Condensed Matter Physics (DCMP): Julia Phillips, Vice-Chair, 2005; Chair-Elect, 2006; Chair, 2007; Past Chair, 2008

— Forum on Industrial & Applied Physics (FIAP): Mark Lee, Vice-Chair, 2005; Chair-Elect, 2006; Chair, 2007
— Committee on Minorities; Carlos Gutierrez, Chair; 2006
— Bouchet Prize Committee; Carlos Gutierrez, member; 2005-2006
— Division of Materials Physics (DMP) Executive Committee; Julia Hsu, member-at-large; 2004-2006
— Committee on Meetings; Mark Lee, member; 2003-2006

American Vacuum Society (AVS)
— Neal Shinn, President; 2007
— 53rd International Symposium
— Neal Shinn, Vice Chair; 2006
— Distinguished Lecture Series Committee; Neal Shinn, Chair; 2004-2006
— Board of Directors; Neal Shinn, member; 2003-2006

ASM International – The Materials Information Society
— Events Committee; Dan Barton, member; 2003-present
— Electronic Device Failure Analysis Society (EDFAS): Dan Barton, Board of Directors member, 1998-present; Vice-President, 2005

Chemistry of Materials
— Editorial Board; Tina Nenoff, member; 2006-2010

Conference on Magnetism and Magnetic Materials
— Scientific Advisory Board; Carlos Gutierrez, member; 2005-2007

Electrochemical Society
— Symposium; Nancy Missert, organizer; 2006, 2007
— Corrosion Division, Nancy Missert: Student Travel Grant Coordinator, 2005-2008; executive committee member, 2006-present
— Nash Miller Award Committee; Nancy Missert, member; 2005
— Individual Membership Committee; Nancy Missert, member; 2003-2006

Electronic Materials Conference
— Organizing Committee, Julia Hsu; 2009

Fifteenth International Conference on Crystal Growth
— Bob Biefeld, Program Co-Chair; 2006-2007

Gaseous Electronics Conference (GEC)
— 56th Annual Meeting; Greg Hebner: Chair-elect, Chair, Past Chair; 2003-2006

Gordon Conference
— Nanoporous Materials Gordon Conference; Tina Nenoff, Chair-elect, 2011
— Zeolite Gordon Conference; Tina Nenoff, Vice-Chair; 2008

Institute of Electrical and Electronics Engineers (IEEE)

— *Transactions on Plasma Science*, 4th issue on Images in Plasma Science; Greg Hebner, guest editor; 2004-2005
— *Transactions on Device and Materials Reliability (TDMR)*; Dan Barton, guest editor; 2002-present
— International Reliability Physics Symposium, Management Committee; Dan Barton, member; 2001-present

International Conference on Applications of Accelerators in Research and Industry

— Barney L. Doyle, Chairman; 2004, 2006, 2008

International Conference on Defects in Semiconductors

— International Advisory Board, Alan Wright,: Co-organizer, 2005-2007, Co-Chair, 2007

International Conference on Electrorheological Fluids and Magnetorheological Suspentions

— James E. Martin, program committee; 2001-2009

International Conference on Ion Beam Analysis

— Barney Doyle, Gyorgy Vizkelethy; International Committee, 2008

International Conference on Low Energy Electron Microscopy/Photoemission Electron Microscopy (LEEM/PEEM)

— International Steering Committee, Gary L. Kellogg, member 2009
— International Advisory Committee; Gary L. Kellogg, member; 2000-present

International Conference on Metal Organic Chemical Vapor Deposition-15 (ICMOVPE-15)

— Conference Organizer; Robert Biefeld; 2009-2010, Andrew Allerman, Conference Committee – 2009-2010

International Conference on Modern Materials and Technology

— Advisory Board; Julia Hsu; 2009

International Conference on Nitride Semiconductors - 7th

— Americas Program Chair; Andrew Allerman 2007

International Conference on Nuclear Microprobe Technology and Applications

— International Committee; Gyorgy Vizkelethy; International Committee, 2008

International Conference on Particle-Induced X-Ray Emission and its Analytical Applications

— International Committee; Barney L. Doyle, member; 2005

International Conference (4th) on Porphyrins and Phthalocyanines

— Symposium; John Shelnutt, Organizer and Chair; 2004, 2006, 2008

International Electron Devices Meeting

— Session; Tom Friedmann, organizer; 2007

International Journal of PIXE (IJPIXE)
— Editorial Board, Barney Doyle; 1996-present

International Symposium on Semiconductor Light Emitting Devices - 7th
— Program Co-Chair; Andrew Allerman, 2008

International Thin Film Conference
— Advisory Board; Julia Hsu; 2009

International Union for Vacuum Science, Technique, and Applications (IUVSTA)
— 17th International Vacuum Congress; Neal Shinn, Program Committee member; 2007
— Surface Science Electoral College, Neal Shinn, United States Representative; 2001-2007
— Surface Science Division: Neal Shinn, Chair, 2004-2007; Secretary, 2001-2004

International Zeolite Association (IZA)
— Commission on Synthesis Committee; Tina Nenoff, member; 2004-2007

Journal of Chemical Physics
— Editorial Board; Jim Martin, member; 2003-2006

Journal of Crystal Growth
— *Journal of Crystal Growth* for subject areas: "Epitaxial Growth and Nanostructures"; Bob Biefeld, Associate Editor; 2004-present

Journal of Materials Research
— Editorial Advisory Board; Julia Phillips, member; 2004-present; chair; 2008-present

Journal of Scanning Probe Microscopy
— Editorial Board; Brian Swartzentruber, member; 2009

Lawrence Berkeley National Laboratory
— Accelerator Fusion Research Department Review; Barney Doyle, 2006-2007
— National Center for Electron Microscopy Operations Review, Jianyu Huang, 2009

Lawrence Livermore National Laboratory
— Panel member; Transformational Materials Initiative, Tina Nenoff, 2009

Materials Research Society (MRS)
— Surface Electron Microscopy Symposium; Gary Kellogg, lead organizer; Spring 2008
— Operational Oversight Committee; Julia Hsu, Treasurer and member; 2006-2007
— *MRS Bulletin*: H_2 Production; Tina Nenoff, co-editor; October 2006
— Symposium Organizers: Neal Shinn and John Sullivan, organizers; Spring 2006; Barney Doyle, organizer, Fall 2005
— Meeting Chair: Julia Hsu, Fall 2007
— Board of Directors: Julia Hsu, member, 2005-2007
— Technical Program Committee; Julia Phillips, Chair; 2005-2008
— Web Advisory Sub-Committee: Sean Hearne, member, 2005-2006; Chair, 2006

— Electronic Services Task Force: Sean Hearne, member; 2005
— Membership Committee: Sean Hearne, member, 2004-2008
— Information Services Committee: Sean Hearne, Chair 2006-2009
— JMR Editor-in-Chief Search Committee: Sean Hearne, Chair, 2008

Microelectronics Reliability (Elsevier Journal)
— Editorial Advisory Board; Dan Barton, member; 2000-present

National Association of Corrosion Engineers
— H.H. Uhlig Educator Award Committee; Nancy Missert, 2006-2008

Nuclear Instruments and Methods in Physics Research, Section B: Beam Interactions with Materials and Atoms
— Editorial Board; Barney Doyle, member; 2003-2006

Pacifichem (Honolulu)
— Symposium; John Shelnutt, organizer and Chair; 2005

Physical Review E
— Gary Grest, Senior Editor; 2002-present

Solid State Communications
— Julia Hsu, Editorial Board; 2005-present

The Minerals, Metals, and Materials Society (TMS)
— Electronic Materials Conference: Nanoscale Characterization, Zinc Oxide, and Organic/Hybrid Photovoltaics Symposium; Julia Hsu, organizer; 2007
— Electronic Materials Committee: Bob Biefeld, member, 2002-present; secretary, 2002-2004; Vice Chair, 2005-2007; Chair, 2007-2009; Past Chair, 2009-2011; Julia Hsu, member, 2000-2006
— Electronic Materials Conference: Group III-Nitrides: Growth, Processing, Characterization, Theory and Devices; Andrew Allerman, organizer; 2005-present
— Symposium; Sean Hearne, organizer; March 2004

US Organometallic Vapor Phase Epitaxy Workshop
— Organizing Committee; Bob Biefeld, member; 1991-present

World Scientific Publishing Company (WSPC)
— Editorial Board, “Reviews of Accelerator Science and Technology”; Barney Doyle, 2007-2008

Resources & Capabilities

— Diagnostics and Characterization —

Atomic-Level Imaging and Spectroscopy
We have developed technical capabilities in the following areas:

- Scanning Tunneling Microscopy (STM) with the ability to track the diffusion of single atoms on surfaces
- Low Energy Electron Microscopy (LEEM) with nanometer spatial resolution and real-time spectroscopic imaging capability at sample temperatures from 300K to over 1000K
- Field Ion Microscopy (FIM) with single atom resolution and accurate temperature control to 1 Kelvin,
- Atom Probe Microscopy (APM) with pulsed laser desorption capability
- Interfacial Force Microscopy (IFM), with feedback for accurate, simultaneous normal and frictional force profile measurements for the quantitative study of adhesion, tribology, nanomechanics, and the mechanical assessment of microsystem components
- Atomic Force Microscopy (AFM) for imaging, force profiling, and manipulation of individual biomolecules in fulid environments with simultaneous fluorescence detection
- Piezo Force Microscopy (PFM) for measuring piezoelectric coefficient, imaging ferroelectric domains, and spatial variation in piezoelectric properties, and input

Chemical Vapor Deposition (CVD)
Sandia provides experimental tools for investigating CVD which include optical probes (such as reflectance-difference spectroscopy) for gas phase and surface processes, a range of surface analytic techniques, molecular beam methods for gas/surface kinetics, and flow visualization techniques. These tools are also integrated in a unique manner with research CVD reactors and with advanced chemistry and fluid models.

Electrochemical Scanning Probe Microscopy
We have developed the ability to study nanoscale changes at surfaces during oxidation and dissolution of metal surfaces under electrochemical control using scanning tunneling microscopy. These studies can be performed in a variety of electrolytes in order to determine the mechanisms governing passive film growth.

Growth Science Laboratory
Sandia has capabilities for in-situ characterization of materials during thin film deposition, molecular beam epitaxial growth, and low energy ion beam simulated growth, using intensity profile sensitive reflection high energy electron diffraction (RHEED) for surface structure, x-ray reflectometry for in-situ surface and interface structure, multibeam wafer curvature for strain (Patent #5,912, 738), and Auger electron spectroscopy for surface composition.

Ion Accelerator Nuclear Microprobe
Sandia provides energy >4 MeV, nuclear microscopy and radiation effects microscopy. This 6 MV tandem accelerator generates ion species from hydrogen to gold for both radiation effects research and quantitative ion beam analysis of materials containing light elements (hydrogen to fluorine) using heavy ion elastic recoil detection (ERD) and heavy elements using high-energy back scattering spectrometry. An external Micro Ion Beam Analysis (X-MIBA) capability enables multi-elemental analysis and ion irradiation of samples, which are vacuum incompatible or extraordinarily large. The Sandia Nuclear Microprobe with submicrometer size high-energy ion beams is used to study materials and devices. Special emphasis is given to the evaluation of the radiation hardness of

microelectronic devices using three new advanced diagnostic techniques invented at Sandia: Single-Event-Upset Imaging, Ion-Beamed-Induced-Charge Collection Imaging (IBICC), and time-resolved IBICC. We have also developed the Ion Electron Emission Microscope (U. S. Patent No. 6,291,823 and 2001 R&D-100 Award winner), which can perform radiation microscopy using very highly ionizing particles without focusing the ion beam. A recent extension of this microscope is a desktop version that uses an alpha radiation source, called the Ion Photon Emission Microscope (which also received an R&D 100 Award in 2005).

KMAP X-ray Diffractometer

Based on double crystal x-ray diffractometry in combination with position sensitive x-ray detection, our KMAP x-ray diffraction analysis is used to determine the lattice constant, strain relaxation, composition, layer orientation, and mosaic spread for a large variety of advanced epitaxial semiconductor materials.

Lasers and Optical Spectroscopies

Sandia has capabilities in characterizing semiconductor materials by photoluminescence and magnetoluminescence down to low temperatures by optical laser imaging and laser microscopy, by laser excitation spectroscopy, and by the time-resolved measurements of optical emission. We also have developed a high lateral resolution, near-field scanning optical microscopy (NSOM) capability with time and frequency resolution. Sandia also has capabilities in gas phase spectroscopy using pulsed and CW laser sources covering the range from microwave frequencies, THz and thorough the deep UV.

Lasers and Optics

We provide characterization and advanced understanding in the area of solid-state lasers and non-linear optics, especially as coherent sources of broadly tunable light in rugged, compact geometries. We also have established expertise in long-term and transient radiation effects characterization of optical materials. Capabilities include the widely used (approximately 2000 users worldwide) SNLO (Sandia Non-Linear Optics) code, which is a lab-tested code for predicting the performance of non-linear optical components. In the area of integrated optical materials, our laboratories produce new types of photosensitive materials (processing patent applied for) for directly-writeable waveguides and reconfigurable optical interconnects.

Low-Temperature Plasma Analysis

We have state-of-the-art capabilities for the analysis of low-temperature plasmas as found in commercial processing reactors. These include emission spectroscopy, electrical characterization, laser and microwave-based measurements of species concentrations, *in situ* electric field measurements, and others. Sandia is the only lab that combines new diagnostics, relevant process chemistries (complex mixtures), and massively parallel (MP) computer models for simulation of continuous and transient plasmas. We also have strengths in plasma – surface interactions, plasma enhanced catalisis and plasma surface modification using plasma sources.

Quantum optics and cold matter physics

Sandia has capabilities in quantum optics and cold matter physics. This includes Bose Einstein condensates, trapped ion for applications to quantum computing and entangled state photon systems for improved remote sensing systems.

Remote Sensing
Sandia has extensive capabilities related to laser based remote detection of materials. We have established and field tested systems that are mounted in trailers, vans and flexible air craft platforms. These systems are flexible and portable spectroscopy systems that find a wide range of applications including WMD detection and topology characterization.

Materials Microcharacterization
Our capabilities in this area include optical microscopy, scanning, electron microscopy, analytical transmission electron microscopy, double crystal x-ray diffraction, ion beam analysis of materials (RBS, channeling, ERD, PIXE, NRA), Hall measurements, microcalorimetry, photoluminescence, light scattering, electronic transport, deep level spectroscopy, magnetization, and dielectric and magnetic susceptibilities.

MEMS-based Tensile Testing
We have developed the capability to perform pure uni-axial loading of metal MEMBS test structure *in situ* and ex situ of a TEM. The technique has been demonstrated using Al, Ni and Cu, but is applicable to a wide range of other materials.

Nanoelectronics Laboratory
Sandia has capabilities for fabrication of nanoscale quantum device structures together with capabilities for ultra-low noise measurement of transport form 0.3 Kelvin to ambient at high magnetic fields.

Scanning Cathodoluminescence Microscopy
We have developed the ability to measure and image cathodoluminescence from insulators and semiconductors on the submicron scale in order to understand how defects influence the emission of light from the ultraviolet to the visible. Individual spectra are also obtained at controlled locations in order to identify heterogeneities.
Scanning Probe Metrology
We have developed a unique wide-field scanning Interfacial Force Microscope with calibrated force detection for the dynamic measurement of normal and lateral forces of micro-electrical-mechanical system components in operation**.**

Simultaneous Measurement of H, D, and T in Materials
We have designed and implemented a new ion beam analysis (IBA) system to simultaneously measure the absolute quantities of H, D, and T in materials using an elastic recoil detection (ERD) technique. The technique uses an E-dE detector arrangement, or particle telescope, to provide for accurate separation of the H, D, and T signals. The system can also simultaneously acquire information about medium and high Z elements in the sample using Rutherford backscattering spectrometry (RBS). Measurement of other light elements is possible using the nuclear reaction analysis (NRA) technique, which is isotope specific. The system will have an accuracy of $< 2\%$ for measuring the composition of solids.

Zeolite and Nanomaterials Analytical Lab
The Zeolite and Nanomaterials Analytical Lab has a suite of instrumentation relevant for the characterization or analysis of a wide array of novel zeolite, complex oxide or nanoparticulate materials for project research applications. The lab houses characterization equipment including a Siemens x-ray diffractometer (XRD), a Fourier transform infrared spectroscopy (FTIR) system, a Temperature Programmed Desorption (TPD) system, a Brunauer, Emmett and Teller (BET) system, and Thermogravimetric Analysis (TGA) instruments.

— Synthesis and Processing —

We apply our facilities and personnel expertise for synthesis and processing of novel materials requiring higher accuracies, or greater understanding of the link between process and performance, than normal. These facilities and expertise range from chemical processes such as chemical vapor deposition to physical processes such as pulsed laser deposition to complex multi-phenomena processes such as ECR plasma deposition and etching. Our technical capabilities include:

400 keV and 180 keV Ion Implanters
These systems are equipped with a variety of sources (gas, sputter, and metal vapor). This facility provides ion species from hydrogen to bismuth that can be used for studying fundamental irradiation mechanisms and selective chemical doping in semiconductors, metals, ferroelectrics and superconductors. The 180 keV Implanter is capable of both ambient and high temperature implants up to 600°C and ion currents up to 50 micro-A.

Crystal and Thin Film Growth
Capabilities in this area include a pulsed laser deposition chamber, a thin film oxide deposition chamber, a diamond-like carbon deposition chamber, a hot filament, chemical vapor deposition chamber, and various apparatus for single crystal growth. Our capabilities for stress relief of diamond-like carbon films and structures produced by pulsed laser deposition are not available elsewhere.

Glancing Angle Deposition System
This system is designed to grow nanowires by depositing on a substrate that is oriented at a high angle (~85°) to the deposition flux. Nanowires naturally form due to shadowing effects that occur as the deposition proceeds. In addition, rotations about the substrate normal during deposition result in helical structures. Currently, the deposition source is configured with an e-beam evaporation source such that most materials that can be evaporated can be deposited as nanowires.

Metal-Organic Chemical Vapor Deposition (MOCVD)
We maintain research facilities with capabilities in MOCVD of compound semiconductor materials. These capabilities include research reactors designed specifically for studies of CVD chemistry, fluid dynamics, the development of advanced in-situ diagnostics, and the development of advanced semiconductor heterostructures and devices. We also investigate the synthesis and properties of a variety of nanostructures including quantum dots and nanowires using MOCVD.

Molecular Beam Epitaxy (MBE)
We have research semiconductor growth laboratories for ultra-pure and ultra-flexible MBE growth of III-V materials

Monolayer Deposition of Organic Films
We have a Langmuir-Blodgett facility for controlled deposition of mono- and multi-layer organic films. The facility includes two computer-controlled troughs, in situ fluorescence microscopy, vibration isolation, and a dust-free down flow work area. These combined capabilities are not available in the private sector.

Nanocluster Laboratory
We have developed numerous processes for the synthesis of large quantities of monodisperse particles and clusters of metals, semiconductors, and oxides.

Soft Nanolithography
Soft nanolithography refers to patterning techniques that complement UV and electron beam lithography. These approaches avoid the chemical and radiation exposure often used in conventional lithography processing, making soft nanolithography particularly useful for bio, organic, and molecular materials. Current capabilities include micro-contact printing, nano-transfer printing, and dip-pen nanolithography.

Stress Evolution During Electrodeposition
We have developed the capability to measure stress evolution during thin film electrodeposition and have used it to measure stress during patterned and unpatterned film growth. Our studies range from fundamental mechanisms that create stress during island coalescence to materials-specific systems, such as electrodeposited Ni, Cu, Sn, Ag and their alloys.

Synthetic Organic Laboratory
Novel lipids, surfactants, and other small molecules are prepared in this laboratory via synthetic organic techniques. The laboratory is also capable of forming and characterizing self-organized structures (e.g., liposomes, micelles, self-assembled monolayers, LB films) generated with the newly synthesized molecules in pure or mixed molecular systems.

Zeolite and Nanomaterials Chemical Synthesis Laboratory
The primary work in this lab involves the production and synthesis of novel materials via standard chemical processing for research applications for relevant projects. In addition to needed chemical materials stock, the lab includes standard laboratory equipment including fume hoods, pH meters, filtration devices, small tube furnaces, synthetic glassware, ovens, and stir plates.

— Theory and Simulation —

Our capabilities in theory and simulation can be applied toward understanding of the synthesis and properties of new materials and/or structures. They are particularly valuable for understanding how to tailor or tune properties for specific applications. The technical capabilities include:

Chemical Processes
We have extensive capabilities, including massively parallel computation, to model complex chemically reacting flows that occur in chemical vapor deposition manufacturing processes. Our numerical simulations can include the coupled gas-phase and gas-surface chemistry, fluid dynamics, heat, and mass transfer to provide predictive models of a chemical process.

Complex System Analysis
We have developed a suite of tools to manage complex data collections and process them to produce user defined information. One key advantage of our approach is that the user employs high-level interactions to process the data and is freed from traditional programming language constructs.

Electronic Structure and Linear Scaling
We have developed state-of-the-art massively parallel electronic structure algorithms, based on ab initio pseudopotentials and plane-wave/Gaussian basis functions. These codes are used to develop a fundamental understanding of physical phenomena and materials, including compound semiconductor band structure, diffusion of point defects, dopants and impurities, optoelectronic properties of extended defects, adsorbate interactions on surfaces, bonding at metal-oxide interfaces, and enhanced reactivity of nanoparticles. To allow the investigation of more complex systems and phenomena, we have developed new computationally efficient algorithms, e.g., self-consistent linear scaling density functional theory, and variable and real-space gridding.

Low-Temperature Plasmas
We have extensive capabilities in massively parallel codes to simulate the time and space evolution of low-temperature plasmas, focusing on new theoretical techniques for achieving rapid convergence and on direct comparisons with experimental results.

Molecular Dynamics Simulation
Large scale, classical molecular dynamics simulations using the massively-parallel code LAMMPS (Large-scale Atomic/Molecular Massively Parallel Simulator) are being used to model a wide variety of systems. These classical simulations cover the length and time scale intermediate between quantum and continuum calculations. Systems of current interest include adhesion and friction in self-assembled monolayers, degradation of polymer adhesives, wetting and spreading of multi-component fluids and transport in polymer membranes for fuel cells. Modifications of the algorithm to include particle rotation and friction have been implemented to study granular materials.

Optical and Wave Propagation
We have developed advanced simulation codes for understanding wave propagation in optical parametric oscillators and amplifiers for the purpose of designing highly efficient, tunable laser sources. We also have capabilities in novel optical designs, including resonators for compact laser geometries. These capabilities are coupled to in-house micro-optics construction facilities and state-of-the-art optics testing.

Physical, Chemical, and Nano Sciences Center – FY09 Budget

Physical, Chemical and Nano Sciences Center FY09 Budget - by Customer

Operating ($48.3M)

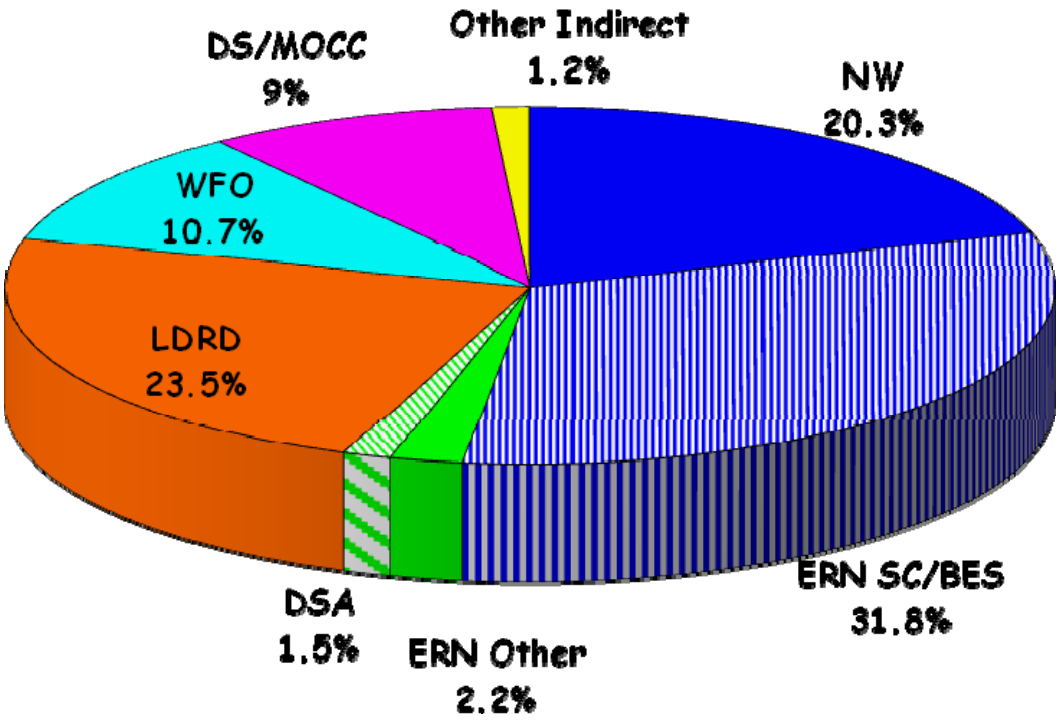

Capital ($5.8M)

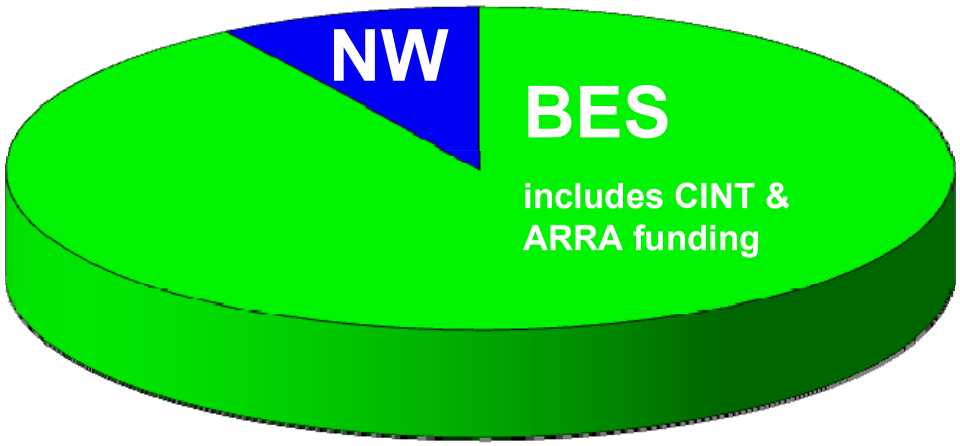

NW	Nuclear Weapons	ERN	Energy, Resources & Nonproliferation	WFO	Work for Others (includes WFOs in ERN,DSA,HSD,NW)
DSA	Defense Systems & Assessments	SC/BES	Office of Science/Basic Energy Sciences	LDRD	Laboratory Directed Research & Development

SAND2010-1393P: *Research Briefs* for the Physical, Chemical, & Nano Sciences Center is published by Sandia National Laboratories, a multiprogram laboratory operated by Sandia Corporation, a Lockheed Martin Company, for the United States National Nuclear Security Administration and the Department of Energy under Contract DE-AC04-94AL85000.

Printed 2010